DISCLAIMER

This report was prepared as an account of work sponsored by an agency of the United States Government. Neither the United States Government nor any agency thereof, nor any of their employees, makes any warranty, express or implied, or assumes any legal liability or responsibility for the accuracy, completeness, or usefulness of any information, apparatus, product, or process disclosed, or represents that its use would not infringe privately owned rights. Reference herein to any specific commercial product, process, or service by trade name, trademark, manufacturer, or otherwise does not necessarily constitute or imply its endorsement, recommendation, or favoring by the United States Government or any agency thereof. The views and opinions of authors expressed herein do not necessarily state or reflect those of the United States Government or any agency thereof. Reference herein to any social initiative (including but not limited to Diversity, Equity, and Inclusion (DEI); Community Benefits Plans (CBP); Justice 40; etc.) is made by the Author independent of any current requirement by the United States Government and does not constitute or imply endorsement, recommendation, or support by the United States Government or any agency thereof.

SANDIA REPORT

SAND2025-06635
Printed June 2025

Sandia
National
Laboratories

Modal Field Reconstruction in Resonant Cavities in the Fundamental and Undermoded Frequency Regimes

Jon Wallace and Chandler Smith

Prepared by
Sandia National Laboratories
Albuquerque, New Mexico 87185
Livermore, California 94550

Issued by Sandia National Laboratories, operated for the United States Department of Energy by National Technology & Engineering Solutions of Sandia, LLC.

Available to DOE and DOE contractors from

U.S. Department of Energy
Office of Scientific and Technical Information
P.O. Box 62
Oak Ridge, TN 37831

Telephone:	(865) 576-8401
Facsimile:	(865) 576-5728
E-Mail:	reports@osti.gov
Online ordering:	http://www.osti.gov/scitech

Available to the public from

U.S. Department of Commerce
National Technical Information Service
5301 Shawnee Road
Alexandria, VA 22312

Telephone:	(800) 553-6847
Facsimile:	(703) 605-6900
E-Mail:	orders@ntis.gov
Online order:	https://classic.ntis.gov/help/order-methods

ABSTRACT

Theory, simulations, and experiments are presented that demonstrate reconstruction of electromagnetic fields in a cavity from sparse probe measurements. Such techniques are often referred to as virtual sensing, allowing fields at unobserved locations to be predicted. These methods are appropriate for the fundamental and undermoded regimes, providing the ability to estimate fields (and shielding effectiveness) throughout an arbitrarily shaped cavity from a few judiciously spaced probes. A modal simulation method is implemented that allows the response of arbitrarily shaped cavities to be rapidly computed with respect to varying probe locations and slot parameters, enabling statistical analysis of probe placement on reconstruction performance. A cylindrical vessel with numerous probe holes is developed for experiments, referred to as Perforated Vessel 2 (PV2). Experiments are performed on the vessel with and without a steel box inside, where transmit power is delivered into the vessel either through probes (probe injection) or through slots using an external antenna (slot excitation). Simulations and experiments illustrate that when the number of probes is minimal (equal to the number of mode coefficients to be estimated at each frequency), probe placement is critical to avoid missed peaks and to have acceptable reconstruction error. Probe placement becomes less important as the number of probes is increased, but care is still required to avoid probe locations giving poor performance.

This page intentionally left blank.

CONTENTS

LIST OF FIGURES

This page intentionally left blank.

LIST OF TABLES

This page intentionally left blank.

ACRONYMS & DEFINITIONS

3D	Three-dimensional
CAD	Computer assisted design
CCDF	Complementary cumulative distribution function
CDF	Cumulative distribution function
CPU	Central processing unit
CST	Computer Simulation Technology (Microwave Studio Suite)
EM	Electromagnetic(s)
EMI	Electromagnetic interference
FEM	Finite element method
iid	Independent and identically distributed
LDRD	Laboratory Directed Research and Development
MMSE	Minimum mean squared error
OED	Optimal Experiment Design
PEC	Perfect electrical conductor
POD	Proper orthogonal decomposition
POE	Point of entry
PV2	Perforated Vessel 2
Q	Quality factor
RF	Radio frequency
rms	Root mean square
SMA	Sub-miniature version A
SNR	Signal-to-noise ratio
SVD	Singular value decomposition
TE	Transverse electric
TM	Transverse magnetic
VNA	Vector network analyzer

This page intentionally left blank.

1. INTRODUCTION

An understanding of resonant fields in metal enclosures is important in automotive, aerospace, and military applications due to the need to protect sensitive electronic systems from harmful electromagnetic interference (EMI). Full-wave simulation tools allow an analyst to study penetration and resonance of fields in metal enclosures, but such models are often hampered by model uncertainty. Sources of modeling error include enclosure dimensions, positioning of contents, material properties, and points of entry (POEs) parameters. POEs are gaps, slots, and apertures where electromagnetic (EM) energy penetrates into the enclosure.

Direct measurement of fields inside of an enclosure is possible using suitable EM probes. However, due to cost, limitations of measurement equipment, and spatial constraints of the enclosure, only a few sensors can typically be accommodated, providing an incomplete picture of cavity fields. For this reason, measurements are often used to calibrate a numerical model of the cavity, allowing the model to be used as a surrogate for exhaustive measurement campaigns.

The Optimal Experiment Design (OED) Laboratory Directed Research and Development (LDRD) project has as one of its goals the design of EM experiments to maximize information collected from such campaigns. These efforts seek to minimize the required number of sensors and experimental trials, as well as extracting as much information as possible from limited measurements. A key feature of this work is the leveraging of modal descriptions of EM fields in cavities. Modal descriptions represent a very compact basis for fields that may be present, providing many advantages for experiment design and analysis:

- Knowing the modal basis allows optimal sensor locations for experiments to be chosen to maximize information provided by the experiment.
- Once the modal basis is known, the cavity response to EM energy coupled through POEs can be computed very rapidly (in a few seconds), compared to lengthy full-wave simulations. This technique is described in Chapter 2.
- Fields throughout the cavity can be reconstructed from the field sampled at a few locations. This allows three-dimensional (3D) cavity fields to be reconstructed from a measurement with sparse probes. The theory behind this is described in Chapter 3.

The purpose of this SAND report is to document theory, simulations, and experiments that illustrate the use of modal analysis techniques to reconstruct cavity fields in arbitrarily shaped metal enclosures. In addition to the theory described in Chapters 2 and 3, subsequent chapters illustrate the use of the theory through detailed simulations and experiments with a cylindrical cavity:

- Chapter 4 describes bench-top probe-injection simulations and experiments of an empty vessel, illustrating modal reconstruction techniques and the effect of probe placement with closed-form modes.

- Chapter 5 extends the probe-injection investigations to the case of a rectangular box inside of the cylindrical enclosure. This chapter illustrates finding numerical modes for the structure using an eigenfrequency solver. The effect of probe placement is again studied for this geometry.
- Chapter 6 applies the theory to a more practical scenario, where the cylindrical vessel with the rectangular box is placed inside an anechoic chamber, and thin slots on the vessel are excited with an external antenna. The results confirm the ability to reconstruct field at unknown locations in the vessel from sparse probes, as well as the utility of modal simulations in rapidly predicting reconstruction performance.

The report concludes in Chapter 7, providing a summary and future outlook of this work.

2. EFFICIENT MODAL SIMULATION METHODS

This chapter describes techniques for rapidly computing the response of an arbitrarily shaped cavity when excited through probe injection or through POEs in the cavity walls. In both cases, the modal weights must be found for the known excitation on the boundary or in the vessel interior. In the case of probe injection, the impedance matrix of the cavity may be found which links the voltage at outputs to current injected at inputs. The impedance matrix may then be converted to S-parameters [4], which are typically used in microwave measurement and analysis.

These techniques rely on having a modal basis for the cavity of interest. For simple cavity shapes, such as a cylinder (Appendix B) or a rectangular box, modes may be found using closed-form expressions. For cavities with arbitrary shapes, a numerical eigenfrequency solver is required. However, even when modes must be found numerically, the modes only need to be found once for a structure of interest, and the response for arbitrary injection probes, POEs, angles of incidence, and sensor locations can be rapidly computed thereafter.

Electric field in a resonant cavity can be written as

$$\overline{E}(\overline{r}) = \sum_n e_n \overline{E}_n(\overline{r}), \tag{2.1}$$

where $\overline{r}$ is a spatial coordinate, n is the index for the mode, $\overline{E}_n(\overline{r})$ is the nth spatial function from the modal basis, and e_n is the nth mode coefficient.

2.1. Probe Injection

Given that the cavity is excited with electric currents (like the monopole probes considered in this work), we have from [1] that

$$e_n = -j \frac{k\eta}{k_n^2 - k^2\left(1 - \frac{1-j}{Q_n}\right)} q_n, \tag{2.2}$$

where $k = \omega\sqrt{\mu\epsilon}$ is the wave number, $\omega = 2\pi f$ is the circular excitation frequency, $\eta = \sqrt{\mu/\epsilon}$, $k_n = \omega_n\sqrt{\mu\epsilon}$ is the wavenumber at the nth circular modal frequency $\omega_n = 2\pi f_n$, Q_n is the quality factor of the nth mode, and

$$q_n = \frac{\int_V \overline{J}(\overline{r}) \cdot \overline{E}_n(\overline{r}) dV}{\int_V \overline{E}_n(\overline{r}) \cdot \overline{E}_n(\overline{r}) dV}, \tag{2.3}$$

where $\overline{J}(\overline{r})$ is a volumetric electric current density. Note that unlike the expressions in [1], the expressions here do not require the modal basis to be previously normalized.

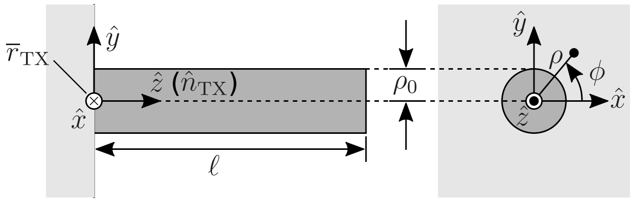

Figure 2-1. A single monopole probe in a coordinate system local to the probe. Note that $\hat{n}_{\mathrm{TX}}$ and $\overline{r}_{\mathrm{TX}}$ are the orientation and base coordinate of the probe in global coordinates.

Fig. 2-1 shows a single cylindrical monopole probe in a local coordinate system, where $\hat{z}$ is along the axis of the probe, ρ_0 is the radius of the probe, and ℓ is the length of the probe. In global coordinates, we will let $\hat{n}_{\mathrm{TX}}$ be along the axis of the probe and $\overline{r}_{\mathrm{TX}}$ be the coordinate of the base of the probe. For monopole probes that are small with respect to the wavelength, we model the current as residing only on the surface of the probe, remaining constant with respect to ϕ, and varying linearly with respect to z. Mathematically, the current density of the probe in local coordinates is

$$\overline{J}(\overline{r}) = \frac{I_{\mathrm{TX}}}{2\pi\rho_0}\delta(\rho - \rho_0)\, f_{\mathrm{triangle}}(\ell, z)\, \hat{z}, \tag{2.4}$$

where

$$f_{\mathrm{triangle}}(\ell, z) = \begin{cases} 1 - z/\ell, & 0 \leq z \leq \ell, \\ 0, & \text{otherwise}, \end{cases} \tag{2.5}$$

and I_{TX} is the input current at the base of the transmit probe. A probe length of ℓ =1 cm was used throughout this work, for both simulations and experiments.

Assuming modal fields do not change appreciably over the length of the short probe, we have

$$q_n = A_n^{-1} \int_V \overline{J}(\overline{r}) \cdot \overline{E}_n(\overline{r}) dV \tag{2.6}$$

$$\approx A_n^{-1} I_{\mathrm{TX}}\ (\ell/2)\ [\hat{n}_{\mathrm{TX}} \cdot \overline{E}_n(\overline{r}_{\mathrm{TX}})], \tag{2.7}$$

where

$$A_n = \int_V \overline{E}_n(\overline{r}) \cdot \overline{E}_n(\overline{r}) dV. \tag{2.8}$$

The expressions above allow the field to be computed everywhere in the cavity at an arbitrary circular frequency ω in response to an input current of I_{TX}. The open-circuit voltage at a receive probe is then given by

$$V_{\mathrm{RX,oc}} = -(\ell/2)\overline{E}(\overline{r}_{\mathrm{RX}}) \cdot \hat{n}_{\mathrm{RX}}, \tag{2.9}$$

where $\overline{r}_{\mathrm{RX}}$ and $\hat{n}_{\mathrm{RX}}$ are the global coordinate and orientation of the receive probe.

2.2. Impedance and Scattering Matrix Computation

For a set of multiple probes, we can use the the previously developed expressions to compute off-diagonal elements of the impedance matrix. The computation is performed as

$$Z_{mn} = \left. \frac{V_{\mathrm{RX,oc},m}}{I_{\mathrm{TX},n}} \right|_{I_{\mathrm{TX},i}=0, \forall i \neq n}, \tag{2.10}$$

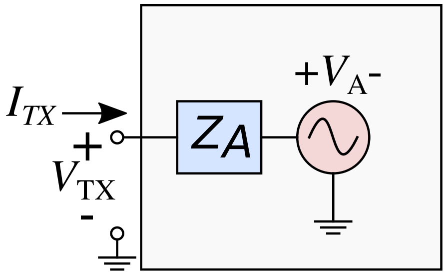

Figure 2-2. Model of a probe that handles both the transmit and receive operation of a driven element.

where $V_{\text{RX,oc},m}$ is the receive open-circuit voltage on the mth probe, and $I_{\text{TX},n}$ is the input transmit current on the nth probe. The meaning of this expression is that we set one probe current at a time to be nonzero and compute the open-circuit voltages seen at all the other probes. This expression is only correct for the case of $m \neq n$.

For the diagonal elements of the impedance matrix, we need to find the total voltage (not open-circuit voltage) at each probe for a nonzero input current into the probe. This can be accomplished considering the model in Figure 2-2. The impedance Z_A is the input impedance of the monopole probe over an infinite ground plane, which is the impedance seen looking into the probe when $V_A = 0$. In the cavity, reflections from the walls will cause $V_A \neq 0$. Driving a current I_{TX} on probe m with other currents set to zero, we can compute cavity fields as before, and the open-circuit voltage that would be present at element m for that field is

$$V_A = V_{\text{RX,oc},m} = -(\ell/2)\overline{E}(\overline{r}_{\text{RX},m}) \cdot \hat{n}_{\text{RX},m}. \tag{2.11}$$

The total voltage at the probe depends on Z_A according to

$$V_{\text{RX},m} = V_A + Z_{A,m} I_{\text{TX},m}, \tag{2.12}$$

where $Z_{A,m}$ is the input impedance of the mth probe over an infinite ground plane. The impedance looking into the driven element is therefore

$$Z_{mm} = \left.\frac{V_{\text{RX},m}}{I_{\text{TX},m}}\right|_{I_{\text{TX},i}=0,\forall i\neq m} = Z_{A,m} + \left.\frac{V_{\text{RX,oc},m}}{I_{\text{TX},m}}\right|_{I_{\text{TX},i}=0,\forall i\neq m}. \tag{2.13}$$

We can then unify (2.10) and (2.13) into the single expression

$$Z_{mn} = \delta_{mn} Z_{A,m} + \left.\frac{V_{\text{RX,oc},m}}{I_{\text{TX},n}}\right|_{I_{\text{TX},i}=0,\forall i\neq n}, \tag{2.14}$$

where δ_{mn} is the Kronecker delta function. This expression is now correct for all impedance matrix elements.

Scattering parameters (S-parameters) may be computed from the impedance matrix using

$$\mathbf{S} = (\mathbf{Z} + Z_0\mathbf{I})^{-1}(\mathbf{Z} - Z_0\mathbf{I}), \tag{2.15}$$

where $\mathbf{I}$ is the identity matrix, and Z_0 is the normalizing impedance, which is assumed to be the same here for all ports.

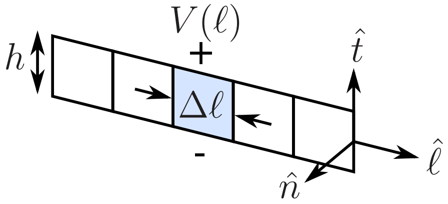

Figure 2-3. Model of a slot that can be used to drive cavity modes. Note that $\hat{n}$ points into the cavity.

2.3. Slot Excitation

We finally consider the case when the cavity is excited from apertures or slots, which coupling can be modeled using equivalent magnetic currents. If the electric field distribution at a slot or aperture is known, it can be replaced with an effective magnetic current according to

$$\overline{M} = -\hat{n} \times \overline{E}_{\text{ap}}, \tag{2.16}$$

where $\overline{E}_{\text{ap}}$ is the field at the aperture. Consider the thin slot shown in Figure 2-3. On the ℓth segment of the slot, the voltage across the slot is related to the field in the slot according to

$$\overline{E}_{\text{slot}}(\ell) = -\frac{V(\ell)}{h}\hat{t}, \tag{2.17}$$

where $V(\ell)$ is voltage, h is the height of the slot, and $\hat{t}$ is the tangential direction along the height dimension. We can compute the effective magnetic current as

$$\begin{aligned} \overline{M} &= -\hat{n} \times \left(-\frac{V(\ell)}{h}\right)\hat{t} && (2.18)\\ &= -\hat{\ell}\frac{V(\ell)}{h}, && (2.19) \end{aligned}$$

where $\hat{\ell}$ is the unit vector along the length of the slot.

The coupling of the slot fields (magnetic currents) to cavity modes is given by [1]

$$e_n = h_n = -j\frac{k/\eta}{k_n^2 - k^2\left(1 - \frac{1-j}{Q_n}\right)}q_n, \tag{2.20}$$

where

$$q_n = \frac{\int_V \overline{M}(\overline{r}) \cdot \overline{H}_n(\overline{r})dV}{\int_V \overline{H}_n(\overline{r}) \cdot \overline{H}_n(\overline{r})dV}. \tag{2.21}$$

Note that in our development the coefficient for magnetic field h_n is the same as that of the electric field e_n, since modes are found as pairs of $\overline{E}_n$ and $\overline{H}_n$ with the proper relative scaling, rather than individually normalizing $\overline{E}_n$ and $\overline{H}_n$ as is done in [1].

For the thin slot model, considering only the ℓth slot element we have

$$\begin{aligned} q_n &= B_n^{-1}\int_V \overline{M}(\overline{r}) \cdot \overline{H}_n(\overline{r})dV && (2.22)\\ &\approx -B_n^{-1}\overline{H}_n(\overline{r}_{\text{slot},\ell}) \cdot \hat{\ell}\, \Delta\ell\, V(\ell), && (2.23) \end{aligned}$$

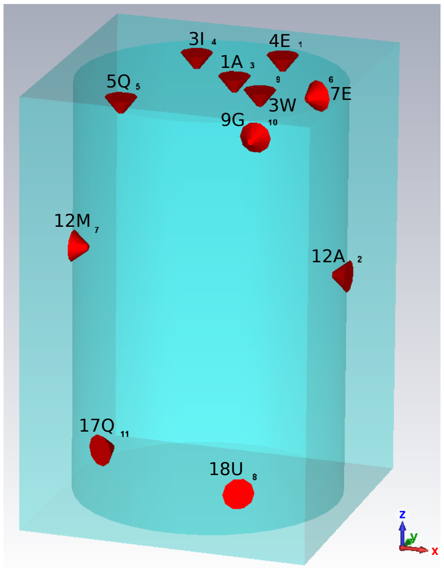

Figure 2-4. CST model with probes placed at the *heuristic* locations. The small numbers near each port represent CST assigned port numbers, while the large labels use the grid system from Appendix A.

where $\overline{r}_{\text{slot},\ell}$ is the coordinate at the center of the ℓth slot element, $\Delta\ell$ is the length of the slot element, and

$$B_n = \int_V \overline{H}_n(\overline{r}) \cdot \overline{H}_n(\overline{r}) dV. \tag{2.24}$$

To compute q_n due to all slot elements, we sum their contributions from (2.22).

2.4. Example 1: Probe-injection Response of Empty PV2

This section validates the theory in Section 2.1 by analyzing the empty PV2, which has a simple cylindrical cavity shape. The theory is first applied to the case when closed-form modes are used, computed using expressions in Appendix B. The theory is then tested for numerical modes of the same structure, where the COMSOL workflow described in Appendix C was used. Responses computed with the efficient modal simulation theory are compared with full-wave CST Microwave Studio simulations of the same structure.

2.4.1. Full-wave CST Simulation

Fig. 2-4 shows the CST model of PV2 with injection probes placed at locations 4E and 12A, corresponding to CST Ports 1 and 2, respectively. Receive probes are placed at the nine locations 1A, 3I, 5Q, 7E, 12M, 18U, 3W, 9G, 17Q, comprising Ports 3 to 11, respectively. These probe locations correspond to those in the heuristic probe set described in Chapter 4. Only the two injection probes were excited in the CST simulation to save simulation time, which allows the S-parameters S_{mn} to be computed for $n = 1, 2$ and $m = 1, \ldots, 11$.

The mesh of the cylinder interior required 95k tetrahedra. For a sweep from 500 MHz to 2 GHz, the adaptive sweep in CST used 1905 frequency points, and the simulation time was 13 hours using 16 cores on an Intel Xeon Platinum 8176 CPU at 2.10 GHz.

2.4.2. Modal Simulation with a Closed-form Basis

The modal framework described in this chapter was applied next, using modal frequencies and mode shapes computed using closed-form expressions from Appendix B. A total of 134 modes were identified from 500 MHz to 2 GHz, of which 18 were unobservable TE modes. Here *unobservable* means modes that have no normal electric field component anywhere on the cavity walls. Modal responses were computed from 500 MHz to 2 GHz using 16351 frequency points (92-kHz step). The full 11×11 S-parameter matrix for the same probe locations analyzed previously required only 1.3 seconds running in MATLAB on a single core.

A few of the S-parameters are plotted in Fig. 2-5. As can be seen, the dominant resonances and overall response are well captured using the efficient modal simulation technique. There are some discrepancies at low frequency at very low power, especially when a near zero occurs there. The zero occurs when two or more modes cancel in between the resonances. We suspect that the reason for the discrepancy is that one simulation tool is including a very weak pole at low frequency while the other tool has not included it.

2.4.3. Modal Simulation with a Numerical Basis

The modal framework was applied again, except this time numerical modes were computed for the cylinder using the COMSOL workflow described in Appendix C. The mesh was generated using the default physics-controlled mesh, resulting in 19k tetrahedra. The COMSOL eigenfrequency simulation required 7 minutes using 12 cores on an Intel Xeon Platinum 8176 CPU at 2.10 GHz. Interestingly, COMSOL only finds 68 modes in the 500 to 2 GHz frequency range. Perhaps to find weaker modes, the solution tolerance needs to be adjusted in COMSOL.

After post-processing COMSOL data, the numerical framework was used to compute probe-injection S-parameters from 560 MHz to 2 GHz at 16351 points. The run time for the full 11×11 S-parameter computation in MATLAB at 16351 frequency points takes only 1.2 seconds.

A few of the S-parameters are plotted in Fig. 2-5. As can be seen, the dominant resonances and overall response are well captured using the efficient modal simulation technique.

2.4.4. Peak Resolution

When comparing the resonant responses of the different solution methods, the amplitude of resonant peaks can sometimes appear to be in error, when in fact the discrepancy is due to resolution of the frequency sampling. Fig. 2-7 compares the peaks of the three methods employed in the empty vessel example for $S_{11,2}$ near the first resonance at 685 MHz. We have chosen this peak and port combination since there is approximately 5 dB of error seen in the original data (92 kHz frequency

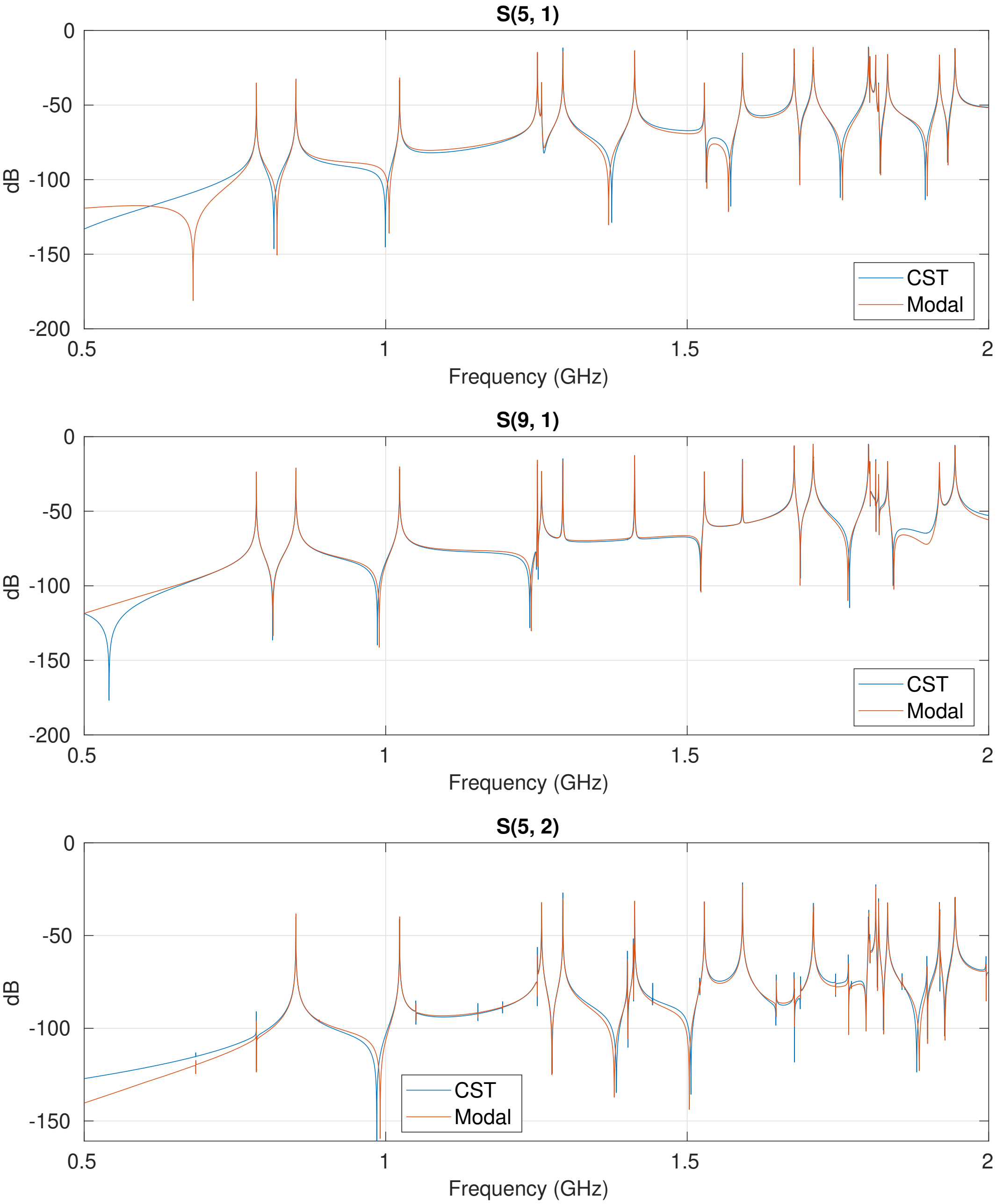
S(5, 1)

S(9, 1)

S(5, 2)

Figure 2-5. Comparison of S-parameters computed with full-wave CST simulations and the fast closed-form modal solution technique for probe injection of the PV2 model. Port numbers represent those assigned by CST and are shown as small numbers in Fig. 2-4.

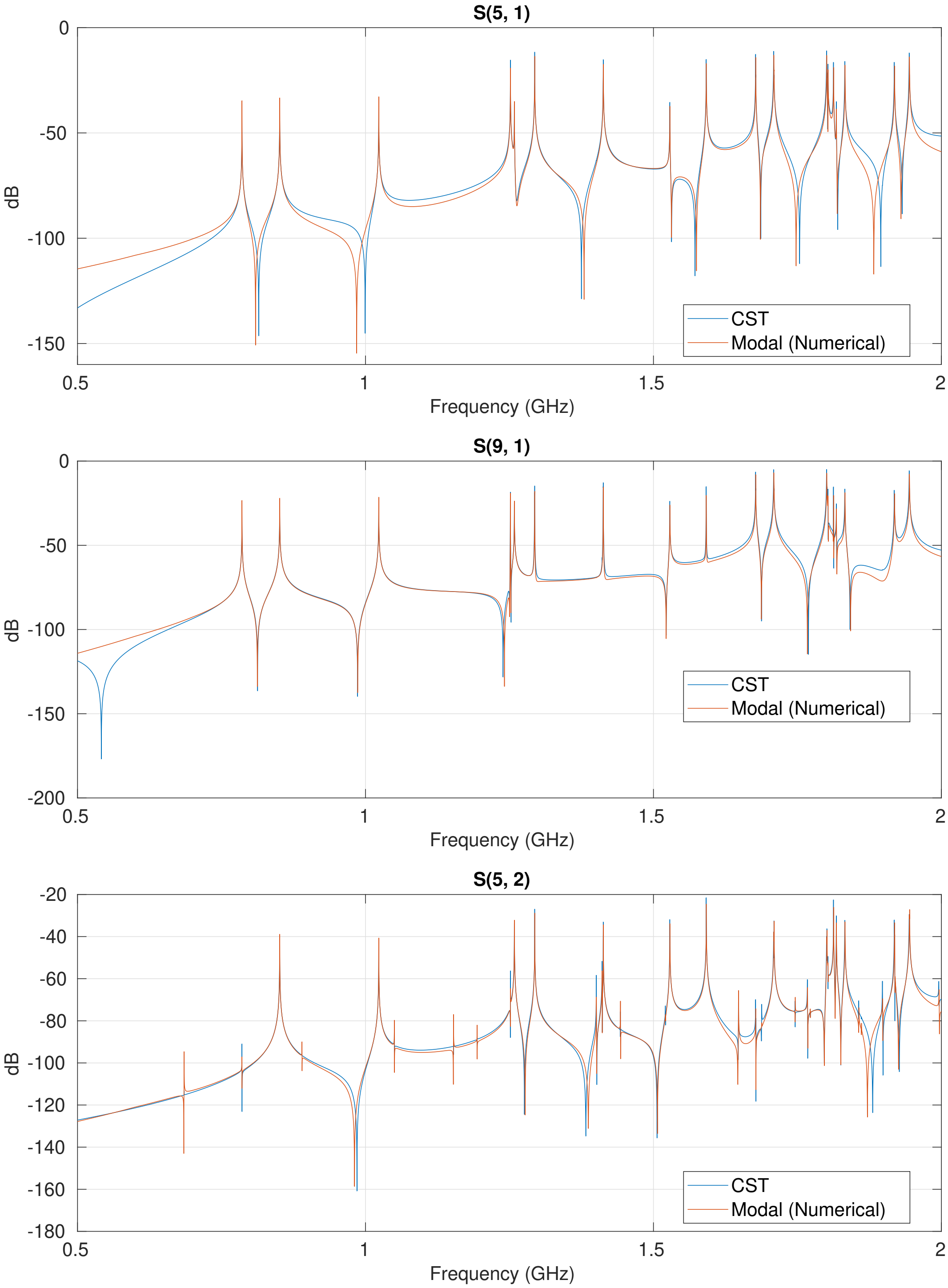

Figure 2-6. Comparison of S-parameters computed with full-wave CST simulations and fast numerical modal solutions for probe injection of the PV2 model.

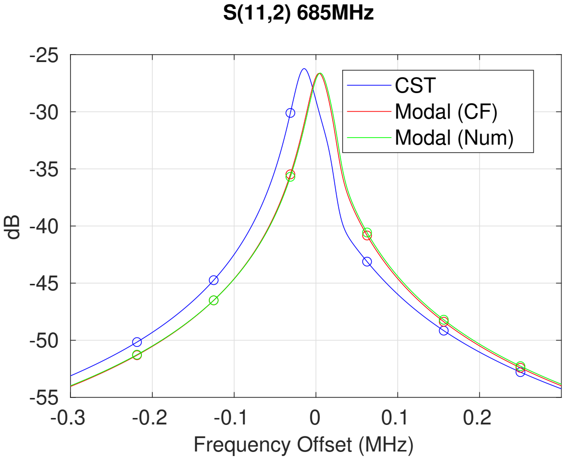

Figure 2-7. Comparison of $S_{11,2}$ near the lowest resonance at 685 MHz for full-wave CST simulations, as well as closed-form and numerical modal simulation.

step), as indicated with symbols in the plot. Performing rational interpolation near this peak at a resolution of 1 kHz gives the smooth curves shown in the plot. The remaining error at the peak after interpolation is only 0.4 dB.

2.5. Example 2: Slot Excitation of Empty PV2

In this section, we turn our attention to excitation of the empty PV2 using slots. We will validate the slot excitation formulation in Section 2.3 by simulating the geometry shown in Fig. 2-8. The computer assisted design (CAD) geometry was drawn in CUBIT with a thin 1 mm ring around the center of the vessel, partitioned in 2° segments.

2.5.1. Full-wave COMSOL Simulation

This geometry was simulated in COMSOL, where a forced electric-field boundary condition was used to impose 1 V/m on a single 2° patch of the ring. The full-wave simulation was run with a frequency sweep from 500 MHz to 2 GHz with a fixed 10 MHz step (151 points). The physics-controlled meshing generated a mesh size of 129k tetrahedra. Simulation required 4.5 hours to complete using 16 cores on an Intel Xeon Platinum 8176 CPU at 2.10 GHz. Rational interpolation was used afterwards to reduce the effective frequency step to 100 kHz. Near fields normal to the cavity wall were sampled at the nine probe positions corresponding to the heuristic probe set and measurement test ports (1A, 3I, 5Q, 7E, 12M, 18U, 3W, 9G, 17Q). These were converted to probe voltages assuming an effective length of the probes of 1 cm/2 = 0.5 cm.

2.5.2. Modal Simulation with a Closed-form Basis

The slot-to-probe modal analysis technique from Section 2.3 was used with a closed-form modal basis. Computation at 15001 frequency points (100 kHz step) from 500 MHz to 2 GHz from a

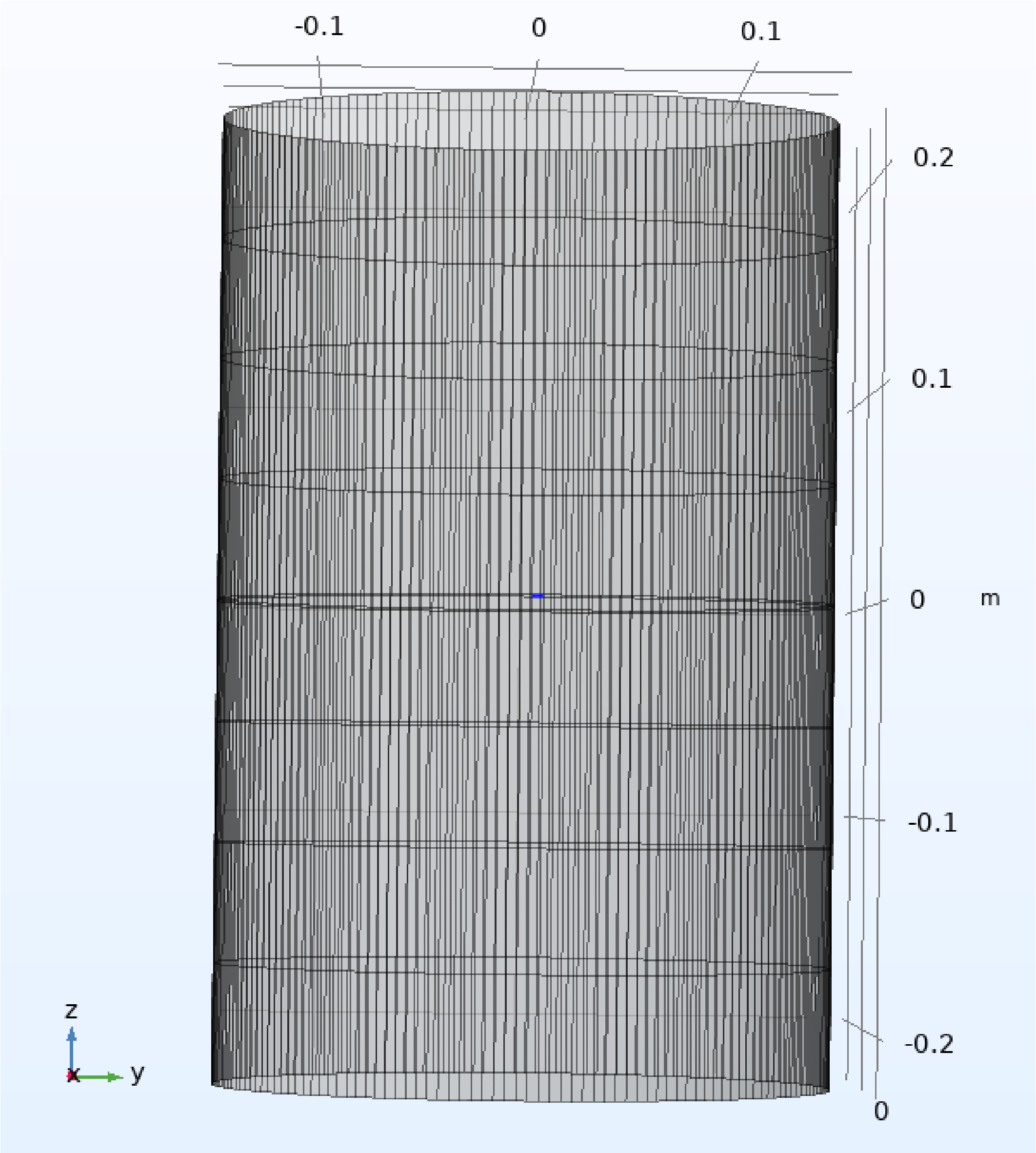

Figure 2-8. Empty cylinder geometry in COMSOL, where the CAD model has been drawn with a small ring on the center perimeter to simulate a thin slot. The small blue rectangle on the ring is the driven element.

single slot element to the nine probes only required 0.35 seconds in MATLAB on a single core.

Full-wave simulation of the slot-to-probe response is compared with the modal solution in Fig. 2-9. Good agreement is seen for most of the modes. However, some of the weaker modes are not being captured. A mode at 692 MHz is perhaps the most obvious example. This is possibly due to sampling fields right at the cylindrical wall in the closed-form expressions, whereas in COMSOL fields are computed slightly away from the walls to avoid numerical problems. This may be the reason that some additional weak modes are observed in the full-wave simulation.

2.6. Example 3: Probe-injection Response of Box in PV2

In this example, we use the numerical mode probe-injection framework to analyze a geometry for which only a numerical modal basis is possible. Fig. 2-10 shows the geometry, consisting of a metal box centered in the bottom of PV2. A numerical modal basis is found in COMSOL using this model.

For this example, a full-wave simulation was not performed, and so we compare with probe-injection measurements that were collected for the box-in-PV2 configuration, as described in Chapter 6. S-parameter measurements were collected with a VNA from 560 MHz to 20 GHz using a 100 kHz step. Fig. 2-11 compares the measured response of the box-in-PV2 configuration with a direct measurement for the raw 100 kHz frequency resolution. Although the responses fit quite well, the peaks are not always at the same level for the different resonances. Part of this is due to insufficient frequency resolution, as was described previously. However, there is also more uncertainty in the box-in-PV2 model, since the box was manually placed and held to the bottom with copper tape. Further, we have not simulated the box as having a different conductivity (steel) as compared to the vessel walls.

2.7. Conclusion

This chapter has described a modal simulation technique that provides very efficient simulation of electromagnetic fields in enclosures. The main strength of the technique is that the modal structure only needs to be computed once with a numerical simulation. After this, arbitrary slots and probes may be placed, and the response rapidly computed.

The efficient nature of the modal simulation method provides many orders of magnitude improvement over full-wave simulation for each probe/slot configuration. This efficiency enables thousands of different probe configurations to be rapidly simulated in Monte Carlo studies described in Chapters 4-6. Note that such studies would be virtually impossible with traditional full-wave simulation techniques.

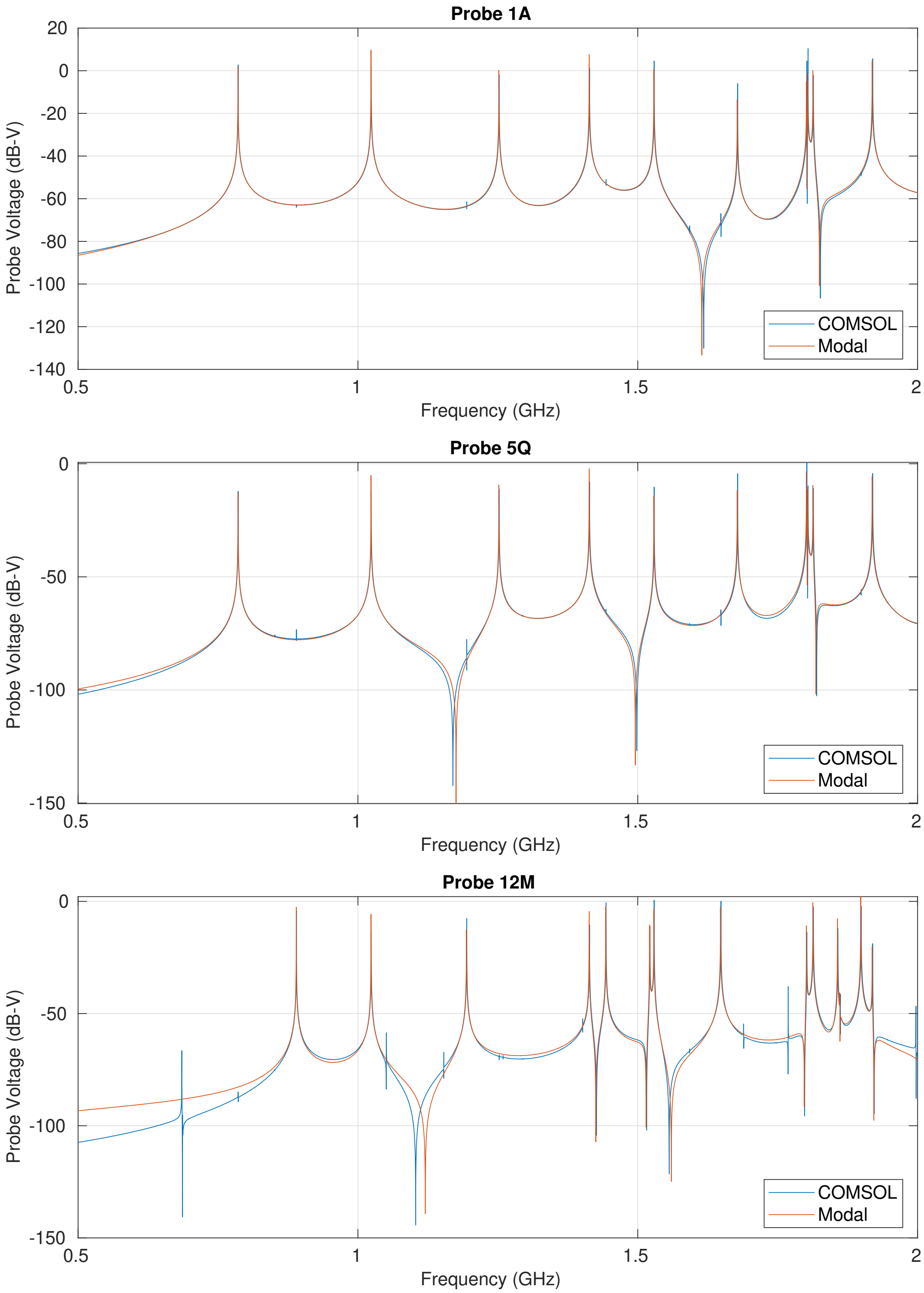

Figure 2-9. Probe voltages for simulations of empty PV2 with a single 1 V/m slot element excited on the wall. A full-wave COMSOL simulation is compared with the slot-to-probe analysis technique using a closed-form basis.

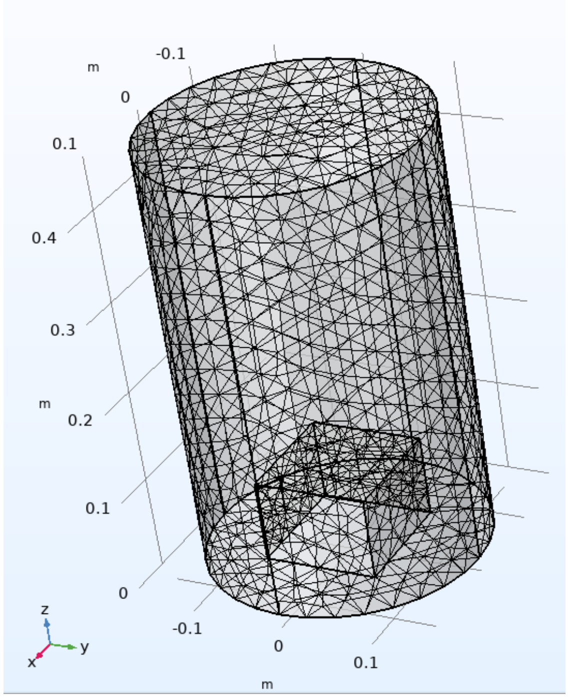

Figure 2-10. Box-in-PV2 geometry used to find modal solutions in COMSOL.

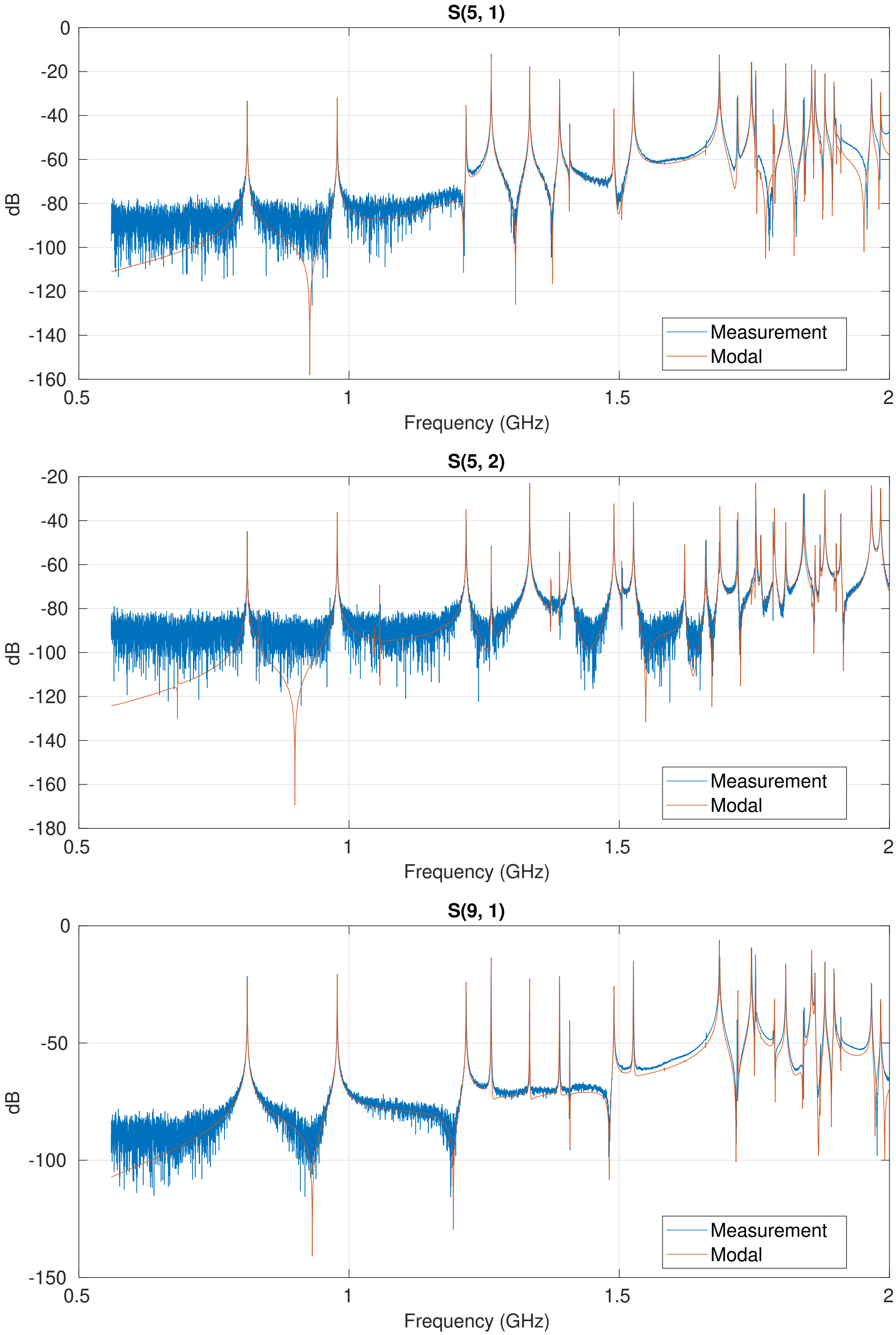

Figure 2-11. Comparison of measured S-parameters with the numerical mode solution for probe injection of the box-in-PV2 model.

3. FIELD RECONSTRUCTION THEORY

This chapter describes methods for reconstructing fields throughout a cavity from sparse sensor measurements with probes. The methods rely on having a basis for cavity fields with no more basis functions than the number of probes. This can be easily satisfied in the fundamental and undermoded regimes, where the degrees of freedom of the cavity fields are sufficiently small.

The reconstruction can be performed at unmeasured candidate probe locations, as is done in the simulations and experiments in Chapters 4-6, as well as points throughout the cavity volume. Such methods also allow worst-case shielding effectiveness to be predicted from a few judiciously chosen probe locations.

3.1. Basis Selection

This section describes the basic concepts and notation required for generating a suitable basis used for reconstruction.

3.1.1. Spatial Basis

Electric field in the cavity is assumed to be a sum of *spatial basis* functions according to

$$\overline{E}(\overline{r}) = \sum_n e_n \overline{E}_n(\overline{r}), \tag{3.1}$$

where $\overline{r}$ is a spatial coordinate, $\overline{E}_n(\overline{r})$ is the nth full-volume spatial basis function, and e_n is the nth basis coefficient.

In practice, the field may be sampled (estimated) at a sparse set of N_P probe locations. Typically, a single probe can only sense one component of the electric or magnetic field, returning a complex scalar for each frequency point sampled. At a single frequency, we denote $\mathbf{p}$ as the vector of *observed* probe signals. For illustration, assuming normal electric field probes (monopoles) on the surface of the cavity, the ith probe signal is

$$p_i = \hat{n}(\overline{r}_i) \cdot \overline{E}(\overline{r}_i), \tag{3.2}$$

where $\overline{r}_i$ is the location of the sensor, and $\hat{n}(\overline{r}_i)$ is the normal to the surface at the probe.

We are interested in reconstructing fields at *unobserved* locations, and we denote $\mathbf{y}$ to be the vector of N_Y unobserved scalar quantities at a single frequency. One example of a practical $\mathbf{y}$ of interest is a vector of potential probe signals at locations where physical probes have not actually been placed, but whose response we wish to predict. For normal electric field probes we have

$$y_i = \hat{n}(\overline{r}'_i) \cdot \overline{E}(\overline{r}'_i), \tag{3.3}$$

where $\overline{r}'_i$ is the spatial position of a candidate probe location we are assuming is not observed. In the studies in Chapters 4-6, we use this designation of unobserved signals to predict field at certain test points, which are then measured and/or simulated, allowing the error in those predictions to be quantified.

Another unobserved signal of practical interest is the field at arbitrary points throughout a cavity's interior which may be very difficult or impossible to measure in practice. In this case we could denote

$$\mathbf{y} = \begin{bmatrix} \overline{E}(\overline{r}'_1) \\ \overline{E}(\overline{r}'_2) \\ \vdots \\ \overline{E}(\overline{r}'_{N_Y}) \end{bmatrix}, \tag{3.4}$$

where $\overline{E}(\overline{r}) = [E_x(\overline{r})E_y(\overline{r})E_z(\overline{r})]^T$ is the 3D field vector at spatial location $\overline{r}$, and $\{\cdot\}^T$ denotes transpose. Here, we would have $N_Y = 3N$, where N is the total number of points on a Cartesian grid that samples the entire volume, and $\mathbf{y}$ becomes a stacked vector of the 3D electric field at all points on that grid.

For the purpose of field reconstruction, we need to establish a correspondence between the unobserved and observed quantities. Specifically, we identify basis vectors $\mathbf{p}_k$ and $\mathbf{y}_k$, which are arrays of observed and unobserved signals that occur together, and $k = 1, \ldots, N_B$. This set of vectors is referred to as the *reconstruction basis* or just *basis* for short. We can organize the basis vectors into basis matrices, namely

$$\mathbf{P} = [\mathbf{p}_1 \; \mathbf{p}_2 \; \ldots \; \mathbf{p}_{N_B}] \tag{3.5}$$

$$\mathbf{Y} = [\mathbf{y}_1 \; \mathbf{y}_2 \; \ldots \; \mathbf{y}_{N_B}]. \tag{3.6}$$

Considering our example of normal electric field probes for both observed and unobserved signals, we have

$$p_{ik} = \hat{n}(\overline{r}_i) \cdot \overline{E}^{(k)}(\overline{r}_i), \tag{3.7}$$

$$y_{ik} = \hat{n}(\overline{r}'_i) \cdot \overline{E}^{(k)}(\overline{r}'_i), \tag{3.8}$$

where the superscript (k) on the field vector indicates the kth excitation of the cavity, which could denote a mode index, frequency, angle of incidence, incident polarization, etc. The main point is that for a single excitation, $\mathbf{p}_k$ and $\mathbf{y}_k$ are not uniquely determined, but rather depend on the same field quantity $\overline{E}^{(k)}(\overline{r})$. In summary, our reconstruction basis consists of matrices $\mathbf{P}$ and $\mathbf{Y}$, whose columns represent corresponding vectors of observed and unobserved signals, respectively.

A natural choice for our reconstruction basis is to tie it back to the original spatial field basis, according to

$$p_{in} = \hat{n}(\overline{r}_i) \cdot \overline{E}_n(\overline{r}_i), \tag{3.9}$$

$$y_{in} = \hat{n}(\overline{r}'_i) \cdot \overline{E}_n(\overline{r}'_i). \tag{3.10}$$

Thus, if we can find a spatial field basis with good properties, it is trivial to convert this into a reconstruction basis.

3.1.2. Basis Orthogonalization

Depending on how a basis is constructed, there may be undesired redundancy. A proper orthogonal decomposition (POD) may be used to make the basis significantly more compact. This section describes how this can be accomplished for an arbitrary basis, represented by **P** and **Y**, by employing the singular value decomposition (SVD).

Stacking the observed and unobserved basis vectors, we can construct the joint basis

$$\mathbf{A} = \begin{bmatrix} \mathbf{P} \\ \mathbf{Y} \end{bmatrix}. \tag{3.11}$$

Performing the SVD of this joint basis, we have

$$\mathbf{A} = \mathbf{U}\mathbf{S}\mathbf{V}^H = \begin{bmatrix} \mathbf{U}_1 \; \mathbf{U}_0 \end{bmatrix} \mathbf{S}\mathbf{V}^H, \tag{3.12}$$

where $\{\cdot\}^H$ is the Hermitian (conjugate transpose) operator. We retain M columns of **U** that are associated with the M largest singular values in **S**, denoted $\mathbf{U}_1$. We can partition $\mathbf{U}_1$ into rows of observable and unobservable signals as

$$\mathbf{U}_1 = \begin{bmatrix} \mathbf{P}' \\ \mathbf{Y}' \end{bmatrix}, \tag{3.13}$$

where the $\mathbf{P}'$ and $\mathbf{Y}'$ represent the new POD basis matrices for observed and unobserved signals, respectively.

3.1.3. Modal Basis

Finding a modal basis for fields in the cavity is perhaps the most efficient way to represent the limited degrees of freedom that may exist. In some cases we may have an efficient way of finding modes of a structure, such as closed-form expressions for simple geometries or reduced-order solvers for shapes with symmetry. For arbitrary shapes, we can use a numerical eigenfrequency solver, such as the workflow described in Appendix C.

For a modal basis, we assume there are N_{mode} modes in the frequency band of interest. We will let f_n denote the nth resonant frequency (or eigenfrequency) of the cavity, which has a corresponding spatial basis function $\overline{E}_n(\overline{r})$.

One drawback of a modal basis for cavity fields is that perturbation of the modal fields due to POEs is not captured. Also, in cases where we have high density of modes, the number of basis functions may be too large to estimate modal coefficients with sparse probes.

3.1.4. Data-Driven Basis

The idea of a data-driven basis is to perform full-wave simulation of the cavity with POEs present to empirically generate a spatial basis. To sample the space of possible solutions, we generate N_S parameter sets, where fixed incident field and POE parameters are chosen for each set. Performing a frequency sweep over the band of interest at N_F frequencies for each parameter set yields $N = N_S N_F$ spatial basis functions $\overline{E}_n(\overline{r})$.

3.2. Pseudoinverse Reconstruction

Assuming that our basis spans all possible signals of interest in our cavity, we can write arbitrary observed ($\mathbf{p}$) and corresponding unobserved ($\mathbf{y}$) signals as

$$\mathbf{p} = \mathbf{P}\mathbf{x}, \tag{3.14}$$

$$\mathbf{y} = \mathbf{Y}\mathbf{x}, \tag{3.15}$$

where $\mathbf{x}$ is a vector of complex basis weights. Assuming that the number of probes at observed locations is at least as large as the number of basis functions, we can compute

$$\mathbf{x} = \mathbf{P}^{+}\mathbf{p}, \tag{3.16}$$

where $\{\cdot\}^{+}$ is the pseudoinverse. Unobserved signals may then be computed as

$$\mathbf{y} = \mathbf{Y}\mathbf{P}^{+}\mathbf{p}. \tag{3.17}$$

For the pseudoinverse method to work well, we need the number of basis functions to be no larger than the number of probes. In the case of a modal basis and a wide frequency range, we will likely have too many modes to satisfy this criterion. One remedy is to limit the number of modes used when reconstructing field at each frequency. Specifically, when reconstructing field at frequency f we limit the number of modes used in the reconstruction basis to the N'_{mode} nearest modes (those having the smallest $|f - f_n|$), where $N'_{\text{mode}} \leq N_P$. For a data-driven basis, the number of basis functions for reconstruction at each f can be limited by using basis orthogonalization and by limiting frequency samples to a small neighborhood around the reconstruction frequency.

Note that the analysis so far has not considered the noise of the probe signals, which is always present in practice. Such noise, coupled with the pseudoinverse estimation method, may lead to significant noise amplification and poor reconstruction performance. Maximum likelihood (ML) estimation is a theoretically optimal approach, which is outlined in the next section.

3.3. Maximum Likelihood Estimation

In this section we illustrate one optimal approach that is expected to have significantly improved performance over the pseudoinverse estimator, namely the ML estimator. We augment the previous model slightly,

$$\mathbf{p} = \mathbf{P}\mathbf{x} + \mathbf{n}, \tag{3.18}$$

$$\mathbf{y} = \mathbf{Y}\mathbf{x}, \tag{3.19}$$

where $\mathbf{n}$ is a vector of independent and identically distributed (iid) zero-mean complex Gaussian noise samples. Our goal is to estimate $\mathbf{y}$ from noisy observations of $\mathbf{p}$. If we assume that the the modal coefficients $\mathbf{x}$ have a joint zero-mean complex Gaussian distribution, $\mathbf{p}$ and $\mathbf{y}$ will also be jointly zero-mean complex Gaussian. Since we observe $\mathbf{p}$, we are interested in the distribution of $\mathbf{y}$ conditioned on $\mathbf{p}$. Choosing the $\mathbf{y} = \mathbf{y}_{\text{opt}}$ that maximizes the conditional probability density function is then our ML estimate. The multivariate complex Gaussian density function is maximized when $\mathbf{y}$ is equal to the mean of the distribution, or $\mathbf{y}_{\text{opt}} = \boldsymbol{\mu}_y$, where $\boldsymbol{\mu}_y$ is the mean of $\mathbf{y}$.

From [2], the mean of $\mathbf{y}$ conditioned on $\mathbf{p}$ is

$$\boldsymbol{\mu}_{y|p} = \boldsymbol{\mu}_y + \mathbf{R}_{yp}\mathbf{R}_{pp}^{-1}(\mathbf{p} - \boldsymbol{\mu}_p), \tag{3.20}$$

where

$$\mathbf{R}_{ab} = \mathrm{E}\left\{(\mathbf{a} - \boldsymbol{\mu}_a)(\mathbf{b} - \boldsymbol{\mu}_b)^H\right\} \tag{3.21}$$

is the covariance matrix of vectors $\mathbf{a}$ and $\mathbf{b}$,

$$\boldsymbol{\mu}_c = \mathrm{E}\left\{\mathbf{c}\right\} \tag{3.22}$$

is the mean of vector $\mathbf{c}$, and $\mathrm{E}\left\{\cdot\right\}$ represents expectation. Substituting our model from (3.18) and (3.19) into (3.20), and assuming the independence of noise and modal coefficients, we have

$$\mathbf{y}_{\text{opt}} = \boldsymbol{\mu}_{y|p} = \mathbf{Y}\mathbf{R}_{xx}\mathbf{P}^H(\mathbf{P}\mathbf{R}_{xx}\mathbf{P}^H + \sigma^2\mathbf{I})^{-1}\mathbf{p}, \tag{3.23}$$

where σ^2 is the noise variance, and $\mathbf{I}$ is the identity matrix.

It is instructive to consider the operation of (3.23). If we let the noise approach zero, and model the modal coefficients as iid Gaussian ($\mathbf{R}_{xx} = \mathbf{I}$), we obtain the pseudoinverse estimator from the last section. This means if we are in a very high signal-to-noise (SNR) environment and all modes in $\mathbf{R}_{xx}$ are strongly coupled to the reconstruction frequency, the pseudoinverse should have good performance.

On the other hand, if we have significant noise, the $\sigma^2\mathbf{I}$ term will tend to regularize the inverse by increasing the diagonal entries of $\mathbf{R}_{pp}$ before taking the inverse. Also, if the power of some modes (diagonal entries of $\mathbf{R}_{xx}$) is small relative to the noise, these modes will be de-emphasized due to the regularization term $\sigma^2\mathbf{I}$.

It is also interesting to consider how we might practically implement the ML estimator. One option is to do as we have done with the pseudoinverse estimator, where we restrict our attention to the closest N'_{mode} modes to a given reconstruction frequency. This would mean taking a subset of the rows and columns of $\mathbf{R}_{xx}$ for each reconstruction performed. Another option is to simply use the full $\mathbf{R}_{xx}$ for all modes and let the estimator optimally choose the proper weighting of the modes in (3.23).

One concern is how we would know or estimate $\mathbf{R}_{xx}$ and σ^2. Typically σ^2 would correspond to the noise of the measurement instrument, which can be easily estimated from an observed noise floor. The covariance $\mathbf{R}_{xx}$ can be estimated through modal simulation combined with Monte Carlo techniques. For example, for slot excitation, we would generate many random realizations of slot voltages $\mathbf{v}$, according to expected illumination conditions. For each realization and at each reconstruction frequency we can compute

$$\mathbf{x} = \mathbf{M}\mathbf{v}, \tag{3.24}$$

where $\mathbf{M}$ is the linear operator (matrix) linking slot voltages to modal coefficients, which can be constructed from expressions in Chapter 2. We have $\mathbf{R}_{xx} = \mathbf{M}\mathbf{R}_{vv}\mathbf{M}^H$.

Another idea is to take a maximum entropy approach, where we properly normalize $\mathbf{P}$ and choose $\mathbf{R}_{xx} = \sigma_x^2\mathbf{I}$, which treats modes equally. It can be shown that this choice leads to a single SNR parameter that needs to be specified, which can be estimated from instrument noise and average probe power.

Note that reconstructions in this report are limited to the simple pseudoinverse estimator, and we expect to investigate the performance of ML and other optimal estimators in future work.

3.4. Reconstruction Error Quantification

This section introduces definitions and methods that are used to quantify reconstruction performance in this report.

3.4.1. Port Designations

Three different types of ports are referred to when simulating or measuring the response of an enclosure and reconstructing fields:

Injection Ports. Ports with antennas that are used to transmit power into the vessel. These are used in probe injection experiments, which allow the vessel to be excited in a convenient bench-top experiment with relatively low power. For slot-excitation experiments, there are no injection ports.

Probe Ports. Ports having probes used to collect *observed* field samples and construct the vector $\mathbf{p}$.

Test Ports. Ports with probes that are assumed to be the *unobserved* field locations, where field will be reconstructed. Signals from test ports form the vector $\mathbf{y}$. Note that in this work, we do measure or simulate the field at the test ports, allowing the error in the reconstruction to be computed.

In experiments, we are limited to a small set of ports that can be investigated, and the following specific ports were always used in experiments:

Injection Ports: 4E, 12A

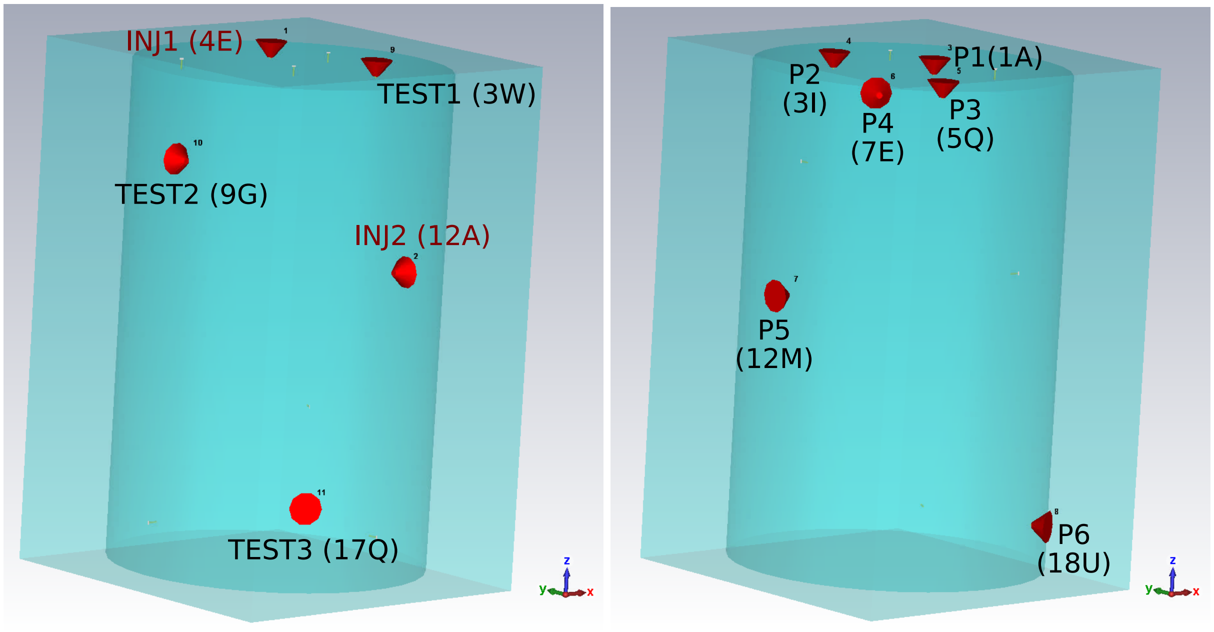

(a) Injection and Test Ports **(b) Heuristic Probe Ports**

Figure 3-1. Specific port locations of PV2 used in experiments and some simulations: (a) injection (INJ) and test (TEST) port locations used in experiments, (b) locations of probes for the *heuristic* probe set.

Test Ports: 3W, 9G, 17Q

These injection and test locations are depicted in Fig. 3-1(a), which were chosen to be spread out and to inject or sample field on both the top and side of the vessel. As described in Chapter 4, in simulation, arbitrary injection and test ports can be considered, which are randomly generated.

The effect of probe placement on reconstruction performance is a major focus of this report. Several probe-placement strategies are considered, one of which is referred to as the *heuristic* probe set, which uses the following port locations:

Heuristic 6 Port: 1A, 3I, 5Q, 7E, 12M, 18U

Heuristic 4 Port: 1A, 5Q, 7E, 18U

It is referred to as “heuristic” because it represents a rule-of-thumb placement strategy that a person might use without detailed information on the cavity modes. In this case, an equal number of probes is placed on the vessel top and side surfaces. On the top surface, probes are widely separated in polar angle and in the radial direction. On the side surface, probes have large separation around the circumference and in the longitudinal direction. Note that probes are also chosen to not be near injection or test locations. The heuristic probe locations are depicted in Fig. 3-1(b).

3.4.2. Error Metrics

Reconstruction error is computed at resonant peaks, which are expected to be the most important frequency points used in shielding effectiveness characterization. Only peaks above a certain threshold are identified and used for error computation, which was done to avoid the high sensitivity of less important weak peaks. The peak threshold in dB is computed as

$$P_{\mathrm{dB,thres}} = \left\langle P_{\mathrm{dB}}(f) - 20\log_{10}(f^2)\right\rangle_f + 20\log_{10}(f^2) + \Delta y_{\mathrm{dB}}, \tag{3.25}$$

where $< \cdot >_f$ indicates an average over frequency, and $\Delta y_{\mathrm{dB}} = 25$ dB was used in this work. The idea of including the $20\log_{10}(f^2)$ term is to create a threshold that tracks the probe efficiency with frequency. Both the transmitted field at an injection probe and the sampled voltage at a receive probe are proportional to f, meaning that a transmission S-parameter in dB will scale as $20\log_{10}(f^2)$ on average. The extra term of Δy_{dB} indicates the offset above the average expected field that a peak must lie above to be detected.

Peaks are identified as points in the test port signal where the derivative of the response with respect to frequency has a zero crossing and power is above $P_{\mathrm{dB,thres}}$. Reconstructions are performed in a neighborhood around each peak, extending from the peak frequency to positive and negative frequency offsets where the response drops by δy_{dB} dB relative to the peak. In this work, $\delta y_{\mathrm{dB}} = 20$ dB was used.

Absolute error at each peak is computed as

$$\epsilon(f_k) = |P_{\mathrm{dB,test}}(f_k) - P_{\mathrm{dB,recon}}(f_k)|, \tag{3.26}$$

where f_k is the frequency sample where a peak is detected, and $P_{\mathrm{dB,test}}(f)$ and $P_{\mathrm{dB,recon}}(f)$ are the measured/simulated test port power and reconstructed test port power, respectively, in dB at frequency f.

Sometimes the reconstruction error for a given peak can be very high due to the dB scale, and these very large errors can dominate the statistics. For this reason, we will define errors above 10 dB as *missed peaks*, and such peaks will be excluded from the computation of statistical distributions and error metrics. However, the probability of missed peaks (P_{missed}) is computed in simulations and experiments, providing an indication of the robustness of the reconstructions.

The set of error at all detected peaks at the test ports is used to generate empirical cumulative distribution functions (CDFs). For visualization purposes, the complementary CDF (CCDF), computed as 1-CDF, is plotted on a log scale, allowing easy identification of $90\%, 99\%, 99.9\%, \ldots$ CDF levels. On a CCDF plot, these are $10\%, 1\%, 0.1\%, \ldots$ levels, indicating the error levels where $90\%, 99\%, 99.9\%, \ldots$ of the cases have lower error. Quantifying error level this way is a another measure of robustness of the reconstruction method. The numerical error level for the 90% CDF level is denoted $\mathrm{Error}_{90\%}$, and this is used to rank the different probe sets in terms of error performance. Average error will be denoted $\mathrm{Error}_{\mathrm{Avg}}$ which is the simple mean of the absolute error of all detected peaks.

3.5. Example Reconstruction: Empty PV2 with Probe Injection

To conclude this chapter, we provide an example of applying reconstruction to simulated data of the empty PV2, which was generated using the modal simulation technique with closed-form modes.

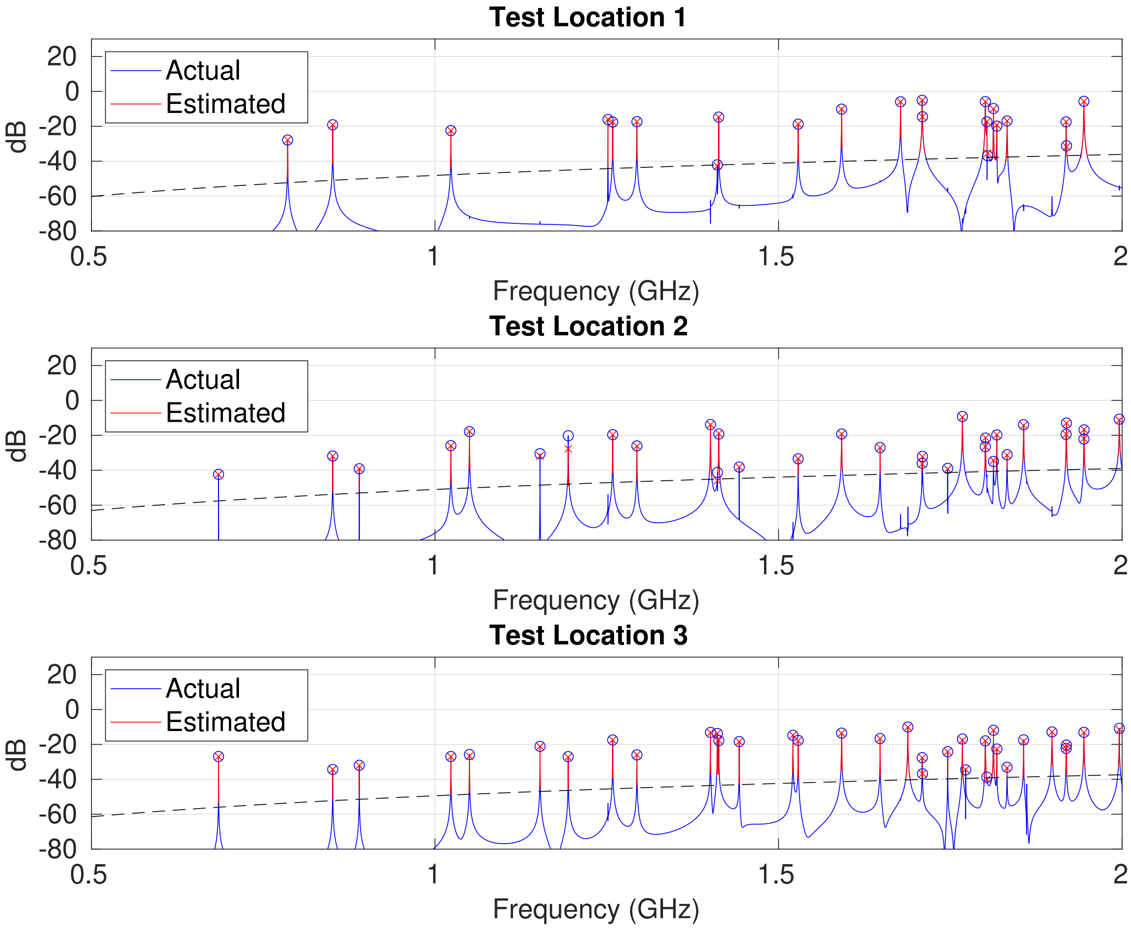

Figure 3-2. Example reconstruction of simulated field at the injection, probe, and test port locations shown in Fig. 3-1. The dashed line is the peak detection threshold.

Here, we use the measurement test and injection ports specified in Section 3.4.1, along with the heuristic probe locations for six ports. A noise level of -80 dB is assumed and probe lengths are 1 cm.

Fig. 3-2 shows the simulated (Actual) field at the test ports, as well as the field reconstructed (Estimated) at test port locations from the six probe measurements. Blue circles are plotted at the detected peaks in the test port signals, and the reconstructed response at the same frequency of each peak is shown with a red x. In this example, very good reconstruction is achieved. Table 3-1 shows the reconstruction metrics for the three test locations, indicating error levels below 1 dB and no missed peaks. Fig. 3-3 illustrates a CCDF of the data, generated from the 85 detected peaks. The 90% error level can be extracted from the plot by reading the error on the x axis when the probability level on the y axis is $10\% = 10^{-1}$.

Test Port	P_{missed}	$\text{Error}_{90\%}$	$\text{Error}_{\text{Avg}}$
1	0.00 %	0.8 dB	0.2 dB
2	0.00 %	0.6 dB	0.6 dB
3	0.00 %	0.8 dB	0.2 dB

Table 3-1. Performance metrics of the example reconstruction case.

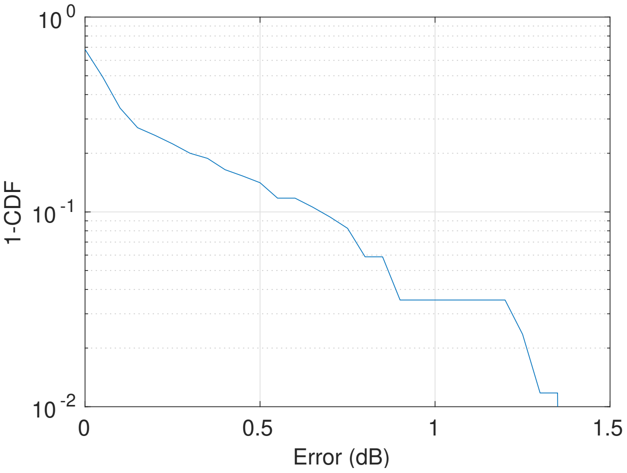

Figure 3-3. CCDF of the reconstruction error for the example reconstruction case.

4. EMPTY VESSEL PROBE INJECTION STUDY

This chapter describes simulations and experiments that were performed to evaluate the performance of the developed field reconstruction methods for the empty PV2. Here we concentrate on convenient probe-injection studies, which can be performed on a lab bench without the need of a chamber or high power EM fields.

The modal simulation technique from Chapter 2 was used with closed-form modes to simulate the vessel response. Efficient modal simulation allows fairly exhaustive simulations of random probe placement to be performed, indicating the statistical behavior of reconstruction error. Simulations of random probe placement not only show the sensitivity of reconstruction error to probe location, but also provide useful probe sets with good and bad performance that can be explored in later experiments.

The chapter concludes with probe injection experiments performed on PV2 for a few different probe placement strategies. Overall, the limited experimental trials confirm the findings seen in the more exhaustive simulation studies.

4.1. Random Probe Set Simulations

Two hundred random probe sets were generated, where each probe set had six probes, and these were used for all random probe studies in this report. The complete listing of these probe sets is provided for reference in Appendix D. The reconstruction performance of each probe set was tested by running one hundred random realizations for each probe set, where a realization has two randomly chosen injection ports, three randomly chosen test ports, and a random injection weight vector. The random port locations are chosen to have uniform probably for all candidate locations on the top and side of PV2. Injection, test, and probe ports are not allowed to coincide with each other. The random weight vector is generated with iid complex Gaussian entries and then normalized to have unit norm.

S-parameters [4] were used to quantify the response of the vessel from injection ports to probe and test ports. This simplifies later VNA experiments, where the S-parameters are directly measured. The reconstruction methods can be applied without modification to S-parameters rather than sampled field, because field is directly proportional to calibrated S-parameters. Random complex Gaussian noise was added to each S-parameter realization to simulate the behavior seen in later measurements. The variance of the noise was chosen to achieve a noise floor of -80 dB, similar to probe injection experiments.

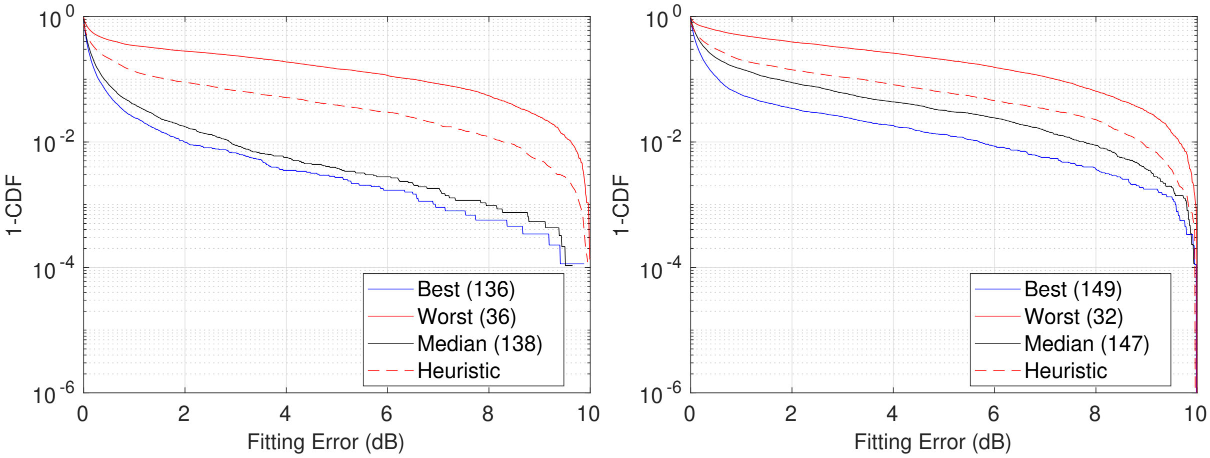

(a) 1-CDF (6 Probes) **(b) 1-CDF (4 Probes)**

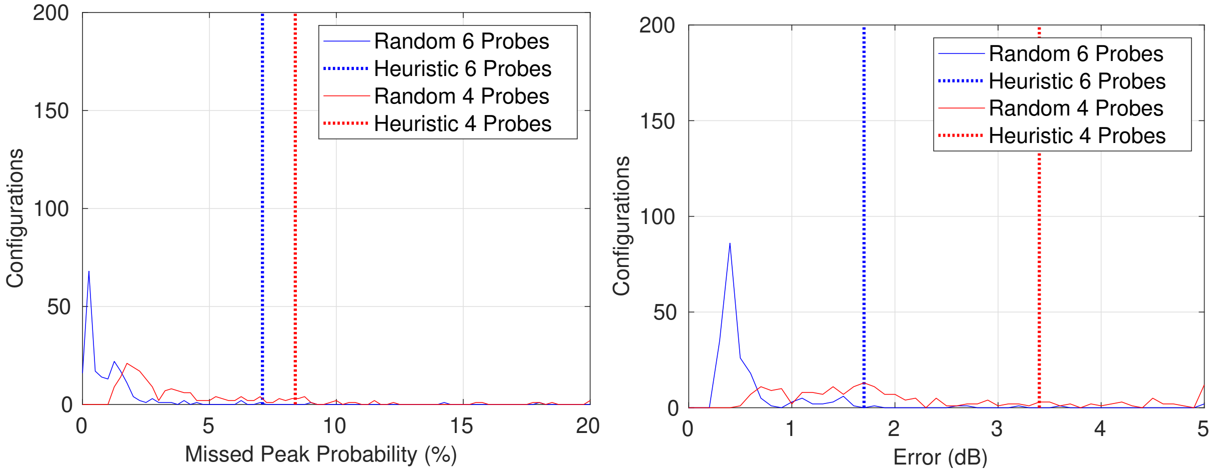

(c) P_{missed} Histogram **(d) $\text{Error}_{90\%}$ Histogram**

Figure 4-1. Reconstruction performance statistics of the random parameter sets for the empty PV2 probe injected case.

4.2. Random Simulation Results

This section documents error performance of field reconstructions when $N'_{\text{mode}} = 4$, meaning the four modes closest to each reconstruction frequency are used for reconstruction. Fig. 4-1(a) and (b) plot CCDFs for reconstruction error with six and four probes, respectively. The performance of three randomly generated probe sets are plotted, namely those having the best, median, and worst $\text{Error}_{90\%}$ performance. The indices of the probe sets are listed in the plot legend, which can be referred to in Appendix D. The statistical performance of the heuristically chosen probe set is also shown for comparison.

When using four probes, performance increases significantly when moving from the worst probe set, to the median probe set, to the best probe set. However, for six probes, the median probe set and best probe set are very close. This illustrates that having more probes relative to the number of mode coefficients to be estimated reduces the importance of selecting the optimal set. It is

	N_P	Index	Probes
Good	6	61	17S, 7H, 18F, 2E, 19M, 4A
	4	73	13P, 9W, 10T, 19M
Bad	6	36	9P, 4B, 5A, 3P, 3L, 5K
	4	36	9P, 4B, 5A, 3P
Heuristic	6	-	1A, 3I, 5Q, 7E, 12M, 18U
	4	-	1A, 5Q, 7E, 18U

Table 4-1. Identified good and bad probe sets from random probe set simulations for four-mode reconstruction in empty PV2 with probe injection. The heuristic probe set is also given for comparison.

	N_P	P_{missed}	$\text{Error}_{90\%}$	$\text{Error}_{\text{Avg}}$
Good	6	0.04%	0.4 dB	0.2 dB
	4	1.63%	0.7 dB	0.3 dB
Bad	6	18.43%	6.2 dB	1.7 dB
	4	17.87%	6.2 dB	1.8 dB
Heuristic	6	7.09%	1.7 dB	0.6 dB
	4	8.38%	3.4 dB	1.0 dB

Table 4-2. Performance of specific probe sets selected from random probe set simulations for four-mode reconstruction in empty PV2 with probe injection.

also interesting to see that the heuristically chosen probe set actually exhibits worse than median performance for both four and six probes.

Fig. 4-1(c) and (d) plot histograms of P_{missed} and $\text{Error}_{90\%}$ with respect to the 200 random probe configurations. With four probes, the histograms for both metrics are fairly spread out with long tails, indicating strong dependence of reconstruction performance on the probe locations. With six probes, the histograms become more concentrated at lower P_{missed} and $\text{Error}_{90\%}$, indicating there are many probe sets with high performance. The heuristic probe set exhibits poor performance for these metrics, lying to the right of the main mass of the random probe set histograms.

Good and bad probe sets were identified from the random probe sets by sorting them with respect to $\text{Error}_{90\%}$. It is also desirable to have a low P_{missed} for a good set, so this was also taken into account. Finally, a probe location should not coincide with a test or injection port to be used in later experiments, which eliminates some probe sets. Table 4-1 lists specific good and bad probe sets for four-mode reconstruction that were identified according to these criteria. The numerical performance of these and the heuristic probe set are given in Table 4-2.

4.3. Measurement

Measurements were performed of the empty PV2 with probe injection using the selected probe sets in Table 4-1. The measurements were performed with a calibrated two-port vector network analyzer (VNA) shown in Fig. 4-2 using the parameters listed in Table 4-3.

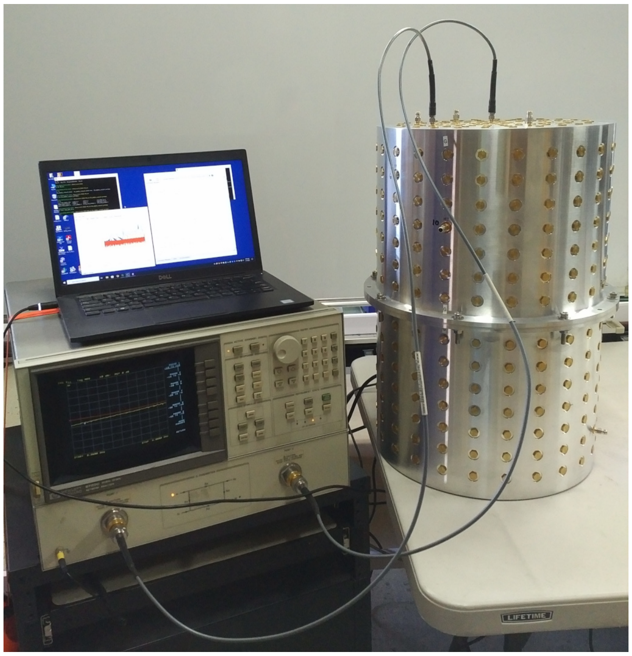

Figure 4-2. VNA measurement setup for empty PV2 with probe injection.

Parameter	Value
Output Power	7 dBm
IF Bandwidth	1 kHz
Frequency Range	560 MHz – 2 GHz
Frequency Step	100 kHz (14401 points)
Calibration	Full 2-port

Table 4-3. VNA parameters for PV2 probe injection measurements.

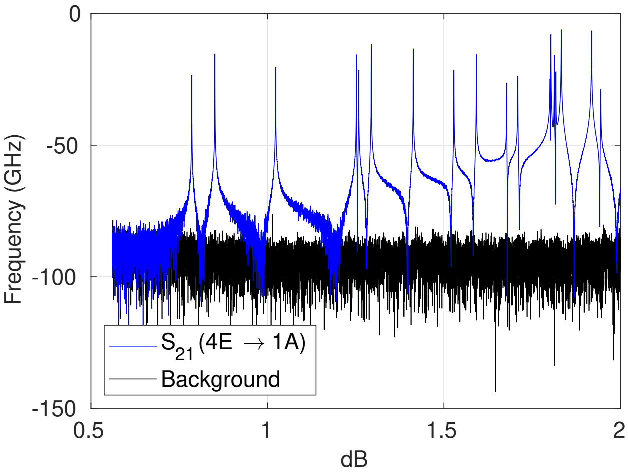

Figure 4-3. Background measurement for empty PV2 probe injection experiments.

Port 1 of the VNA was connected to one of the two injection ports, and Port 2 was connected to one of the nine probe or test ports, requiring 2×9 measurements for each probe set. Note that unconnected PV2 ports were always terminated with 50 Ω loads when not connected to the VNA.

A background measurement of the probe injection experiment is shown in Fig. 4-3. In this measurement, a terminator/short blocking element was placed between the end of the Port 1 VNA cable and the injection port (4E) on PV2. The terminator/short is a coaxial 50 Ω terminator and a coaxial shorting cap that have been soldered together (back to back). This blocks the radio-frequency (RF) signal on the inside of the cable, but still provides a ground connection. The idea is to allow measurement of undesired coupling in a background measurement on or through cable shields, while blocking the desired RF path on the cable interior. Port 2 of the VNA was connected to the first heuristic probe port (1A) as usual. The background response is dominated by the VNA noise floor, which is -80 dB or lower.

The same modal reconstruction technique was applied here to measurements of the good, bad, and heuristic probe sets for both six and four probes. The injection weight vector applied to the two injection ports was $[1\ j]$ in all cases here. Simulations were also performed for the same injection, probe, and test ports used in measurements. Detailed reconstructions are shown in Appendix E Section E.1 for the empty PV2 for the good, bad, and heuristic probe sets for both simulated and measured data with six and four probes.

A summary of the performance metrics for the different cases is shown in Table 4-4. Overall, good agreement is seen in the reconstruction performance seen in measurement and simulation. The main exception is the measured good probe set, which has significantly worse measured performance than simulations. Interestingly, in the measurements for these specific injection and test ports, the heuristic probe set performs as good or better than the good random probe set. This was not true in simulation, where the heuristic probe set performed somewhat worse than the good random probe set. The poor performance of the bad random probe set is seen in both simulation and measurement.

These results illustrate that useful reconstructions can be performed on measured data, where model uncertainty is certainly present. With six probes, reconstruction error at the 90% confidence level

Measured				
	N_P	P_{missed}	$\text{Error}_{90\%}$	$\text{Error}_{\text{Avg}}$
Good	6	0.00 %	1.4 dB	0.6 dB
	4	6.19 %	3.5 dB	1.4 dB
Bad	6	13.00 %	4.7 dB	1.4 dB
	4	14.00 %	4.8 dB	1.7 dB
Heuristic	6	0.00 %	1.1 dB	0.5 dB
	4	0.00 %	3.2 dB	1.1 dB

Simulated				
	N_P	P_{missed}	$\text{Error}_{90\%}$	$\text{Error}_{\text{Avg}}$
Good	6	0.00 %	0.4 dB	0.1 dB
	4	3.37 %	0.5 dB	0.3 dB
Bad	6	10.99 %	4.2 dB	1.4 dB
	4	10.42 %	4.2 dB	1.4 dB
Heuristic	6	0.00 %	0.8 dB	0.3 dB
	4	0.00 %	2.4 dB	0.7 dB

Table 4-4. Performance metrics of measured and simulated reconstructions in the empty PV2 with probe injection.

was only 1.4 dB with the good random probe set, and no missed peaks were observed. With four probes, the error increased to 3.5 dB for this case, but this level of error is also expected to be useful for practical shielding effectiveness characterization.

5. BOX IN VESSEL PROBE INJECTION STUDY

This chapter describes simulations and experiments of a more difficult reconstruction case, where a small steel box with dimensions 122 mm × 122 mm × 87 mm was placed in the bottom of PV2. There were two important reasons for studying this more complex case:

- Adding the box breaks the symmetry of the vessel, requiring numerical modes to be computed with the workflow described in Appendix C. Thus, the box-in-vessel case illustrates that useful reconstructions with low error can be obtained using these numerical methods.
- Additional model uncertainty is present, since the box is placed manually in the bottom of the vessel. Such uncertainty is likely to be present in real measurement scenarios, and it is important to check if the field reconstruction methods are robust to such errors.

The modal simulation technique from Chapter 2 was used with numerical modes found with the workflow in Appendix C. The COMSOL geometry is depicted in Fig. 5-1. COMSOL simulation of this cavity using the default physics-controlled mesh from 500 MHz to 2 GHz found 65 modes. Run time was about 7 minutes on an Intel Xeon Platinum 8176 CPU at 2.10 GHz using 12 cores. Subsequent simulation of 11×11 S-parameters using modal simulation required only 0.7 seconds in MATLAB on a single core for the full frequency range.

5.1. Random Probe Set Simulations

The same two hundred probe sets that were described in Section 4.1 and listed in Appendix D were analyzed for the box-in-PV2 simulations. As before, one hundred random realizations were generated for each probe set, with each realization having two random injection ports, three random test ports, and a random injection weight vector. For a given set of ports, 11×11 S-parameters were computed for the box-in-PV2 geometry using the modal simulation method with numerical modes. Complex Gaussian noise was added to a achieve a noise floor of -80 dB.

5.2. Random Simulation Results

This section documents error performance of field reconstructions when $N'_{\text{mode}} = 4$, meaning the four modes closest to each reconstruction frequency are used for reconstruction. Fig. 5-2(a) and (b) plot CCDFs for reconstruction error with six and four probes, respectively. The CCDFs for three randomly generated probe sets are plotted, namely those having the best, median, and worst $\text{Error}_{90\%}$ performance. The indices of the probe sets are listed in the plot legend, which can be referred to in Appendix D.

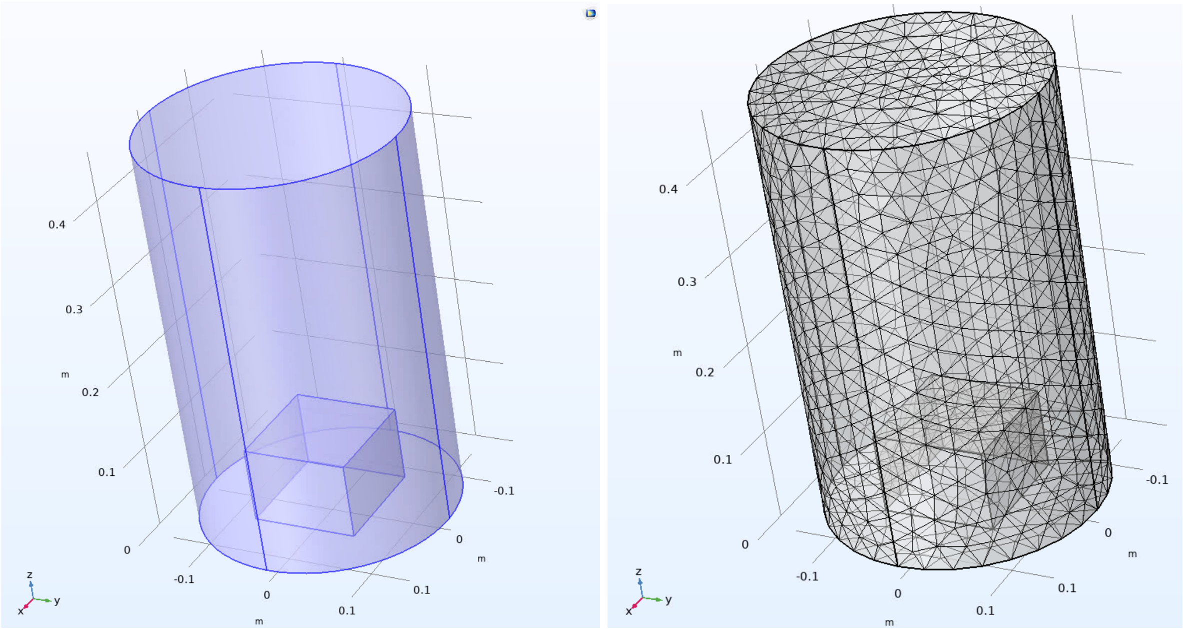

(a) Cavity Model **(b) Meshed Model**

Figure 5-1. Box-in-PV2 model used to find numerical modes with COMSOL.

The statistical performance of the heuristically chosen probe set is also shown for comparison.

For both four and six probes, performance increases significantly when moving from the worst probe set, to the median probe set, to the best probe set. Note that this is different from the empty vessel case, where with six probes, the 1-CDF plot of the median and best cases looked nearly identical for the median and best cases. This suggests that having a more complex vessel shape (lack of symmetry) increases the importance of judiciously choosing probe locations.

Fig. 5-2(c) and (d) plot histograms of P_{missed} and $\text{Error}_{90\%}$ with respect to the 200 random probe configurations. For four probes, the results are similar to the case of the empty vessel, where these metrics are spread out for four probes, but much more concentrated for six probes. This emphasizes the importance of selecting good probe locations with sparse probes.

Good and bad probe sets were identified from the box-in-PV2 random probe set simulations, which are given in Table 5-1. The numerical performance of these and the heuristic probe set are given in Table 5-2. We note that the the bad probe set had significantly worse performance for the box-in-PV2 case as compared to the empty vessel (see Table 4-2). Interestingly, the heuristic probe set with four probes also had somewhat decreased performance compared to the previous empty case.

5.3. Measurement

Measurements were performed of the box-in-PV2 with probe injection using the selected probe sets in Table 5-1, except for the bad probe set, which was not investigated for this vessel configu-

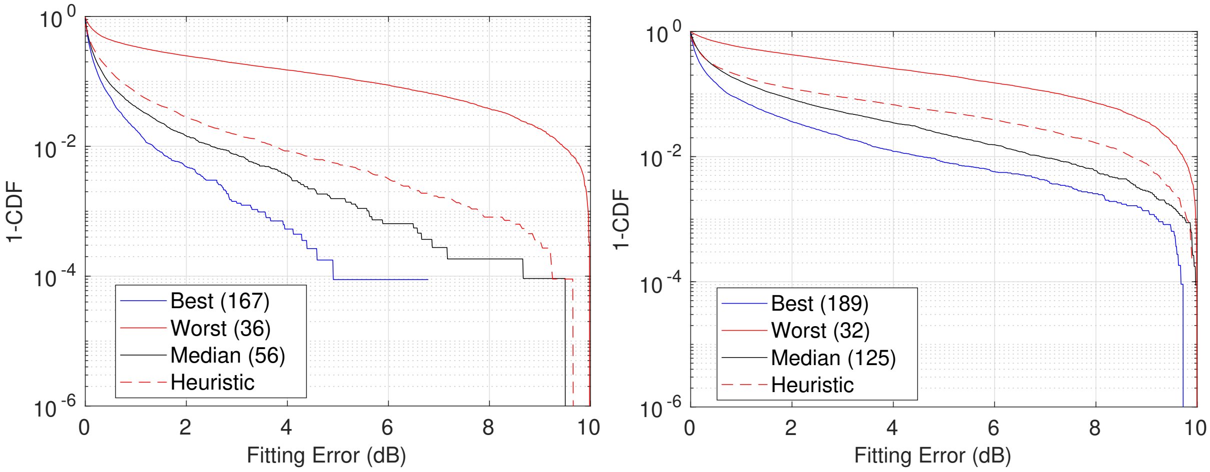

(a) 1-CDF (6 Probes) **(b) 1-CDF (4 Probes)**

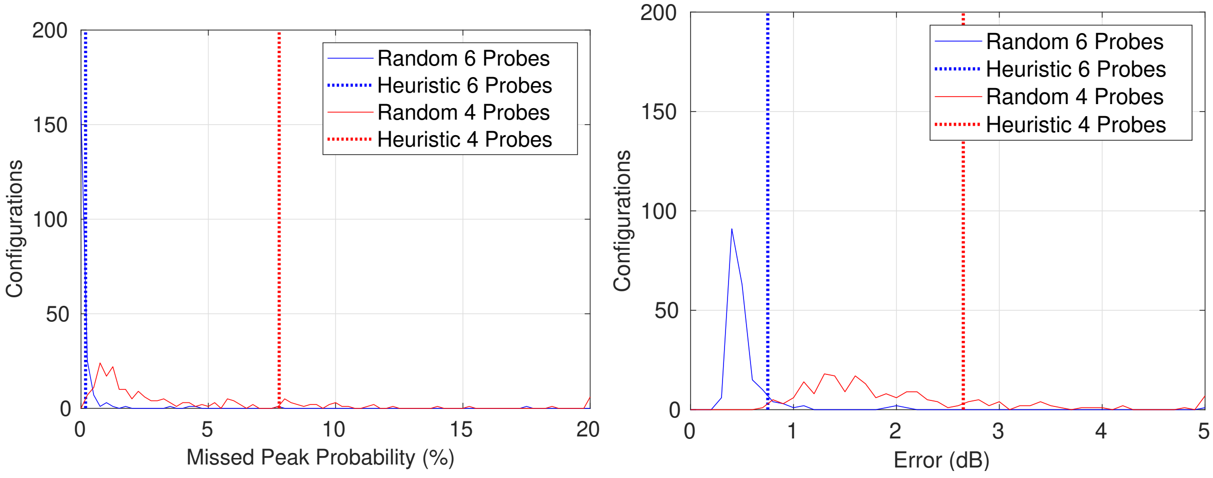

(c) P_{missed} Histogram **(d) $\text{Error}_{90\%}$ Histogram**

Figure 5-2. Reconstruction performance statistics of the random parameter sets for the box in PV2 probe injected case.

	N_P	Index	Probes
Good	6	116	8P, 5O, 18B, 3K, 14W, 16I
	4	136	13G, 7X, 13N, 16I
Bad	6	36	9P, 4B, 5A, 3P, 3L, 5K
	4	36	9P, 4B, 5A, 3P
Heuristic	6	-	1A, 3I, 5Q, 7E, 12M, 18U
	4	-	1A, 5Q, 7E, 18U

Table 5-1. Identified good and bad probe sets from random probe set simulations for four-mode reconstruction in box-in-PV2 with probe injection. The heuristic probe set is also given for comparison.

	N_P	P_{missed}	$\text{Error}_{90\%}$	$\text{Error}_{\text{Avg}}$
Good	6	0.03%	0.4 dB	0.2 dB
	4	0.41%	0.9 dB	0.4 dB
Bad	6	17.87%	5.3 dB	1.5 dB
	4	35.08%	6.5 dB	2.0 dB
Heuristic	6	0.18%	0.8 dB	0.3 dB
	4	7.78%	2.7 dB	0.9 dB

Table 5-2. Performance of specific probe sets selected from random probe set simulations for four-mode reconstruction in box-in-PV2 with probe injection.

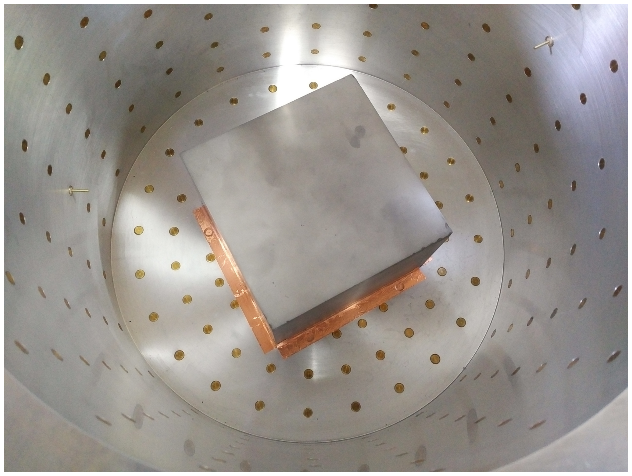

Figure 5-3. Steel box placed in the vessel for box-in-PV2 measurements. The box was taped to the bottom of PV2 using copper tape.

ration. The same VNA setup, parameters, and procedure were used for measurements as was done previously with the empty vessel (see Section 4.3).

The placement of the metal box in the bottom of PV2 is depicted in Fig. 5-3. The welded steel box has no seams or apertures, except for a probe hole in the bottom center. This probe hole was used to align the box with the bottom center of PV2 using an SMA bulkhead connector. The box was manually rotated to be approximately aligned in the xy plane as shown in Fig. 5-1. The rotation was approximate, because it had to be moved and aligned by hand. Copper tape was used to affix the box to the bottom of PV2 at four edges, which kept the box from moving during setup and measurements.

The numerical modal reconstruction technique was applied to measurements of the good and heuristic probe sets for both six and four probes. The injection weight vector applied to the two injection ports was $[1\ j]$ in all cases here. Simulations were also performed for the same injection, probe, and test ports used in measurements. Detailed reconstructions are shown in Appendix E Section E.2 for the box-in-PV2 for the good and heuristic probe sets for both simulated and measured data with six and four probes.

A summary of the performance metrics for the different cases is shown in Table 5-3. The per-

Measured				
	N_P	P_{missed}	$\text{Error}_{90\%}$	$\text{Error}_{\text{Avg}}$
Good	6	0.00 %	1.7 dB	0.8 dB
Good	4	4.30 %	3.2 dB	1.4 dB
Heuristic	6	0.00 %	2.7 dB	1.2 dB
Heuristic	4	8.25 %	4.2 dB	1.5 dB

Simulated				
	N_P	P_{missed}	$\text{Error}_{90\%}$	$\text{Error}_{\text{Avg}}$
Good	6	0.00 %	0.4 dB	0.1 dB
Good	4	0.00 %	0.8 dB	0.3 dB
Bad	6	12.50 %	5.0 dB	1.3 dB
Bad	4	28.30 %	5.5 dB	1.6 dB
Heuristic	6	0.00 %	0.8 dB	0.3 dB
Heuristic	4	4.67 %	2.4 dB	0.8 dB

Table 5-3. Performance metrics of measured and simulated reconstructions for box-in-PV2 with probe injection.

formance ranking of the different probe set cases is the same in measurements and simulations. However, measurement results exhibit higher absolute P_{missed} and error metrics as compared to simulations, which is expected due to larger model uncertainty when placing the box in PV2. It is worth noting that the measured performance of the good probe set is better than the heuristic probe set, which was not true for the empty vessel.

These results illustrate that useful reconstructions can be performed on measured data of a sparsely populated vessel using the reconstruction framework and numerical modes. With six probes, reconstruction error at the 90% confidence level was only 1.7 dB with the good random probe set, and no missed peaks were observed. With four probes, the error increased to 3.2 dB for this case, which again is expected to be useful for practical shielding effectiveness characterization.

This page intentionally left blank.

6. BOX IN VESSEL SLOT EXCITATION STUDY

This chapter applies the modal reconstruction technique to a more practical shielding scenario, where the box-in-PV2 configuration is excited from thin slots on the vessel perimeter. The same numerical modes computed in Chapter 5 can be used for reconstruction and simulation of cavity fields. However, to generate synthetic responses due to EM coupling through slots, the framework in Section 2.3 was used. As was done in previous chapters, reconstruction performance for the random probe sets in Appendix D are first studied to gauge the importance of probe placement and to identify good and bad probe sets for later experiments. Experiments are then performed on the box-in-PV2 in a small anechoic chamber, where the vessel is illuminated with an antenna outside the vessel. The results demonstrate that useful reconstruction accuracy can be attained for this more practical case.

6.1. Random Probe Set Simulations

The same two hundred probe sets that were described in Section 4.1 and listed in Appendix D were analyzed for the box-in-PV2 simulations with slot excitation. As before, one hundred random realizations were generated for each probe set, with each realization having three random test ports. For the case of slot excitation, injection ports are no longer used. Instead, random excitation is assumed on the thin slots around the perimeter of the vessel.

Slots are formed in PV2 by placing shims on the flange at bolt locations. We chose to place four shims, separated by 90° around the flange. The shims are 5-mil (127 μm) thick and made from brass, thus forming a 5-mil slot when placed on the flange. Each shim occupies 16° of angular extent around the vessel circumference. Fig. 6-1 shows a picture of the shim placement that was used in subsequent experiments, which was also modeled in simulations.

A specific distribution of electric field needs to be assumed in the slots when using the framework in Section 2.3 for slot excited modes. In this work, a thin 5-mil slot was assumed around the entire circumference of PV2, which was divided into patches of 2° angular extent. The voltage in a single slot was assumed to follow a half-sine shape:

$$v_i(\phi) = v_i \sin\left(\frac{\pi\phi}{\Delta\phi}\right), \quad 0 \le \phi \le \Delta\phi, \tag{6.1}$$

where $v_i(\phi)$ is the voltage in the ith slot at local angle ϕ, v_i is the complex voltage at the center of the slot, and $\Delta\phi$ is the angular extent of the slot. The slot voltage v_i was assumed to follow an iid complex Gaussian distribution for all four slots. The sampled voltages around the circumference of the vessel are denoted $v_k = v(\phi_k)$, where $k = 1, \ldots, 180$ is the sub-slot index, and ϕ_k represents the angle at the center of a sub-slot. This vector of voltages was always normalized to have unit norm

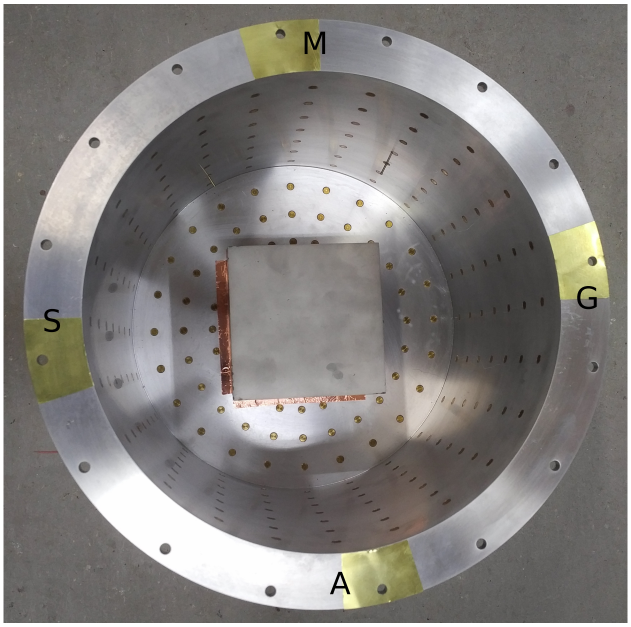

Figure 6-1. Shims placed in PV2.

in simulations. Fig. 6-2 shows an example realization of the amplitude of the slot voltage vector **v**. Note that at shim locations the voltage is assumed to be zero. For each slot voltage realization, the simple model of assuming the same voltage across the entire frequency band was used.

6.2. Random Simulation Results

This section documents error performance of field reconstructions when $N'_{\text{mode}} = 4$, meaning the four modes closest to each reconstruction frequency are used for reconstruction. Fig. 6-3(a) and (b) plot CCDFs for reconstruction error with six and four probes, respectively. The performance of

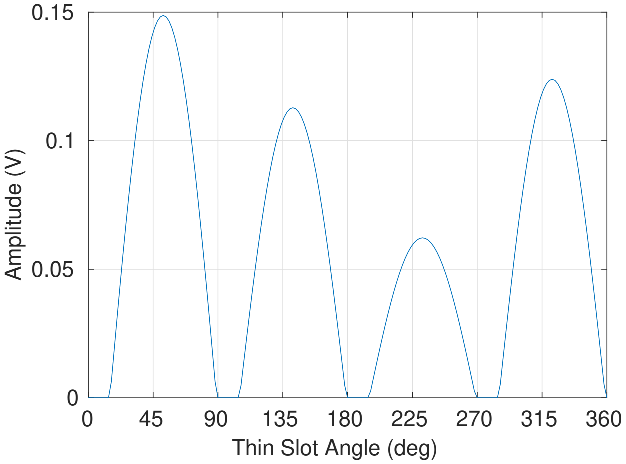

Figure 6-2. Example realization of the random slot voltages.

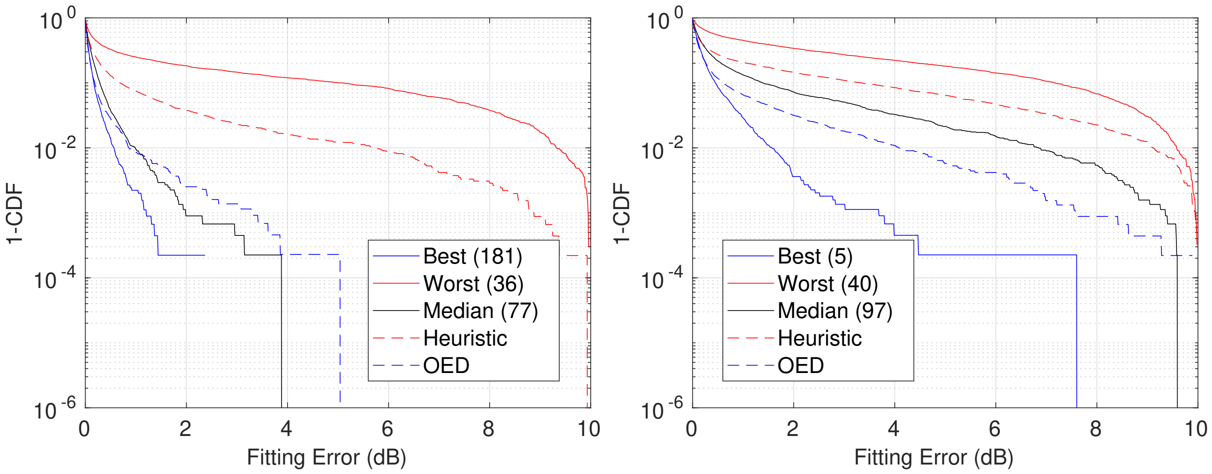

(a) 1-CDF (6 Probes) **(b) 1-CDF (4 Probes)**

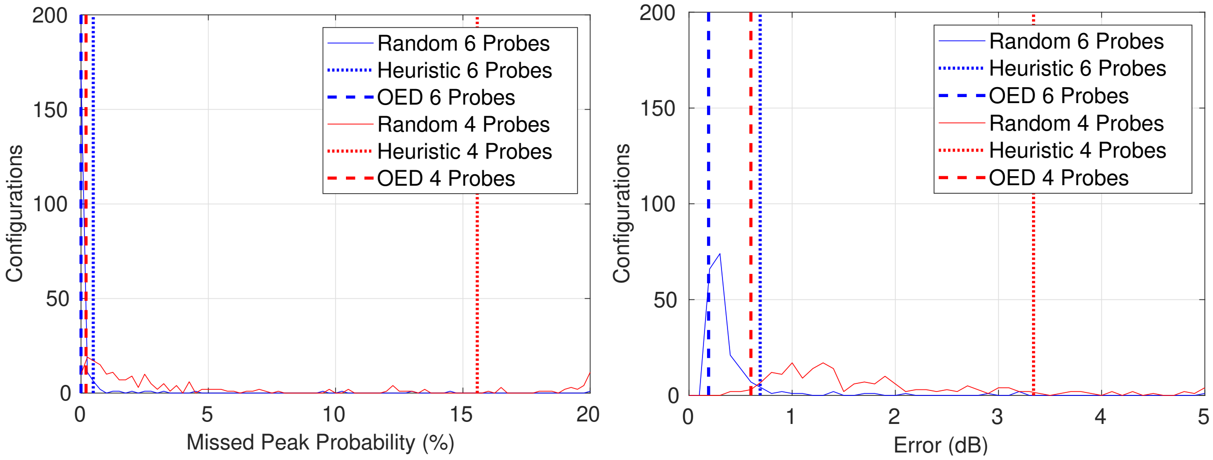

(c) P_{missed} **Histogram** **(d)** $\text{Error}_{90\%}$ **Histogram**

Figure 6-3. Reconstruction performance statistics of the random parameter sets for the box-in-PV2 slot-excited case.

three randomly generated probe sets are plotted, namely those having the best, median, and worst $\text{Error}_{90\%}$ performance. The indices of the probe sets are listed in the plot legend, which can be referred to in Appendix D.

The performance of two other probe sets is plotted along with randomly generated probe set results. First, the performance of the heuristic probe set is shown, which has been described previously. Second, a code for fast selection of near-optimal probe locations has been developed in this LDRD, referred to the Optimal Experiment Design (OED) code. This code implements a greedy algorithm that uses the numerical modes to sequentially build a probe set with good performance. The probes comprising the heuristic and OED probe sets are given in Table 6-1.

For four probes, a wider performance gap is seen between the three random probe sets (best, median, worst) for this study as compared to the two previous probe-injection studies. This emphasizes again the importance of judiciously choosing probe locations when the number of probes is relatively small. For six probes, the median and best random probe sets have similar performance. The

	N_P	Index	Probes
Good	6	14	11P, 16I, 4C, 8R, 4V, 7P
	4	136	13G, 7X, 13N, 16I
Bad	6	36	9P, 4B, 5A, 3P, 3L, 5K
	4	36	9P, 4B, 5A, 3P
Heuristic	6	-	1A, 3I, 5Q, 7E, 12M, 18U
	4	-	1A, 5Q, 7E, 18U
OED	6	-	8H, 17V, 3B, 15E, 17F, 3U
	4	-	8H, 17V, 3B, 15E

Table 6-1. Identified good and bad probe sets from random probe set simulations for four-mode reconstruction in box-in-PV2 with slot excitation. The heuristic and OED probe sets are also given for comparison.

	N_P	P_{missed}	$\text{Error}_{90\%}$	$\text{Error}_{\text{Avg}}$
Good	6	0.00%	0.2 dB	0.1 dB
Good	4	0.02%	0.7 dB	0.3 dB
Bad	6	25.93%	4.9 dB	1.2 dB
Bad	4	40.51%	5.1 dB	1.5 dB
Heuristic	6	0.48%	0.7 dB	0.3 dB
Heuristic	4	15.56%	3.3 dB	0.9 dB
OED	6	0.00%	0.2 dB	0.1 dB
OED	4	0.20%	0.6 dB	0.3 dB

Table 6-2. Performance of specific probe sets selected from random probe set simulations for four-mode reconstruction in box-in-PV2 with slot excitation.

OED probe set consistently outperforms the heuristic and median random probe sets for both six and four probes. It is interesting that the OED probe set has almost the same performance as the best random probe set near the left side of the distribution (near the 90% confidence level), but the low-probability tail on the right side of the distribution more closely follows the median random probe set. Note that the performance of the heuristic probe set is poor for both six and four probes.

Fig. 6-3(c) and (d) plot histograms of P_{missed} and $\text{Error}_{90\%}$ with respect to the 200 random probe configurations. As in the probe injection studies, the heuristic probe set has rather poor performance in terms of missed peak probability and 90% error level. On the other hand, the OED probe set has nearly optimal performance for both six and four probes.

Good and bad probe sets were identified from the box-in-PV2 slot-excited random probe set simulations, which are given in Table 6-1. The heuristic and OED probe sets are also shown for comparison. The numerical performance of these probe set are given in Table 6-2.

Comparing the numerical performance of the different probe sets, it can be seen that the good probe set has very low error and a vanishing probability of missed peaks for both six and four probes. The heuristic probe set has significantly reduced performance compared to the good probe sets,

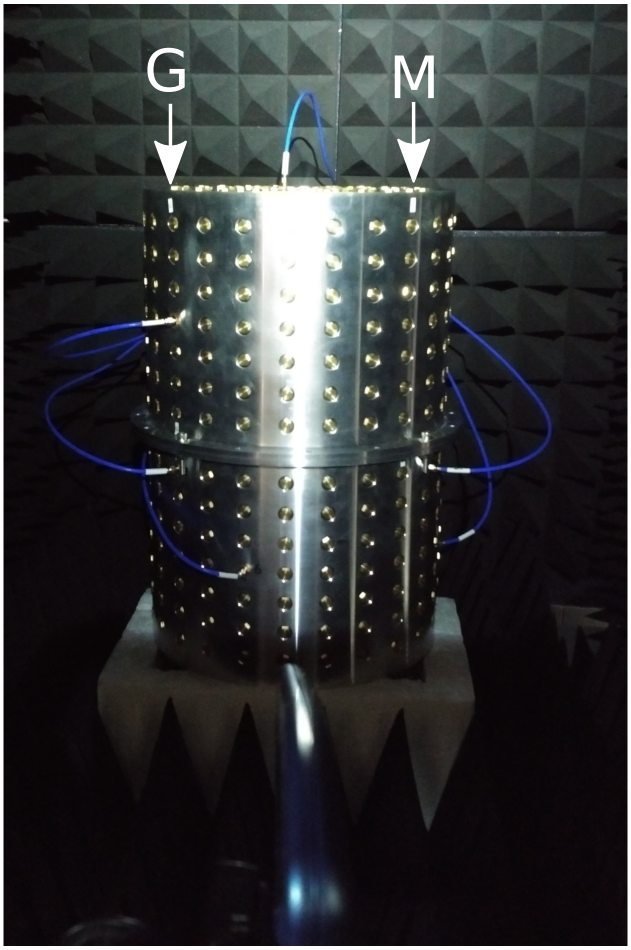

Figure 6-4. PV2 in the small anechoic chamber for box-in-PV2 slot-excitation experiments. The log-periodic transmit antenna is pointed at the center of the slot between columns G and M on PV2.

especially for four probes. Finally the OED probe set has nearly identical performance to the good random probe set for both four and six probes.

6.3. Measurement

Measurements were performed of the box-in-PV2 with slot excitation by placing PV2 in a small anechoic chamber with dimensions 4 ft × 4 ft × 6 ft (1.22 m × 1.22 m × 1.83 m), depicted in Fig. 6-4. Key measurement parameters are given in Table 6-3. Four slots were realized by placing 5-mil shims in the flange as depicted in Fig. 6-1. A log-periodic antenna (Aaronia HyperLog 7040) was used to illuminate PV2 at a range of 55 cm from the tip of the antenna to the PV2 flange. Although this separation is too close for farfield conditions, our goal is to excite fields in the slots, not necessarily to generate a pure plane wave. An amplifier was used to boost the output power at the antenna to 20 dBm. SMA cables were connected to all probe and test ports and fed to the outside of the chamber. These cables were clamped tightly to the back wall of the chamber to keep the cables from moving when manually changing connections during a measurement sequence.

Parameter	Value
Transmit Power	20 dBm
Antenna	Log Periodic (4 dBi gain)
IF Bandwidth	1 kHz
Frequency Range	560 MHz – 2 GHz
Frequency Step	100 kHz (14401 points)
Calibration	Response (thru)

Table 6-3. Parameters for box-in-PV2 chamber measurements.

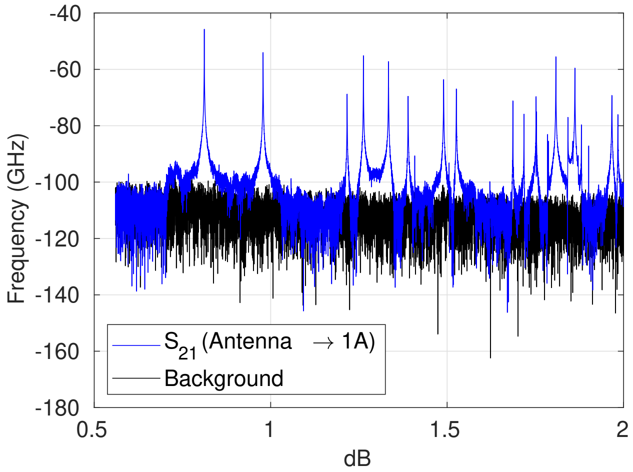

Figure 6-5. Background measurement for box-in-PV2 slot-excitation chamber experiments.

Note that unconnected probe cables were always terminated using 50 Ω loads.

Due to the inclusion of the amplifier on transmit, a full two-port calibration was not performed. Instead, a "response" type calibration was performed to remove bulk cable losses and phase shifts for the nine measured ports (six probe and three test ports). This was accomplished by disconnecting the transmit antenna cable (VNA Port 1) and connecting it to each of the nine PV2 port cables in turn. On the receive side, the cable from VNA Port 2 was connected directly to the other side of each cable. The S_{21} response for each port was measured and then used to correct subsequent PV2 slot-excitation measurements.

A background measurement of the slot-excitation chamber measurement is shown in Fig. 6-5. In this measurement, VNA Port 1 was connected to the transmit antenna as usual, but a terminator/short blocking element was placed between the first probe port SMA output (Port 1A) on PV2 and the cable leading to the VNA. The background response is dominated by the VNA noise floor, which is approximately -100 dB or lower.

The same modal reconstruction technique was applied here to measurements of the good and heuristic probe sets for both six and four probes. Only the single angle of incidence (antenna aimed at the slot between columns G and M) was tested. Simulations were also performed for the same cases that were measured, where the slot voltage was assumed to be a half sine on the single slot (between columns G and M) and zero on the other slots. Detailed reconstructions are

Measured				
	N_P	P_{missed}	$\text{Error}_{90\%}$	$\text{Error}_{\text{Avg}}$
Good	6	0.00 %	1.8 dB	0.7 dB
Good	4	0.00 %	2.7 dB	1.3 dB
Heuristic	6	3.80 %	2.5 dB	1.0 dB
Heuristic	4	17.72 %	4.8 dB	1.4 dB
Simulated				
	N_P	P_{missed}	$\text{Error}_{90\%}$	$\text{Error}_{\text{Avg}}$
Good	6	0.00 %	0.2 dB	0.1 dB
Good	4	0.00 %	0.7 dB	0.3 dB
Bad	6	29.17 %	2.4 dB	1.0 dB
Bad	4	41.67 %	5.8 dB	2.0 dB
Heuristic	6	2.08 %	0.2 dB	0.1 dB
Heuristic	4	10.42 %	4.1 dB	0.9 dB
OED	6	0.00 %	0.2 dB	0.1 dB
OED	4	0.00 %	0.4 dB	0.2 dB

Table 6-4. Performance metrics of measured and simulated reconstructions for box-in-PV2 with slot excitation.

shown in Appendix E Section E.3 for the box-in-PV2 chamber measurements. A summary of the performance metrics for the different cases is shown in Table 6-4.

In terms of relative performance, simulations track measurement results fairly well. The heuristic probe set has significantly lower performance as compared to the good probe set for missed peaks and 90% error. Average error, however, is similar for the two probe sets. The simulated OED probe set had zero missed peak probability, as well as the lowest simulated error metrics. The simulated bad probe set shows the high penalty that could be caused by choosing a poor probe configuration.

These results illustrate that useful reconstructions can be performed on practical measured data, having uncertainty in the placement of internal components (the box) as well as imprecise knowledge of angle of incidence and slot excitations. With six probes, reconstruction error at the 90% confidence level was only 1.8 dB with the good random probe set, and no missed peaks were observed. With four probes, reconstruction error at the 90% confidence level was only 2.7 dB and still no missed peaks were observed. As with previous probe injection experiments, we expect this level of error to be low enough for practical shielding effectiveness studies.

This page intentionally left blank.

7. SUMMARY AND CONCLUSION

This report has documented theory, simulations, and experiments from the Optimal Experiment Design LDRD for reconstructing cavity fields from sparse probe measurements. This work directly supports shielding effectiveness characterization, enabling spatial fields throughout an enclosure to be predicted from judiciously placed probes. The methods are appropriate for the fundamental and undermoded regimes, where modal fields are sufficiently sparse. A key aim of the work was to understand the importance of probe placement in minimizing reconstruction error.

Key tools developed in this effort included workflows for modal simulation of cavity fields. Traditional simulation of enclosures in the fundamental and undermoded regimes requires full-wave simulation with either a very fine frequency step or an adaptive sweep in order to resolve resonant peaks. Even with an adaptive frequency sweep, full-wave simulations can be time consuming and must be performed for all point-of-entry (POE) configurations of interest. On the other hand, the modal simulation methods only require a single eigenfrequency simulation to be performed, after which the response for fairly arbitrary POEs can be computed in a few seconds for a full frequency sweep. This allowed extensive statistical studies of probe placement to be performed in this report, where many thousands of POE configurations were simulated. We expect that these methods will also be extremely useful in the future for efficient calibration of models to measured data.

Our investigations focused on a cylindrical cavity based on Vessel 2 [5], which was referred to as the Perforated Vessel 2 (PV2). The top, bottom, and sides of PV2 are covered with numerous holes for probes, allowing in-depth studies of the effect of probe placement on reconstruction performance. We began with probe-injection simulations and experiments that could be performed conveniently on a laboratory bench at relatively low EM power levels. Later, we performed slot-excitation experiments in a small anechoic chamber. Overall, the behaviors seen in the more difficult chamber-based measurements were already observed in the simpler probe-injection studies, demonstrating that probe injection is a useful modality for testing EM cavity models and associated reconstruction performance.

Simulations were performed on 200 probe sets that were randomly generated assuming a uniform distribution over the available probe holes on the top and sides of PV2. The goal was to understand how strongly reconstruction performance depends on probe placement, as well as to identify good and bad probe sets that could be used in later experiments. The simulations illustrated that when the number of probes is equal to the number of modal coefficients estimated at each reconstruction frequency, judicious probe placement is critical for obtaining good reconstruction performance. On the other hand, when the number of probes is significantly larger than the number of modes being estimated, most of the randomly chosen probe sets had good performance.

A surprising simulation result was the relatively poor performance of a "heuristic" probe set that was chosen using the intuition that probes should be spread out as much as possible on the top and side surfaces of PV2. The results showed that this choice of probe placement usually had worse performance than the median randomly selected probe set. This shows that probe placement algorithms and simulation studies may be critical for ensuring useful probe data is extracted from experiments. It also illustrates the need for fast algorithms and new rule-of-thumb strategies to place probes for good performance.

In addition to studies with the empty PV2 cavity, simulations and experiments were also performed for the case of including simple contents in the enclosure. Specifically, a rectangular steel box was placed in the bottom of PV2. The presence of this box breaks the symmetry of the structure, requiring modes to be found numerically. The box also presents significant modeling uncertainty in experiments, since the box was placed by hand in position and taped to the bottom of PV2 with copper tape.

Experiments were performed on a limited number of cases to verify behaviors observed in simulation. Experiments explored good, bad, and heuristic probe sets for the empty PV2 and box-in-PV2 cases, as well as both probe injection and slot excitation. Overall, the relative performance of the various probe sets seen in simulations was confirmed by experiments. However, the absolute error of reconstructions was higher in experiments, as compared to simulation, but error still remained within useful levels. Numerically, the error of reconstructed resonant peaks for a judiciously chosen probe set was no larger than 3.5 dB and 1.8 dB at the 90% confidence level for four and six probes, respectively, with nearly zero probability of a missed peak detection.

One limitation of this work was the simplicity of the modal reconstruction method, where a direct pseudoinverse was used for a fixed number of modes per reconstruction frequency. An advantage of this approach is that the estimator does not require information on noise levels, the distribution of modal coefficients, nor the degree of modal coupling to the reconstruction frequency. A significant disadvantage, however, is that the pseudoinverse can exhibit noise amplification, leading to suboptimal performance. Also, not estimating the optimal number of modes and including modes with insignificant coupling to a reconstruction frequency can lead to poor conditioning and higher error of the inverse. In future work, we expect to explore theoretically optimal approaches, such as the minimum-mean-squared-error (MMSE) estimator, the maximum likelihood (ML) estimator, etc.

In conclusion, we point out the success of this effort in demonstrating useful reconstruction of cavity fields of an empty cavity, as well as one having simple contents. The results are encouraging and suggest that modal reconstruction may have high practical value in estimating shielding throughout an enclosure without the need to include a large number of probes. We have also demonstrated that detailed simulations can predict the same behavior observed in measurements, suggesting that probe placement can be explored before experimental campaigns to determine good probe placement strategies and expected reconstruction error. Although the investigations in this report considered fairly simple cavity geometries, the methods developed are general and should be applicable to arbitrary cavity shapes. Future investigations are needed to assess how well these methods perform for more realistic cavity shapes that may have significantly higher complexity and associated model uncertainty.

APPENDIX A. Perforated Vessel 2 (PV2)

This appendix provides details on the design of the perforated Vessel 2 (PV2) used in simulations and experiments in this report. The design is very similar to the original Vessel 2 that is described in [5]. PV2 consists of two top-hat like aluminum structures that are bolted together at a flange, as depicted in Figure A-1. The wall thickness of PV2 is 0.5 inches, which was increased from the 0.25-inch thickness of the original Vessel 2 to accommodate probes on the walls. Slots are formed by placing shims on the flange at bolt positions. In probe injection experiments, bolts were used at eight out of the sixteen bolt holes, and no shims were used. Bolts were always torqued to 20 in-lbs in this report. For slot excitation experiments, only four bolt holes were used, and 5-mil brass shims were placed at the bolt positions as depicted in Fig. 6-1.

Like Vessel 2, PV2 has a flange that is 0.25 inches thick and extends 0.75 inches from the vessel surface to the outer flange edge, giving the slots a depth of 1.25 inches. The interior of the vessel is a cylindrical cavity with height and radius equal to 18 and 5.75 inches, respectively.

A detailed drawing of PV2 is shown in Figure A-3. Note that the eight tapped 10-32 holes on the top face and bottom face can be used for vibration experiments or for placing PV2 on a rotation stage for scanned measurements, as was done in [5].

Due to the many holes in PV2, a suitable way to cover the unused holes is needed. For this purpose, a custom built SMA plug part was designed and manufactured. The plug was designed with the 0.25-36 UNS 2A thread compatible with SMA connectors. The length of the bolt shaft is 0.45 inch, which given the thickness of the vessel walls (0.5 inch) minus the inset for the probe heads (0.05 inch), provides a nearly flush surface on the inside wall at each plug location. The SMA plugs were fabricated in brass, which was deemed soft enough to not damage the threads of the aluminum vessel. A photo and mechanical drawing of the SMA plug are given in Fig. A-4 and A-5, respectively. Not only does the SMA plug avoid the use of copper tape or other means of covering unused holes, the plugs may be removed or replaced without the need to disassemble the vessel.

The probes that were used with PV2 are monopoles that were realized by placing a 1-cm pin inside a bulkhead SMA adapter. To save cost, standard dielectric-filled SMA bulkhead adapters were used (Amphenol Part# 132170), where the outer conductor on the long side was cut off right at the end of the dielectric material and inner pin socket. Using this cut SMA adapter with a standard 40-mil copper crush washer provided almost the exact depth needed for the dielectric and inner pin socket to be flush with the inside of PV2. A photo of the modified SMA adapter used in experiments is shown in Fig. A-6.

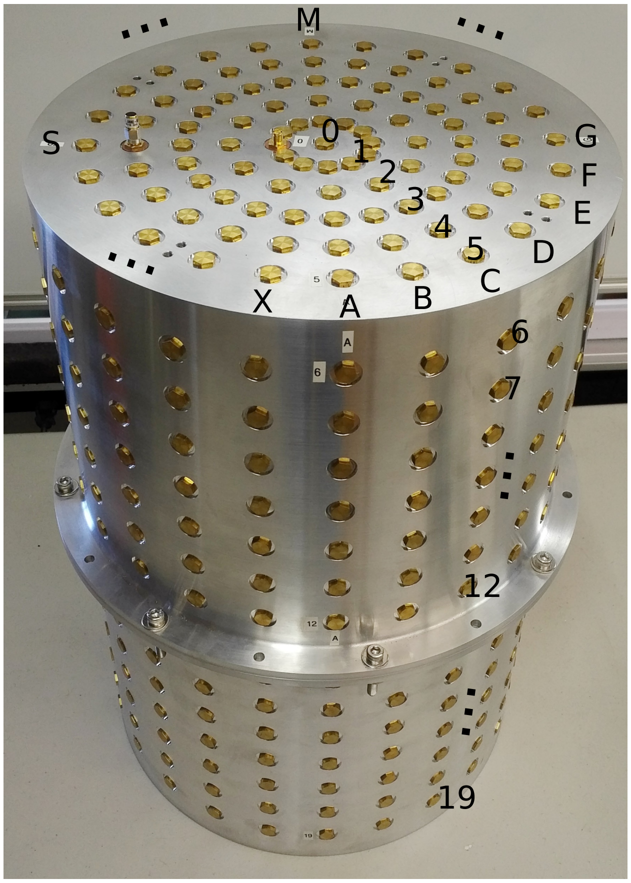

Figure A-1. Photo of PV2 with row (0-19) and column (A-X) labels for ports.

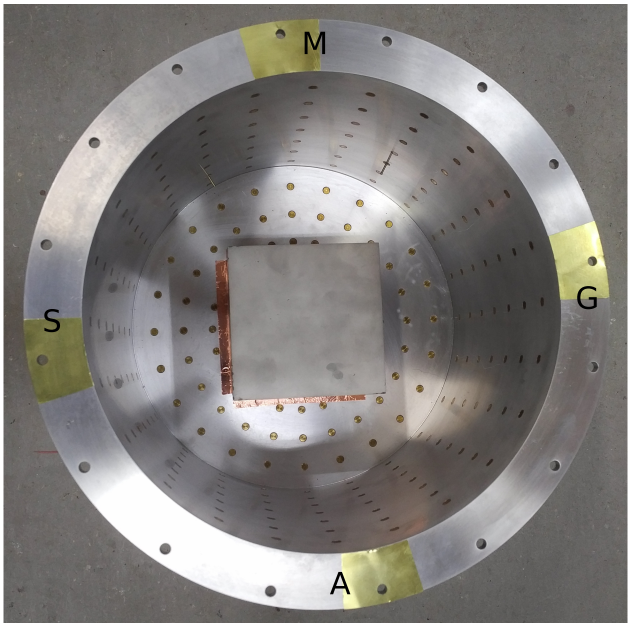

Figure A-2. Shim locations for PV2 slot excitation experiments.

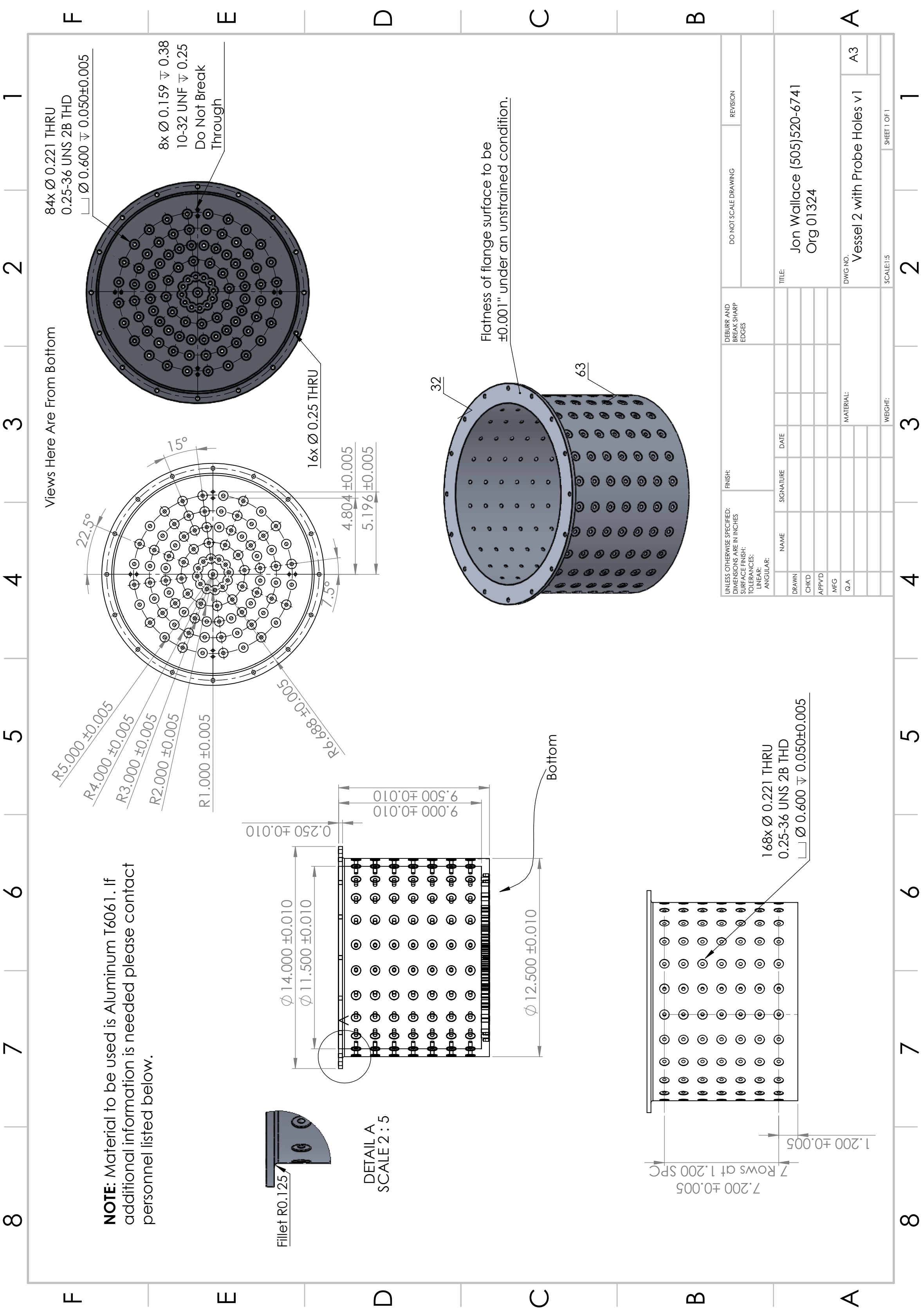

Figure A-3. Mechanical drawing of PV2. The full vessel is made from two identical halves.

Figure A-4. Photo of the SMA plug.

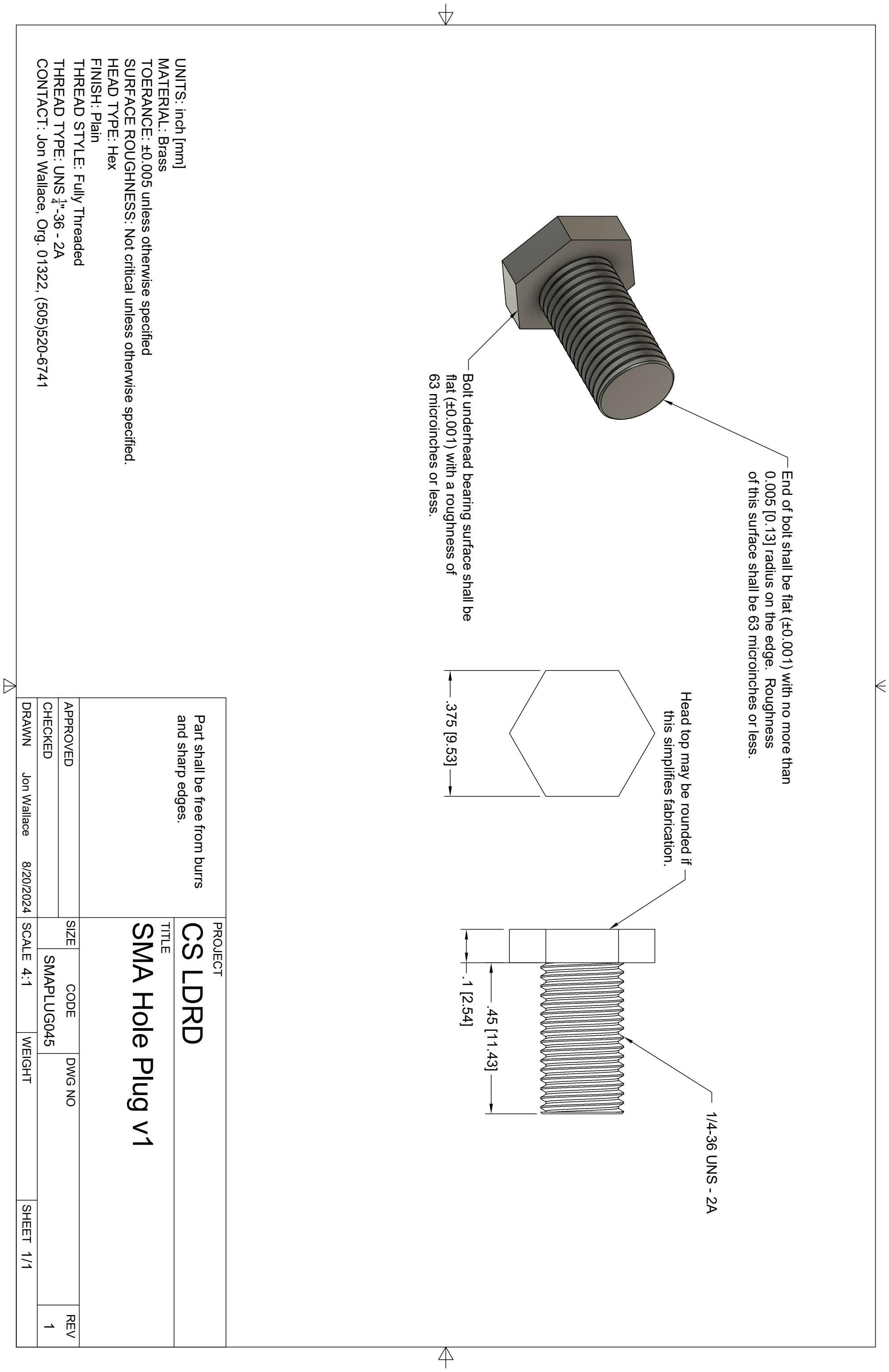

Figure A-5. Mechanical drawing of the SMA plug design.

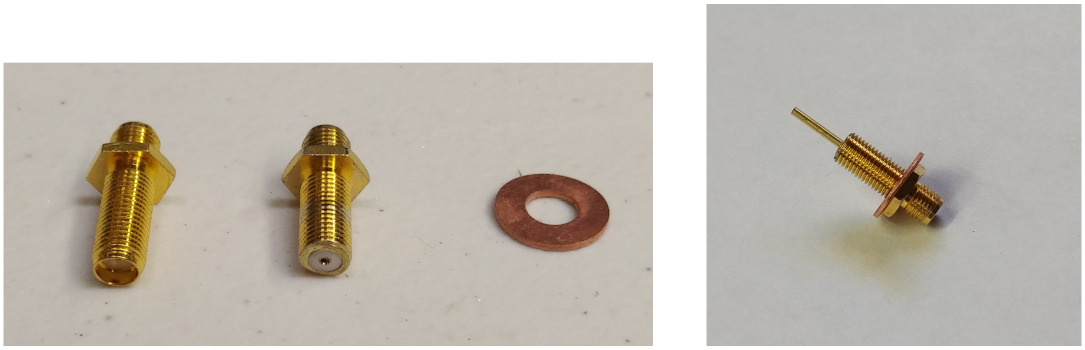

(a) Probe Base Parts

(b) 1 cm Probe

Figure A-6. Probes used in experiments: (a) uncut SMA adapter, final cut SMA adapter, crush washer, (b) completed 1 cm probe.

APPENDIX B. Analytical Mode Solutions of Cylinders

Modes of a cylindrical vessel are given by expressions in [4]. Modes are indexed by three integers

n Tangential (ϕ) variation, $n = 0, 1, \ldots$

m Radial (ρ) variation, $m = 1, 2, \ldots$

ℓ Axial (z) variation, $\ell = 0, 1, \ldots$

B.1. Resonant Frequencies

Modal resonant frequencies for transverse electric (TE) modes are

$$f_{\mathrm{TE},nm\ell} = \frac{c}{2\pi}\sqrt{\left(\frac{p'_{nm}}{a}\right)^2 + \left(\frac{\pi\ell}{d}\right)^2}, \tag{B.1}$$

where $c = 1/\sqrt{\mu\epsilon}$ is the wave velocity in the cavity medium, a is the cylinder radius, d is the cylinder height, and p'_{nm} is the mth zero of the nth order Bessel function derivative satisfying $J'_n(p'_{nm}) = 0$.

Modal resonant frequencies for transverse magnetic (TM) modes are

$$f_{\mathrm{TM},nm\ell} = \frac{c}{2\pi}\sqrt{\left(\frac{p_{nm}}{a}\right)^2 + \left(\frac{\pi\ell}{d}\right)^2}, \tag{B.2}$$

where p_{nm} is the mth zero of the nth order Bessel function satisfying $J_n(p_{nm}) = 0$.

B.2. Quality Factor

The quality factor for TE and TM modes may be found in [1]. For TE modes we have

$$Q_{\mathrm{TE},nm\ell} = \frac{\lambda_0}{2\pi\delta_{\mathrm{S}}}\frac{\left[1 - \left(\frac{n}{p'_{nm}}\right)^2\right]\left[(p'_{nm})^2 + \left(\frac{\ell\pi a}{d}\right)^2\right]^{3/2}}{\left[(p'_{nm})^2 + \frac{2a}{d}\left(\frac{\ell\pi a}{d}\right)^2 + \left(1 - \frac{2a}{d}\right)\left(\frac{n\ell\pi a}{p'_{nm}d}\right)^2\right]}, \tag{B.3}$$

Table B-1. Cylindrical mode fields for $\exp(jn\phi)$ variation.

	TE	TM
E_z	0	$J_n(k_\rho \rho)e^{jn\phi}\cos(k_z z)$
H_z	$J_n(k_\rho \rho)e^{jn\phi}\sin(k_z z)$	0
E_ρ	$\frac{\omega\mu n}{k_\rho^2 \rho} J_n(k_\rho \rho)e^{jn\phi}\sin(k_z z)$	$-\frac{k_z}{k_\rho} J'_n(k_\rho \rho)e^{jn\phi}\sin(k_z z)$
E_ϕ	$j\frac{\omega\mu}{k_\rho} J'_n(k_\rho \rho)e^{jn\phi}\sin(k_z z)$	$-j\frac{k_z n}{k_\rho^2 \rho} J_n(k_\rho \rho)e^{jn\phi}\sin(k_z z)$
H_ρ	$\frac{k_z}{k_\rho} J'_n(k_\rho \rho)e^{jn\phi}\cos(k_z z)$	$-\frac{\omega\epsilon n}{k_\rho^2 \rho} J_n(k_\rho \rho)e^{jn\phi}\cos(k_z z)$
H_ϕ	$j\frac{k_z n}{k_\rho^2 \rho} J_n(k_\rho \rho)e^{jn\phi}\cos(k_z z)$	$-j\frac{\omega\epsilon}{k_\rho} J'_n(k_\rho \rho)e^{jn\phi}\cos(k_z z)$
k_ρ	p'_{nm}/a	p_{nm}/a
k_z	$\pi\ell/d$	$\pi\ell/d$

where $\lambda_0 = c/f_{\text{TE}}$ is the modal wavelength, δ_s is the wall skin depth, given by

$$\delta_{\text{S}} = \sqrt{\frac{1}{\pi f_{\text{TE}}\, \mu_{\text{wall}}\, \sigma_{\text{wall}}}}, \tag{B.4}$$

and μ_{wall} and σ_{wall} are the permeability and conductivity, respectively, of the metallic walls.

For TM modes we have

$$Q_{\text{TM},nm\ell} = \frac{\lambda_0}{2\pi\delta_{\text{S}}} \frac{\sqrt{p_{nm}^2 + \left(\frac{\ell\pi a}{d}\right)^2}}{1 + \delta_\ell \left(\frac{a}{d}\right)}, \tag{B.5}$$

where $\lambda_0 = c/f_{\text{TM}}$ is the modal wavelength, δ_{S} is the wall skin depth, given by

$$\delta_{\text{S}} = \sqrt{\frac{1}{\pi f_{\text{TM}}\, \mu_{\text{wall}}\, \sigma_{\text{wall}}}}, \tag{B.6}$$

and

$$\delta_\ell = \begin{cases} 1, & \ell = 0 \\ 2, & \text{otherwise.} \end{cases} \tag{B.7}$$

B.3. Modal Fields

The most compact way to write modes is to assume $\exp(jn\phi)$ tangential variation, where n is an arbitrary integer (positive, negative, or zero). The expressions for TE and TM modes are given in Table B-1.

Often it is desirable to have real-valued modal functions, which is possible by converting each pair of modes with $e^{jn\phi}$ variation for positive and negative n into a cosine and sine mode pair. Consider a combination of the modes for coefficients $\pm n$, or

$$f(\rho,\phi) = c_n f_n(k_\rho \rho)e^{jn\phi} + c_{-n} f_{-n}(k_\rho \rho)e^{-jn\phi}. \tag{B.8}$$

Table B-2. Conversion from $\exp(jn\phi)$ to $\cos$ and $\sin$ variation.

	TE		TM	
	cos	sin	cos	sin
E_z	0	0	$\cos(n\phi)$	$\sin(n\phi)$
H_z	$\cos(n\phi)$	$\sin(n\phi)$	0	0
E_ρ	$j\sin(n\phi)$	$-j\cos(n\phi)$	$\cos(n\phi)$	$\sin(n\phi)$
E_ϕ	$\cos(n\phi)$	$\sin(n\phi)$	$j\sin(n\phi)$	$-j\cos(n\phi)$
H_ρ	$\cos(n\phi)$	$\sin(n\phi)$	$j\sin(n\phi)$	$-j\cos(n\phi)$
H_ϕ	$j\sin(n\phi)$	$-j\cos(n\phi)$	$\cos(n\phi)$	$\sin(n\phi)$

We can create a $\cos(n\phi)$ mode by letting $c_n = \frac{1}{2}$ and $c_{-n} = \frac{(-1)^n}{2}$, which converts the $e^{jn\phi}$ variation into $\cos n\phi$ (or $j\sin n\phi$) variation when n is not (or is) present in the mode coefficient.

Likewise, we can create a $\sin(n\phi)$ mode by letting $c_n = \frac{1}{2j}$ and $c_{-n} = \frac{(-1)^{n+1}}{2j}$, which converts the $e^{jn\phi}$ variation into $\sin n\phi$ (or $-j\cos n\phi$) variation when n is not (or is) present in the mode coefficient.

Note that deriving these relationships required applying the identity

$$Y_{-n}(x) = \begin{cases} +Y_n(x), & n \text{ even}, \\ -Y_n(x), & n \text{ odd}, \end{cases} \tag{B.9}$$

where $Y_n(x)$ is an arbitrary Bessel function (or derivative).

The required replacements of the $e^{jn\phi}$ term in the modes are summarized in Table B-2 for the cosine and sine modes. Note in Table B-2 that it is possible to derive the sine mode of each mode type (TE or TM) from the cosine mode by replacing $n\phi$ in the cosine column with $n\phi + \phi_0$. Then, the cosine and sine columns are generated with $\phi_0 = 0$ and $\phi_0 = -\pi/2$, respectively. This is a more efficient way to generate the cosine and sine modes in a computer code.

Performing the substitutions described above results in Table B-3. We have multiplied all TE expressions by $-j$, resulting in purely real electric field and purely imaginary magnetic field for both TE and TM modes. We have also used $k = \omega\sqrt{\mu\epsilon}$ and $\eta = \sqrt{\mu/\epsilon}$ in this form of the modal fields.

B.4. Stored Energy and Normalization Integrals

Computation of stored energy is useful for later computation of mode normalization integrals. At a resonance, stored electric and magnetic energy are equal, requiring only one to be computed. Stored electric energy is

$$U_E = \frac{\epsilon}{4} \underbrace{\int_V \left|\overline{E}(\overline{r})\right|^2 dV}_{I_E}, \tag{B.10}$$

Table B-3. Cosine and sine form of cylinder cavity modes. Cosine and sine modes are obtained with $\phi_0 = 0$ and $\phi_0 = -\pi/2$, respectively.

	TE	TM
E_z	0	$J_n(k_\rho \rho)\cos(n\phi + \phi_0)\cos(k_z z)$
H_z	$-jJ_n(k_\rho \rho)\cos(n\phi + \phi_0)\sin(k_z z)$	0
E_ρ	$\frac{k\eta n}{k_\rho^2 \rho} J_n(k_\rho \rho)\sin(n\phi + \phi_0)\sin(k_z z)$	$-\frac{k_z}{k_\rho} J_n'(k_\rho \rho)\cos(n\phi + \phi_0)\sin(k_z z)$
E_ϕ	$\frac{k\eta}{k_\rho} J_n'(k_\rho \rho)\cos(n\phi + \phi_0)\sin(k_z z)$	$\frac{k_z n}{k_\rho^2 \rho} J_n(k_\rho \rho)\sin(n\phi + \phi_0)\sin(k_z z)$
H_ρ	$-j\frac{k_z}{k_\rho} J_n'(k_\rho \rho)\cos(n\phi + \phi_0)\cos(k_z z)$	$-j\frac{kn}{\eta k_\rho^2 \rho} J_n(k_\rho \rho)\sin(n\phi + \phi_0)\cos(k_z z)$
H_ϕ	$j\frac{k_z n}{k_\rho^2 \rho} J_n(k_\rho \rho)\sin(n\phi + \phi_0)\cos(k_z z)$	$-j\frac{k}{\eta k_\rho} J_n'(k_\rho \rho)\cos(n\phi + \phi_0)\cos(k_z z)$

where I_E for a TE mode is computed as

$$I_E = \int_V \left(\left| E_\rho \right|^2 + \left| E_\phi \right|^2 \right) dV. \tag{B.11}$$

Substituting field expressions for an arbitrary TE cosine mode from Table B-3, we obtain

$$I_E = \frac{\pi d k^2 \eta^2 a^4}{4(p'_{nm})^2} \left(1 - \frac{n^2}{(p'_{nm})^2} \right) \left[J_n(p'_{nm}) \right]^2. \tag{B.12}$$

Total stored energy for a TE mode is therefore

$$U_{\mathrm{TE}} = 2U_E = \frac{\epsilon I_E}{2}. \tag{B.13}$$

Stored magnetic energy is

$$U_H = \frac{\mu}{4} \underbrace{\int_V \left| \overline{H}(\overline{r}) \right|^2 dV}_{I_H}, \tag{B.14}$$

where I_H for a TM mode is computed as

$$I_H = \int_V \left(\left| H_\rho \right|^2 + \left| H_\phi \right|^2 \right) dV. \tag{B.15}$$

Substituting field expressions for an arbitrary TM cosine mode from Table B-3, we obtain

$$I_H = \frac{\pi d k^2 a^4}{\delta_n \delta_\ell \, \eta^2 (p_{nm})^2} \left[J_n'(p_{nm}) \right]^2, \tag{B.16}$$

where $\delta_{(\cdot)}$ is given in (B.7). Total stored energy for a TM mode is therefore

$$U_{\mathrm{TM}} = 2U_H = \frac{\mu I_H}{2}. \tag{B.17}$$

Noting that the form of the modes in Table B-3 have purely real electric field and purely imaginary magnetic field, we can readily compute the the following normalization integrals from the stored energy results. For a TE mode we have the normalization integral

$$A_{nm\ell} = \int_V \overline{E}(\overline{r}) \cdot \overline{E}(\overline{r}) dV = \int_V |\overline{E}(\overline{r})|^2 dV = I_E. \tag{B.18}$$

For an arbitrary TM mode we have the normalization integral

$$B_{nm\ell} = \int_V \overline{H}(\overline{r}) \cdot \overline{H}(\overline{r}) dV = \int_V (-|\overline{H}(\overline{r})|^2) dV = -I_H. \tag{B.19}$$

This page intentionally left blank.

APPENDIX C. Numerical Mode Solutions with COMSOL

For most cavity shapes of interest, there is no closed-form solution for the modes. However, modes may be found numerically using finite-element (FEM) solvers, such as COMSOL. In FEM, the modal system of equations results in a sparse matrix eigenvalue / eigenvector problem that may be solved efficiently with sparse eigenvalue solvers like ARPACK [3]. This section describes the setup required to find numerical modes in COMSOL, which may be used in place of closed-form modes when finding internal cavity fields for the theory described in Chapter 2.

C.1. Problem Setup

The following steps should be followed when setting up the analysis problem in COMSOL:

1. A fully enclosed domain should be created that represents the empty space inside of the cavity. The boundaries of the domain represent the cavity walls.
2. No ports or sources should be added to the geometry. It will be assumed that probes and apertures do not appreciably perturb the modal fields inside the cavity.
3. Assuming walls with high conductivity, a perturbation approach is followed, where walls are simulated as perfect electrical conductor (PEC) to find the modes. Later, the quality factor of the modes may be found by accounting for the actual wall conductivity in post-processing.
4. The “eigenfrequency” study is selected in COMSOL, which is depicted in Fig. C-1. Here the maximum number of eigenfrequencies and the range of frequencies to consider is selected. Since we have PEC walls, the imaginary part of the eigenfrequency (loss) can be set to zero.

C.2. Field Export

Modal fields need to be exported for the various modes found in the frequency range of interest. This is performed by creating a new “Data Export” item under the “Export” tab in the Model Builder pane. The “Expressions” table should be populated with eigenfrequencies (freq) and each of the electric and magnetic field components (emw.Ex, emw.Ey, emw.Ez, emw.Hx, emw.Hy, emw.Hz). An example export setup is shown in Figure C-2.

It should be noted that modal fields are exported at nodes on the COMSOL volume mesh, which usually does not form a regular grid. However, conversion to a regular grid or arbitrary observation points can be easily accomplished using interpolation (such as the ScatteredInterpolant in MATLAB).

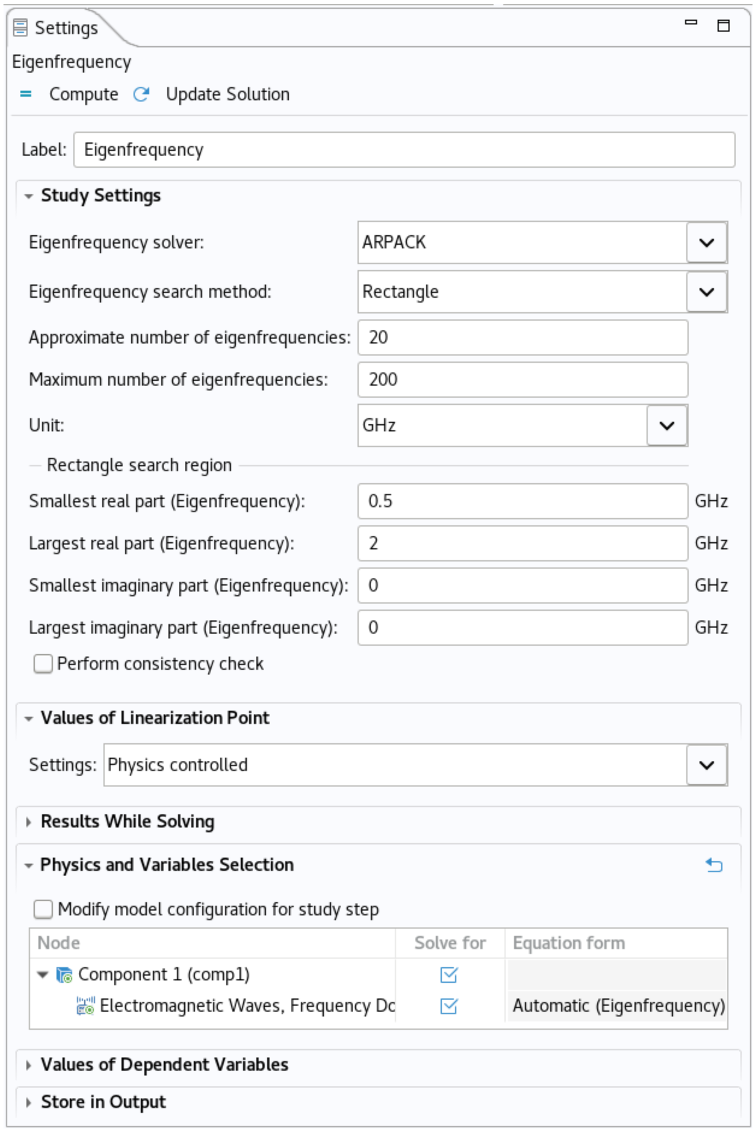

Eigenfrequency

Label: Eigenfrequency

Study Settings

Eigenfrequency solver: ARPACK

Eigenfrequency search method: Rectangle

Approximate number of eigenfrequencies: 20

Maximum number of eigenfrequencies: 200

Unit: GHz

Rectangle search region

Smallest real part (Eigenfrequency): 0.5 GHz

Largest real part (Eigenfrequency): 2 GHz

Smallest imaginary part (Eigenfrequency): 0 GHz

Largest imaginary part (Eigenfrequency): 0 GHz

☐ Perform consistency check

Values of Linearization Point

Settings: Physics controlled

Results While Solving

Physics and Variables Selection

☐ Modify model configuration for study step

Node	Solve for	Equation form
Component 1 (comp1)	☑	
Electromagnetic Waves, Frequency Dc	☑	Automatic (Eigenfrequency)

Values of Dependent Variables

Store in Output

Figure C-1. Eigenfrequency study setup in COMSOL.

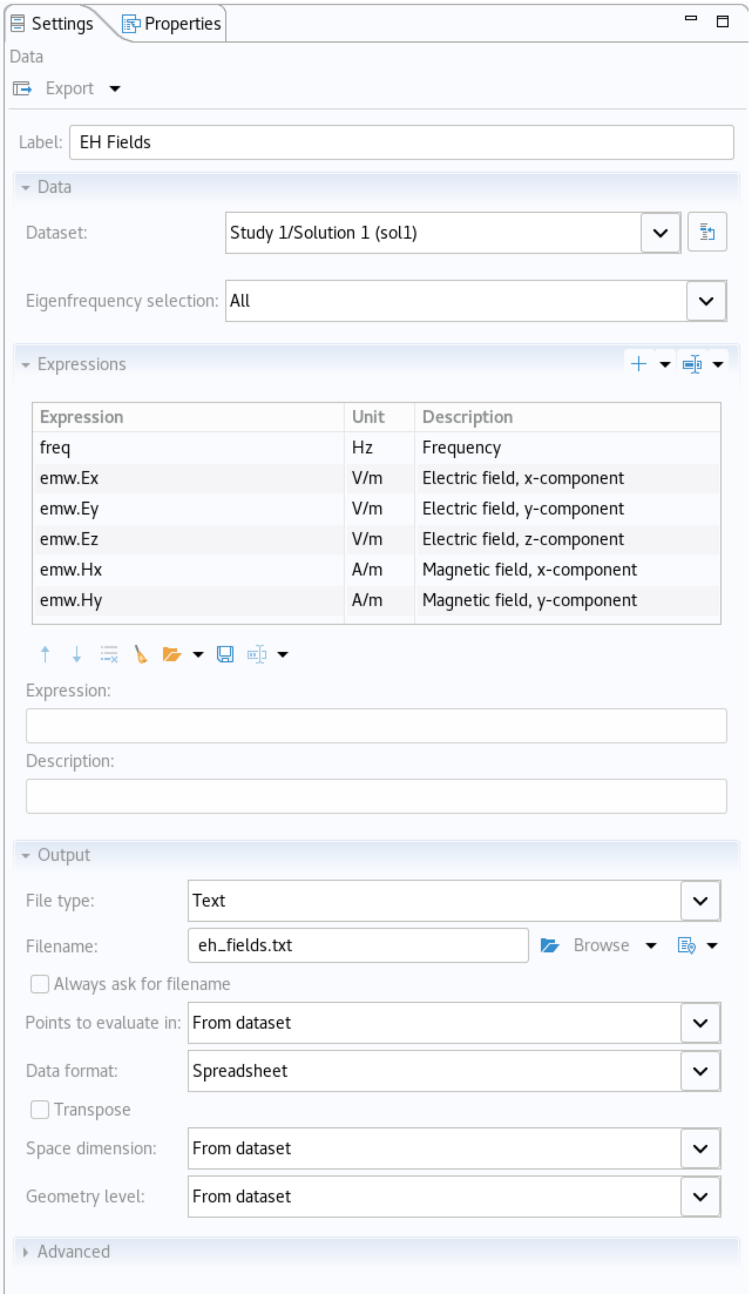

Label: EH Fields

Data

Dataset: Study 1/Solution 1 (sol1)

Eigenfrequency selection: All

Expressions

Expression	Unit	Description
freq	Hz	Frequency
emw.Ex	V/m	Electric field, x-component
emw.Ey	V/m	Electric field, y-component
emw.Ez	V/m	Electric field, z-component
emw.Hx	A/m	Magnetic field, x-component
emw.Hy	A/m	Magnetic field, y-component

Expression:

Description:

Output

File type: Text

Filename: eh_fields.txt

☐ Always ask for filename

Points to evaluate in: From dataset

Data format: Spreadsheet

☐ Transpose

Space dimension: From dataset

Geometry level: From dataset

Figure C-2. Modal field export in COMSOL.

C.3. Dissipated Power Export

To compute quality factor, dissipated power in the cavity walls needs to be computed for each mode, which can be accomplished using the “Results →Derived Values” tab. Dissipated power is computed with the integral

$$P_{\mathrm{d},n} = \frac{R_S}{2} \underbrace{\int_S \left|\hat{n} \times \overline{H}_n\right|^2 dS}_{I_P}, \tag{C.1}$$

where S is the surface consisting of cavity walls, $\hat{n}$ is the inward surface normal, $\overline{H}_n$ is the magnetic field on the wall for the nth mode, the wall resistivity is given by

$$R_S = \sqrt{\frac{\pi f_n \mu_{\mathrm{wall}}}{\sigma_{\mathrm{wall}}}}, \tag{C.2}$$

and f_n is the frequency of the nth mode. In COMSOL it is most convenient to compute and export just the integral I_P in (C.1), which can then be scaled according to $R_S/2$ in later processing.

Figure C-3 shows the setup for computing the dissipated power integral I_P. The translation of I_P into COMSOL variables is as follows:

```
emw.Hx*conj(emw.Hx)*(nz^2 + ny^2) + emw.Hy*conj(emw.Hy)*(nx^2 + nz^2) +
emw.Hz*conj(emw.Hz)*(nx^2 + ny^2) - 2*nx*ny*real(emw.Hx*conj(emw.Hy)) -
2*nx*nz*real(emw.Hx*conj(emw.Hz)) - 2*ny*nz*real(emw.Hy*conj(emw.Hz))
```

For the simplest model, the wall conductivity is the same for all surfaces. However, it is possible to create multiple derived values for different surfaces and export I_P separately for each one. Then, the total dissipated power would be the sum of these exported quantities scaled by $R_S/2$ of each surface.

When evaluating a derived value, a table is created which can then be exported to an ASCII file using the “Export” tab.

C.4. Stored Energy and Mode Normalization Export

Computation of quality factor requires stored energy of each mode to be computed. Total stored energy of the nth mode is the sum of electric and magnetic stored energy, or

$$U_n = U_{\mathrm{E},n} + U_{\mathrm{H},n}. \tag{C.3}$$

Electric stored energy is computed as

$$U_{\mathrm{E},n} = \frac{\epsilon}{4} \int_V |\overline{E}_n|^2 dV, \tag{C.4}$$

which can be computed in COMSOL using a volume integral “Derived Result” with the equation

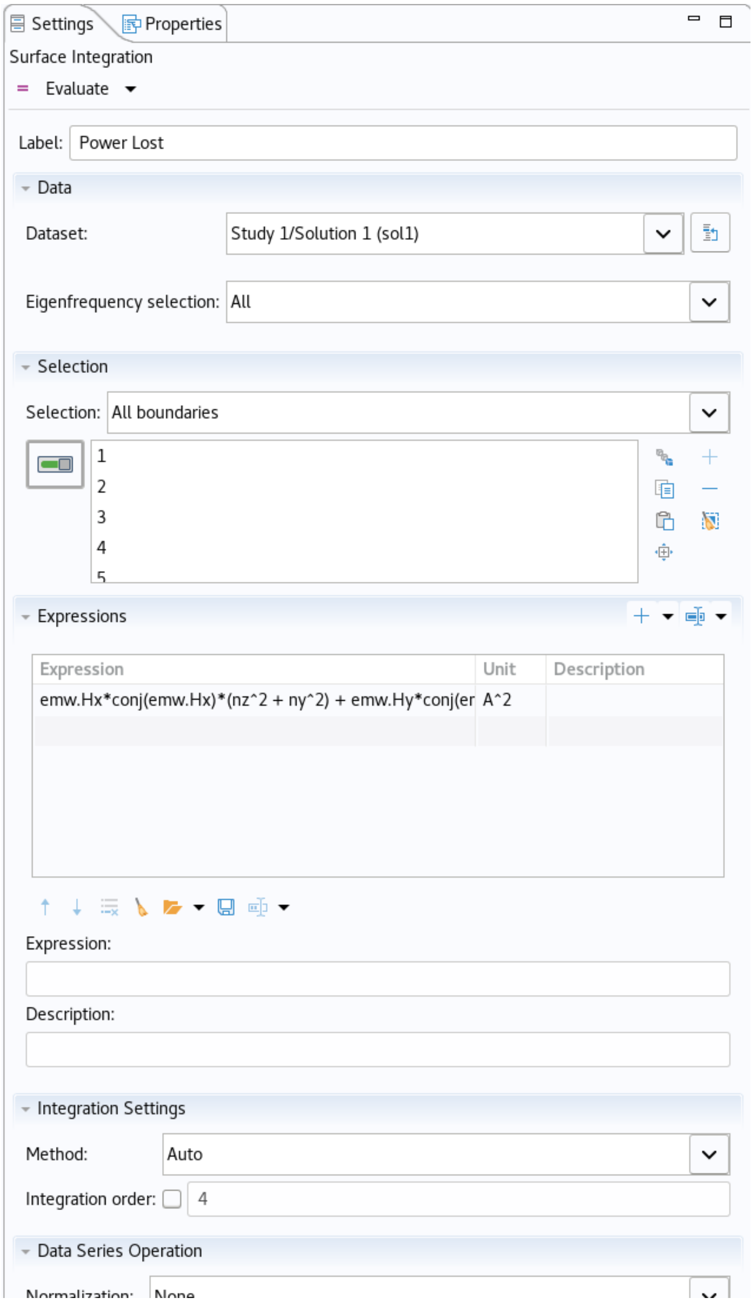

Surface Integration

Label: Power Lost

Data

Dataset: Study 1/Solution 1 (sol1)

Eigenfrequency selection: All

Selection

Selection: All boundaries

1
2
3
4
5

Expressions

Expression	Unit	Description
emw.Hx*conj(emw.Hx)*(nz^2 + ny^2) + emw.Hy*conj(er	A^2	

Expression:

Description:

Integration Settings

Method: Auto

Integration order: ☐ 4

Data Series Operation

Normalization: None

Figure C-3. Power loss computation in COMSOL.

```
epsilon0_const/4*(emw.Ex*conj(emw.Ex) + emw.Ey*conj(emw.Ey)
+ emw.Ez*conj(emw.Ez))
```

Magnetic stored energy is computed as

$$U_{\mathrm{H},n} = \frac{\mu}{4}\int_V |\overline{H}_n|^2 dV, \tag{C.5}$$

which can be computed in COMSOL using a volume integral "Derived Result" with the equation

```
mu0_const/4*(emw.Hx*conj(emw.Hx) + emw.Hy*conj(emw.Hy)
+ emw.Hz*conj(emw.Hz))
```

In addition to stored energy, normalization constants for electric and magnetic fields are needed for subsequent modal analysis, given by

$$A_n = \int_V \overline{E}_n(\overline{r}) \cdot \overline{E}_n(\overline{r}) dV, \tag{C.6}$$

$$B_n = \int_V \overline{H}_n(\overline{r}) \cdot \overline{H}_n(\overline{r}) dV, \tag{C.7}$$

which are computed in COMSOL with the volume integrands

```
emw.Ex^2 + emw.Ey^2 + emw.Ez^2
```

```
emw.Hx^2 + emw.Hy^2 + emw.Hz^2
```

respectively.

The setup for the stored energy and field normalization computation is shown in Figure C-4. Data is evaluated to a table and exported using the "Export" tab as before.

C.5. Quality Factor Computation

Given the numerical values for wall dissipated power and stored energy described in the previous sections, the quality factor for each mode is computed as

$$Q_n = \frac{2\pi U_n}{P_{\mathrm{d},n}}. \tag{C.8}$$

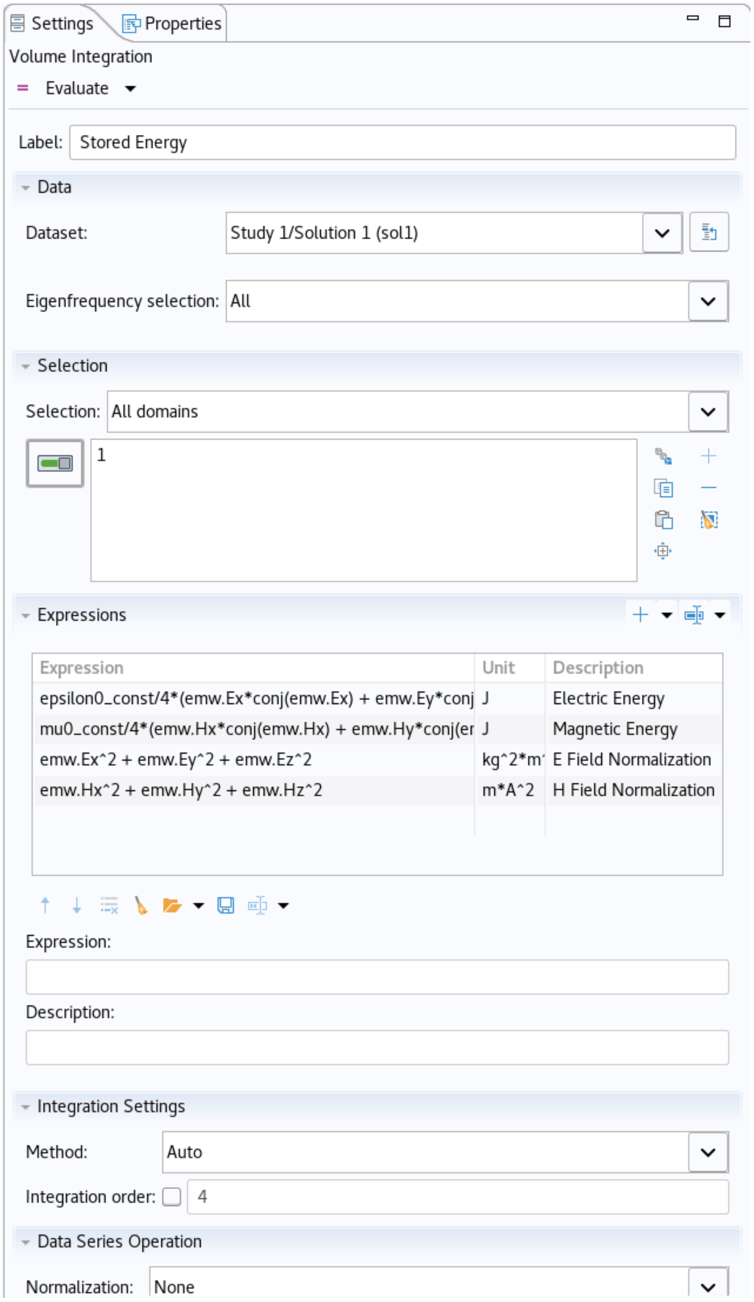

Label: Stored Energy

Data

Dataset: Study 1/Solution 1 (sol1)

Eigenfrequency selection: All

Selection

Selection: All domains

1

Expressions

Expression	Unit	Description
epsilon0_const/4*(emw.Ex*conj(emw.Ex) + emw.Ey*conj	J	Electric Energy
mu0_const/4*(emw.Hx*conj(emw.Hx) + emw.Hy*conj(e	J	Magnetic Energy
emw.Ex^2 + emw.Ey^2 + emw.Ez^2	kg^2*m	E Field Normalization
emw.Hx^2 + emw.Hy^2 + emw.Hz^2	m*A^2	H Field Normalization

Expression:

Description:

Integration Settings

Method: Auto

Integration order: ☐ 4

Data Series Operation

Normalization: None

Figure C-4. Stored energy and field normalization computation in COMSOL.

This page intentionally left blank.

APPENDIX D. Random Probe Sets

Two hundred random probe sets were generated for use in simulation and experimental studies in this work. Here the probe sets are listed, allowing them to be referred to elsewhere by a numerical index. Each probe set has six probe locations. When only four probes are used, the first four probe locations are used. The row (number) and column (letter) designations of the ports are shown in Fig. A-1.

1	13K, 10K, 17M, 14S, 14X, 14W	68	11K, 16I, 8F, 16S, 8T, 17M	135	16J, 13B, 3S, 14J, 8N, 12P
2	11N, 8H, 11T, 3M, 3P, 9I	69	14K, 6L, 9T, 4E, 10V, 12I	136	13G, 7X, 13N, 16I, 14V, 7U
3	13C, 18T, 9B, 6B, 8T, 16B	70	14A, 11V, 14L, 12J, 17O, 8M	137	15D, 12H, 11D, 6U, 11M, 12C
4	9V, 8H, 14H, 8E, 10P, 2K	71	1Q, 10L, 10V, 17C, 15P, 17F	138	17E, 7E, 4U, 12D, 17M, 15J
5	9X, 18H, 9K, 17M, 13L, 6P	72	19G, 3L, 9J, 11X, 3R, 16V	139	19G, 5T, 1M, 11E, 4T, 7O
6	3W, 6A, 17V, 16S, 17J, 15E	73	13P, 9W, 10T, 19M, 16X, 15T	140	12T, 14E, 19M, 10M, 4E, 16F
7	4C, 14A, 12T, 14R, 7W, 11T	74	19P, 3J, 13K, 1I, 3I, 5K	141	16Q, 17A, 12Q, 16V, 7U, 3X
8	2Q, 9C, 12I, 16N, 19T, 18G	75	11U, 4F, 5S, 12U, 1W, 4E	142	16N, 3W, 14W, 9B, 15O, 12H
9	4F, 16D, 16L, 13W, 5T, 7T	76	11N, 0A, 12H, 11B, 15C, 2I	143	5L, 12E, 13U, 11C, 3O, 17X
10	3N, 7D, 12P, 13B, 19H, 10X	77	14W, 14I, 19C, 15W, 13D, 3N	144	19H, 12C, 11D, 8B, 19Q, 11M
11	11W, 2S, 8O, 2I, 10K, 16A	78	5U, 7P, 4K, 15H, 18Q, 4X	145	10M, 13H, 11E, 4T, 9H, 6V
12	18C, 11K, 10N, 3N, 18U, 12I	79	1I, 13O, 17J, 10T, 9D, 8B	146	12N, 1U, 7J, 13C, 6V, 4M
13	9H, 18B, 3W, 14Q, 17Q, 14K	80	17E, 6V, 1S, 10R, 10F, 18L	147	6H, 15I, 8E, 17E, 8P, 8V
14	11P, 16I, 4C, 8R, 4V, 7P	81	12K, 15M, 18T, 16R, 10U, 14P	148	8J, 3E, 13I, 9I, 19A, 18I
15	6B, 2C, 15L, 7K, 11A, 3P	82	7L, 18J, 18W, 6K, 9X, 17O	149	10B, 10P, 18B, 8S, 16E, 15B
16	15H, 4G, 11K, 5O, 8T, 13D	83	9O, 5B, 6L, 8F, 3P, 1C	150	14L, 15Q, 18P, 3S, 5H, 9L
17	13D, 7A, 6R, 13R, 16E, 9B	84	6G, 13C, 2O, 18P, 11B, 10O	151	4R, 3C, 3D, 11I, 17X, 15K
18	10J, 3W, 2U, 8N, 1G, 14L	85	18O, 8X, 14T, 11I, 8M, 18W	152	3J, 5G, 14N, 19Q, 4H, 6K
19	15H, 12K, 17T, 8E, 1K, 5J	86	17U, 10R, 7P, 14L, 18P, 16A	153	8D, 11H, 10L, 17M, 16F, 7I
20	3E, 15K, 11F, 19G, 7B, 7W	87	6T, 12G, 7B, 3E, 9S, 6Q	154	6G, 13E, 18V, 8O, 10R, 2C
21	13L, 9Q, 3C, 12P, 16X, 12V	88	11A, 8A, 7X, 17S, 16B, 2E	155	18G, 10U, 6V, 18B, 10R, 6S
22	1W, 18M, 16Q, 16T, 4M, 5R	89	3W, 6D, 18W, 17H, 13W, 10A	156	7O, 4X, 3X, 10B, 18W, 16W
23	15R, 2W, 9M, 17G, 6L, 19Q	90	8A, 9G, 17F, 17T, 3C, 11D	157	2E, 7K, 19D, 14U, 18V, 12F
24	18U, 10B, 9U, 10K, 3U, 4O	91	13S, 6T, 9R, 3D, 11D, 1W	158	18F, 11K, 14K, 16K, 9U, 13P
25	18N, 10V, 6R, 17K, 17I, 7H	92	6G, 19H, 11I, 5V, 13N, 8C	159	14U, 7W, 6F, 6D, 2A, 5C
26	3M, 7V, 8E, 3P, 3C, 9E	93	18A, 8Q, 5Q, 8B, 17D, 10M	160	19E, 9E, 16O, 2A, 2Q, 14T
27	11H, 14X, 14T, 18G, 5F, 17Q	94	15J, 7H, 12B, 12K, 9V, 11H	161	14I, 6J, 11B, 17V, 15G, 18P
28	10F, 18F, 4I, 18K, 4C, 6M	95	18U, 2W, 6H, 9M, 12G, 16J	162	7A, 7T, 14K, 6M, 9Q, 10P
29	11D, 9U, 15L, 6A, 0A, 17G	96	19E, 6V, 13I, 11X, 15J, 18K	163	19N, 6I, 14Q, 10R, 6R, 13Q
30	9G, 19O, 4K, 19D, 10N, 10M	97	8E, 10L, 15R, 14M, 11O, 8P	164	17T, 8F, 4W, 2A, 5R, 12E
31	17F, 3U, 15H, 7G, 9L, 8U	98	17V, 18N, 13S, 8E, 13V, 10H	165	8I, 7H, 19V, 10A, 8N, 2S
32	13L, 2A, 0A, 1A, 15P, 18R	99	8N, 10R, 4L, 15W, 15E, 15H	166	3B, 6S, 3H, 7D, 5C, 7K
33	13Q, 17E, 10J, 4P, 4F, 14L	100	6T, 17I, 7E, 19G, 7W, 6C	167	3W, 2A, 14N, 13T, 9P, 18L
34	0A, 9F, 2G, 10M, 3N, 12G	101	8T, 19W, 17W, 16V, 16A, 13W	168	13M, 3L, 7I, 12D, 13V, 5X
35	16G, 15F, 1A, 19G, 6E, 10P	102	13L, 4B, 12Q, 18T, 16W, 14L	169	4N, 17B, 2O, 11Q, 14W, 3S
36	9P, 4B, 5A, 3P, 3L, 5K	103	18E, 5W, 18V, 15B, 4V, 19H	170	13X, 8L, 19X, 11L, 9K, 13C
37	15W, 3X, 18D, 8U, 14I, 15B	104	15I, 12L, 14I, 9F, 9Q, 6M	171	5T, 14T, 13J, 6E, 14W, 7K
38	13X, 1O, 19U, 18Q, 10L, 18T	105	12G, 2E, 15V, 6Q, 7R, 3X	172	15R, 18R, 17B, 8A, 7I, 17R
39	8I, 19C, 16O, 19G, 9S, 9W	106	3W, 16R, 4W, 9B, 15R, 13C	173	18A, 14B, 4U, 2U, 15J, 18D
40	1A, 13A, 15G, 1M, 9C, 9Q	107	13U, 4T, 16B, 7G, 13F, 17C	174	6E, 4M, 14G, 13V, 3K, 7B
41	19L, 13O, 12P, 17N, 10U, 18K	108	6S, 13C, 17M, 4C, 5W, 13X	175	11L, 5U, 4N, 9A, 6E, 2G
42	7H, 13F, 2O, 19K, 12B, 16J	109	15V, 11X, 17F, 8X, 10C, 8N	176	17G, 12D, 14C, 14F, 14E, 13C
43	13R, 6U, 16G, 5J, 16J, 15L	110	18M, 13S, 12N, 15U, 9T, 9M	177	8J, 17L, 1M, 18Q, 19C, 12M
44	19D, 17N, 7H, 8G, 4B, 19P	111	14H, 5K, 17I, 6X, 7J, 4A	178	3D, 10B, 12I, 12O, 13E, 15C
45	6T, 9A, 4F, 6R, 4X, 6X	112	3L, 14X, 17H, 13X, 16Q, 13P	179	13I, 3V, 3F, 11X, 7L, 8S
46	17M, 8T, 19T, 17I, 12R, 8P	113	12U, 11X, 15P, 5E, 15E, 6I	180	7E, 8N, 14K, 4O, 6L, 1W
47	5H, 2E, 19T, 10X, 3V, 16A	114	16W, 19J, 16H, 18O, 11S, 3M	181	18R, 18J, 3Q, 17X, 13K, 9P
48	15R, 10W, 11W, 6N, 12I, 7V	115	3J, 18R, 6G, 12E, 11T, 13R	182	16Q, 2G, 7H, 19H, 9J, 10F
49	12H, 7L, 14J, 9Q, 4U, 9W	116	8P, 5O, 18B, 3K, 14W, 16I	183	13I, 13Q, 5T, 18V, 8D, 12W
50	4K, 16P, 16S, 6N, 14S, 11O	117	17W, 11O, 6H, 7C, 9R, 9Q	184	17F, 13A, 14F, 14K, 10Q, 4Q
51	18P, 15S, 11R, 18E, 15K, 4K	118	19P, 18D, 12V, 12K, 11L, 8Q	185	4D, 19S, 4X, 10N, 14A, 9F
52	16B, 13J, 3U, 5D, 13P, 10S	119	13D, 5V, 15K, 5E, 18K, 1W	186	19V, 9A, 16T, 10U, 19A, 10R
53	3J, 13O, 17C, 7K, 3P, 3A	120	5A, 4F, 11R, 17B, 14F, 8K	187	10Q, 3E, 13V, 3K, 12A, 17P
54	4R, 10J, 18U, 9I, 3K, 14I	121	10G, 17X, 14B, 7G, 10F, 12B	188	4G, 4P, 8C, 12F, 5K, 15T
55	8B, 14N, 3C, 10H, 7H, 4H	122	19L, 19W, 8S, 5N, 13M, 10H	189	11F, 16P, 8L, 13T, 7C, 14B
56	19A, 4K, 3X, 11D, 7L, 16W	123	6I, 3W, 16X, 8P, 17T, 15K	190	19M, 17M, 16N, 2C, 12H, 19N
57	5E, 7V, 19Q, 8R, 16I, 9G	124	14J, 16Q, 12N, 10X, 11X, 15K	191	3Q, 13J, 7D, 6E, 10E, 5T
58	14T, 12M, 17C, 18W, 9T, 19J	125	17F, 15D, 16W, 4G, 9E, 7U	192	12E, 12L, 16H, 10F, 11O, 4P
59	11U, 7U, 9R, 12L, 1C, 18X	126	10A, 16Q, 9A, 18K, 5G, 19L	193	15A, 11P, 13O, 10L, 11W, 10J
60	14V, 6E, 9E, 16G, 8B, 10K	127	2G, 15T, 19G, 9D, 4W, 18C	194	4I, 13L, 8J, 10Q, 9X, 2S
61	17S, 7H, 18F, 2E, 19M, 4A	128	12S, 13T, 2A, 12F, 18E, 9G	195	1W, 16H, 14A, 2M, 19H, 13I
62	5H, 8H, 14A, 12R, 11V, 10A	129	12V, 16F, 14F, 13B, 15V, 9U	196	7H, 7M, 5Q, 13E, 8X, 6I
63	12Q, 17X, 11N, 1A, 7S, 14J	130	13F, 19V, 8R, 5K, 17L, 13X	197	3I, 3B, 15Q, 8P, 12E, 4L
64	9D, 11S, 10K, 7B, 18F, 3P	131	8B, 13D, 11R, 4I, 16V, 10K	198	17O, 13J, 17L, 5C, 10I, 19B
65	6P, 10S, 8D, 16V, 17C, 4F	132	15X, 3U, 16M, 14D, 3M, 17F	199	18Q, 3E, 7H, 15J, 9D, 14N
66	7L, 18Q, 5F, 9O, 5C, 16X	133	14W, 5K, 3U, 8O, 16D, 4N	200	5N, 18P, 3L, 5M, 12H, 3F
67	2G, 15X, 19U, 1U, 4U, 3U	134	19F, 11U, 1C, 4E, 5K, 10G		

APPENDIX E. Reconstruction Plots

E.1. Empty PV2 with Probe Injection

This appendix plots detailed reconstructions of all of the measurement cases described in this report. Each measured reconstruction is also compared with a simulation for the same ports for verification purposes.

E.1.1. Six Probes

E.1.1.1. Good Random Probe Set (Measured)

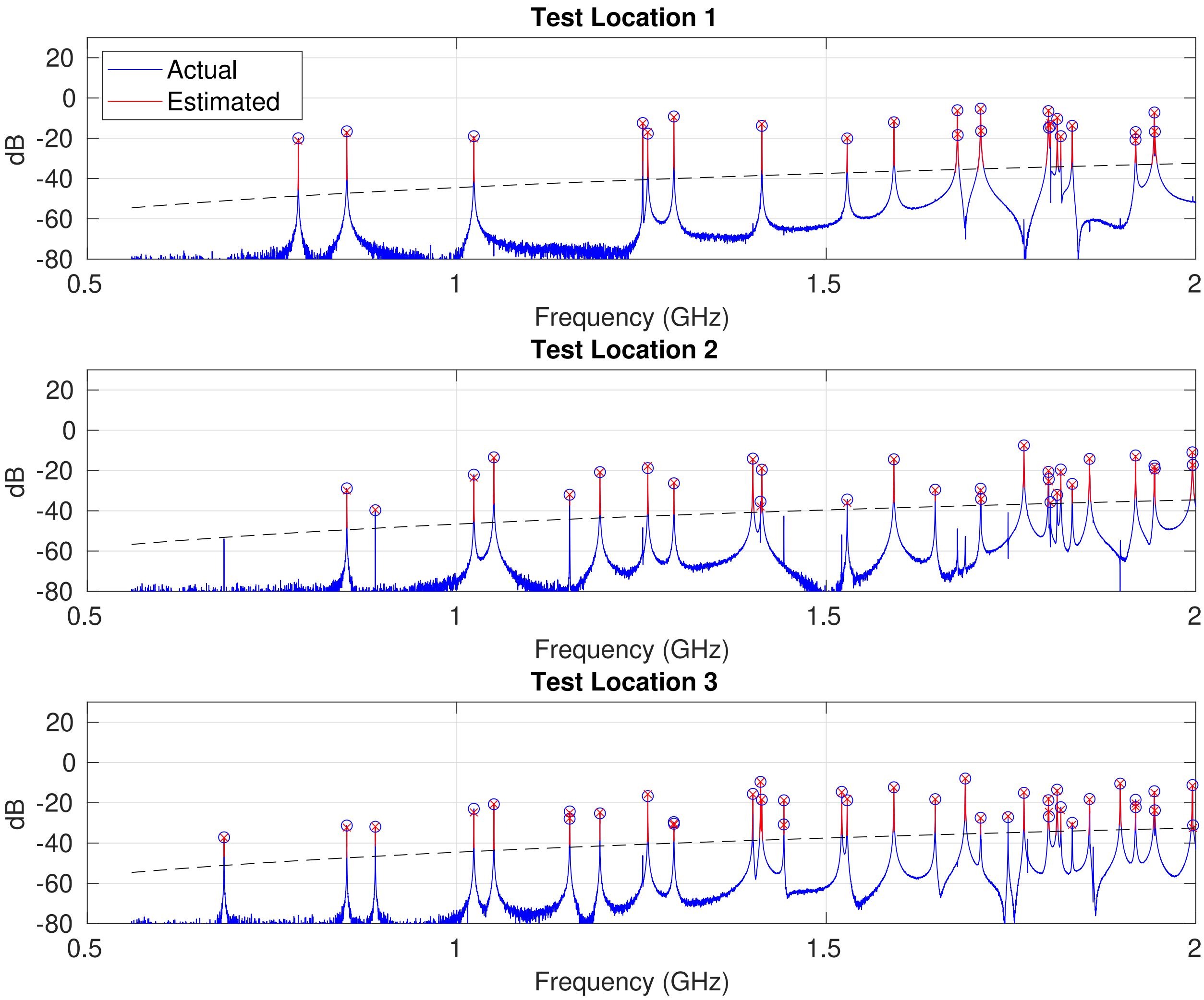

Test Port	P_{missed}	$\text{Error}_{90\%}$	$\text{Error}_{\text{Avg}}$
1	0.00 %	1.1 dB	0.5 dB
2	0.00 %	1.5 dB	0.6 dB
3	0.00 %	1.5 dB	0.6 dB

Figure E-1. Measured good random probe set in empty PV2 with six probes.

E.1.1.2. Good Random Probe Set (Simulated)

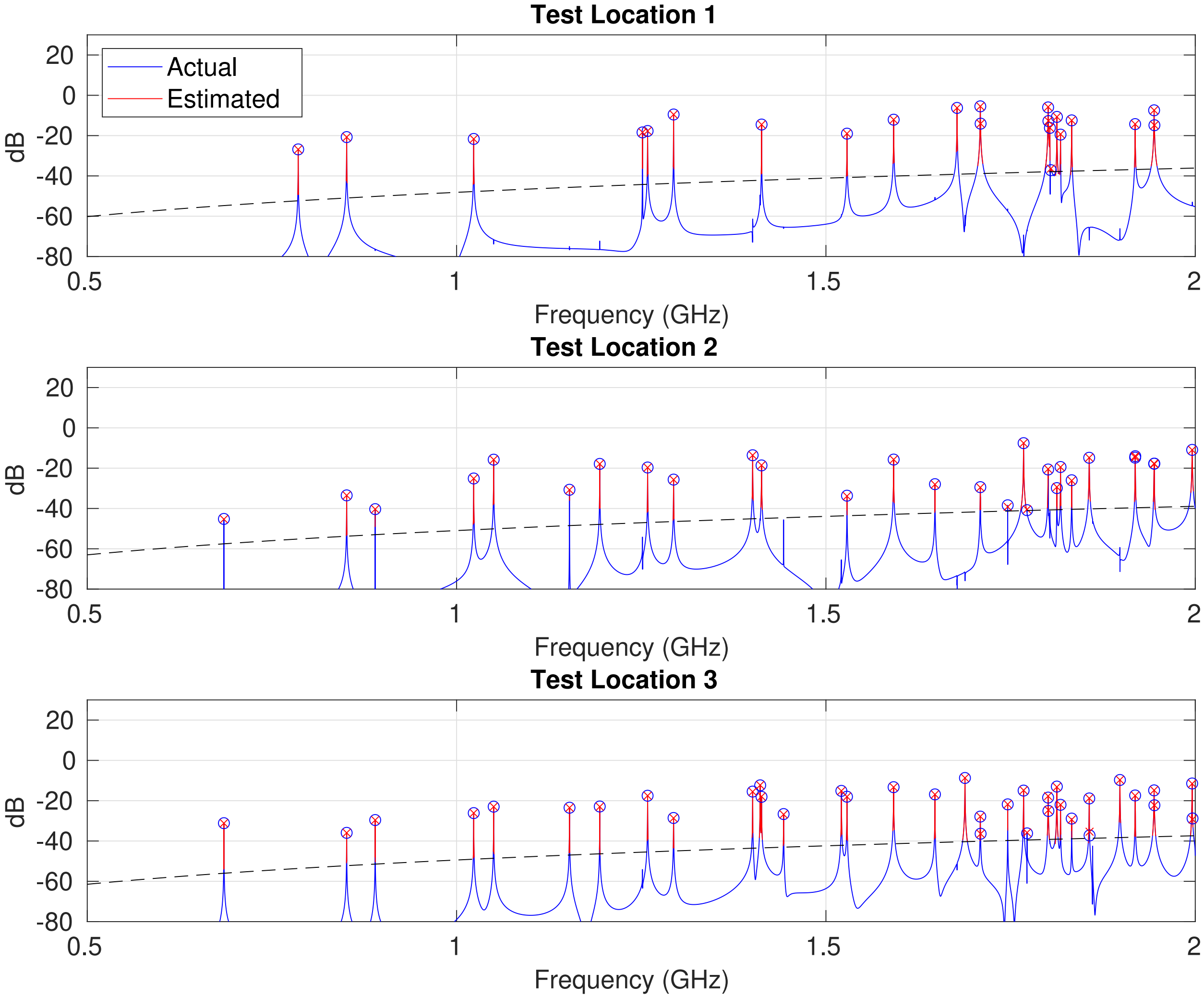

Test Port	P_{missed}	$\text{Error}_{90\%}$	$\text{Error}_{\text{Avg}}$
1	0.00 %	0.2 dB	0.1 dB
2	0.00 %	0.4 dB	0.1 dB
3	0.00 %	0.5 dB	0.2 dB

Figure E-2. Simulated good random probe set in empty PV2 with six probes.

E.1.1.3. Bad Random Probe Set (Measured)

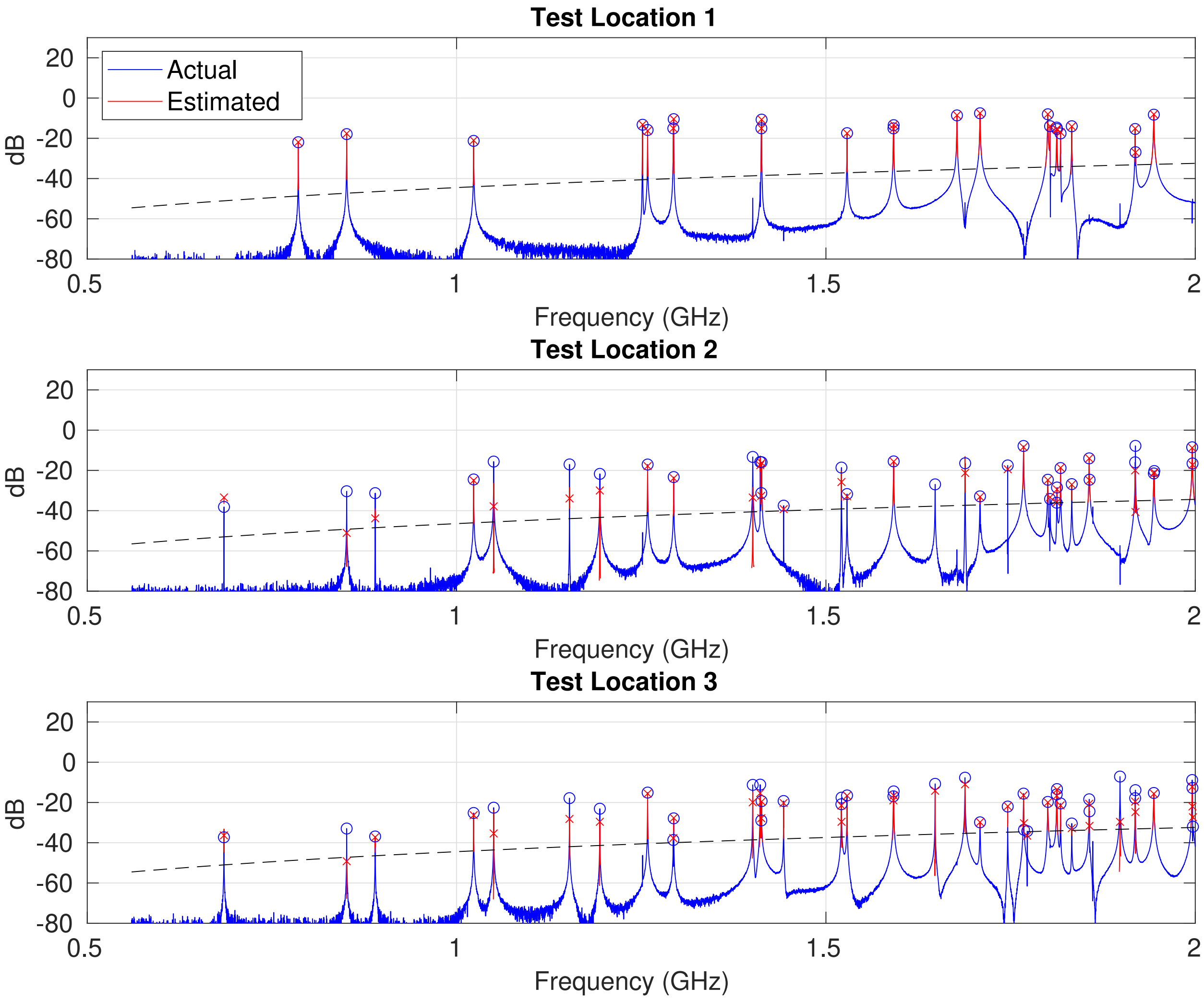

Test Port	P_{missed}	$\text{Error}_{90\%}$	$\text{Error}_{\text{Avg}}$
1	0.00 %	0.5 dB	0.2 dB
2	19.44 %	4.8 dB	1.5 dB
3	14.63 %	6.5 dB	2.2 dB

Figure E-3. Measured bad random probe set in empty PV2 with six probes.

E.1.1.4. Bad Random Probe Set (Simulated)

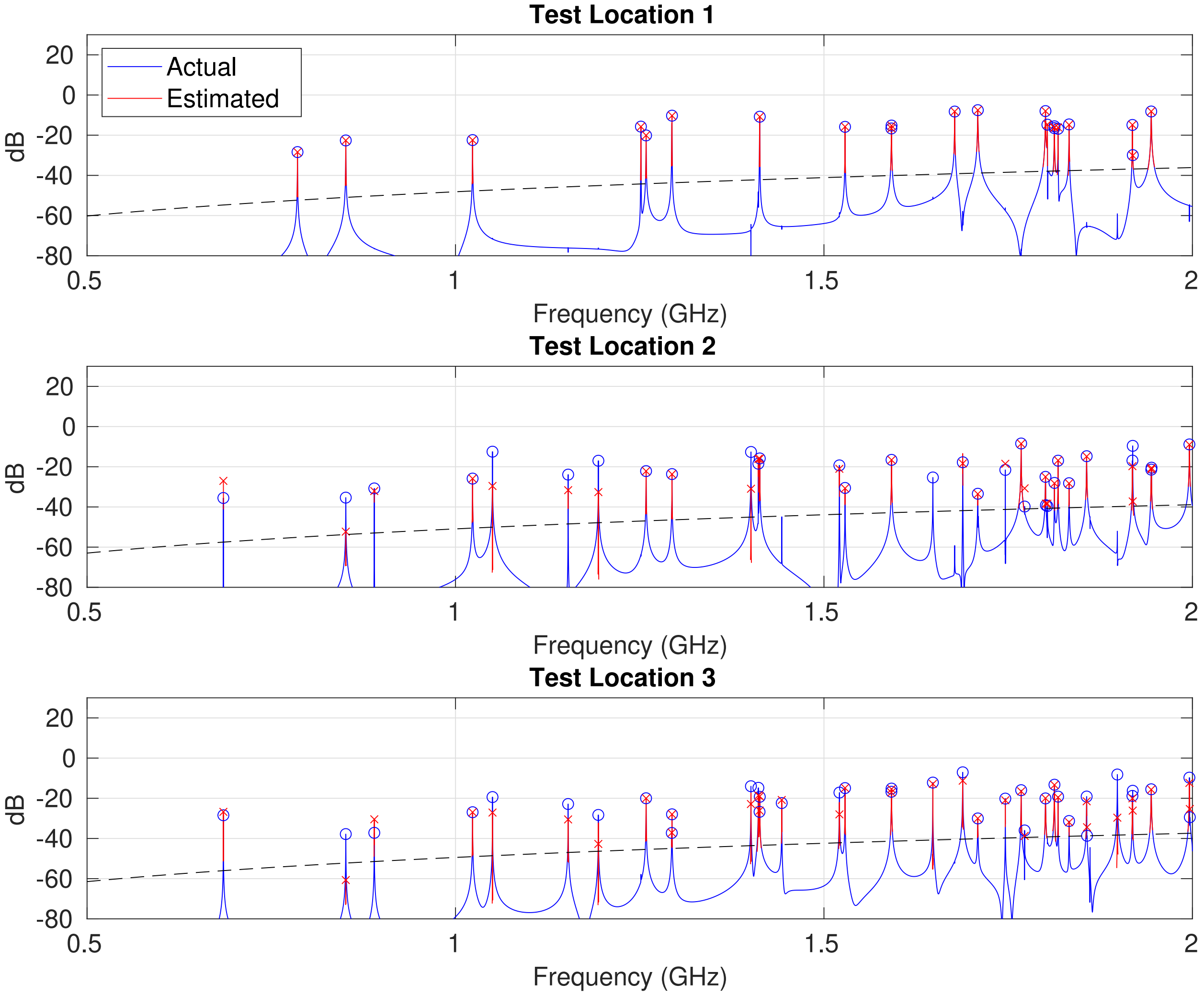

Test Port	P_{missed}	$\text{Error}_{90\%}$	$\text{Error}_{\text{Avg}}$
1	0.00 %	0.2 dB	0.1 dB
2	18.18 %	7.8 dB	1.5 dB
3	10.81 %	7.7 dB	2.3 dB

Figure E-4. Simulated bad random probe set in empty PV2 with six probes.

E.1.1.5. Heuristic Probe Set (Measured)

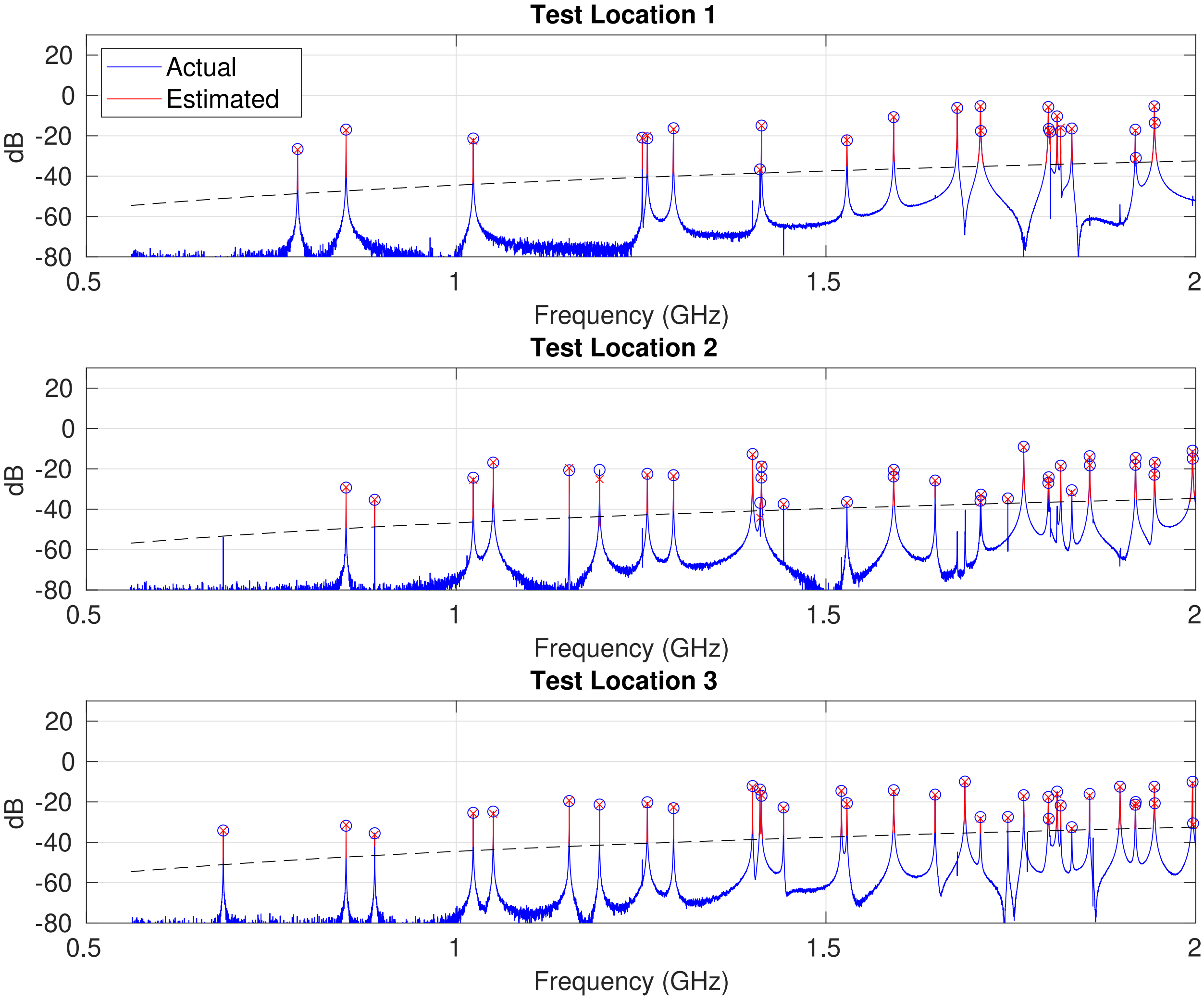

Test Port	P_{missed}	$\text{Error}_{90\%}$	$\text{Error}_{\text{Avg}}$
1	0.00 %	1.1 dB	0.4 dB
2	0.00 %	1.1 dB	0.7 dB
3	0.00 %	0.9 dB	0.5 dB

Figure E-5. Measured heuristic probe set in empty PV2 with six probes.

E.1.1.6. Heuristic Probe Set (Simulated)

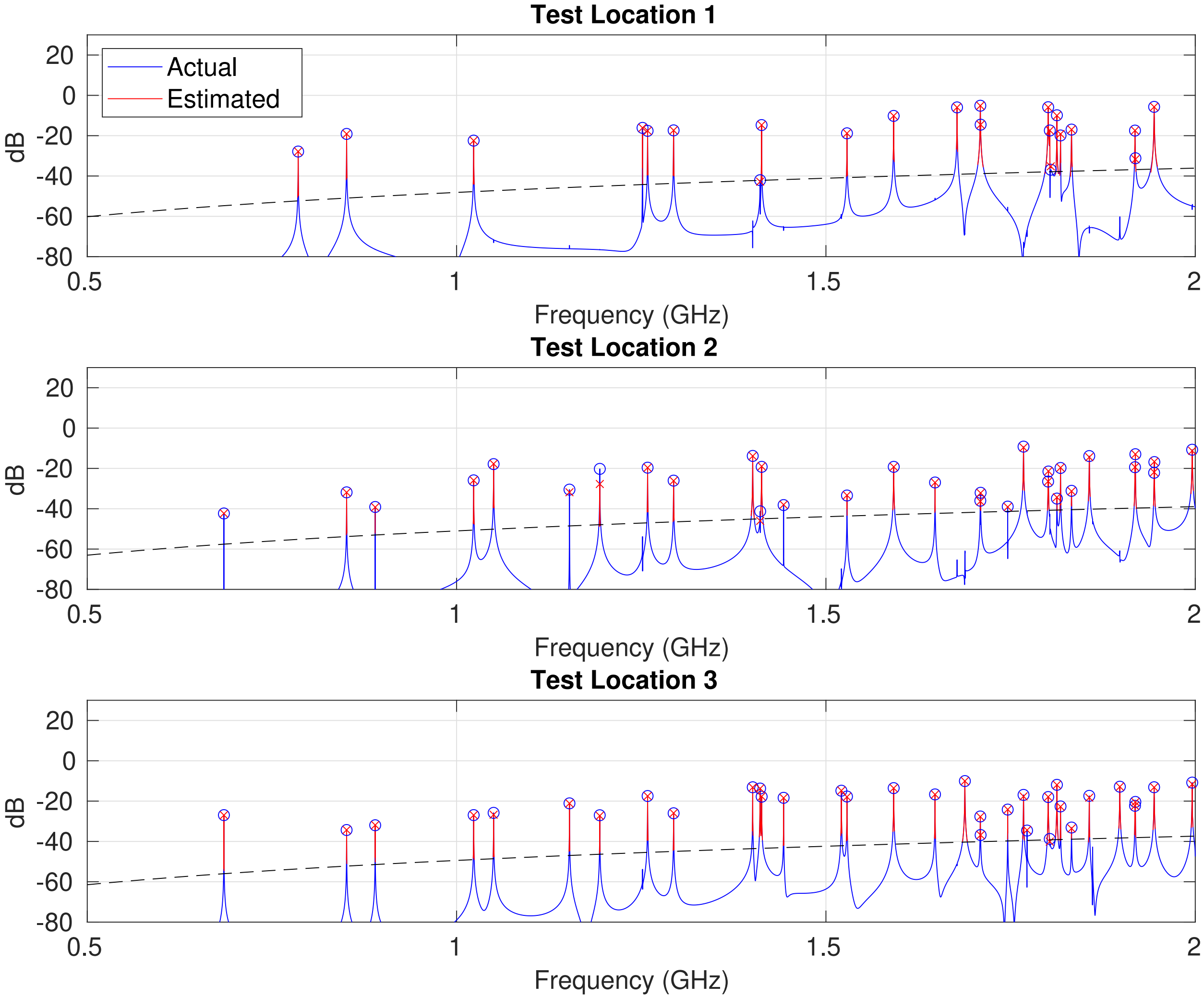

Test Port	P_{missed}	$\text{Error}_{90\%}$	$\text{Error}_{\text{Avg}}$
1	0.00 %	0.7 dB	0.2 dB
2	0.00 %	0.7 dB	0.6 dB
3	0.00 %	0.8 dB	0.2 dB

Figure E-6. Simulated heuristic probe set in empty PV2 with six probes.

E.1.2. Four Probes

E.1.2.1. Good Random Probe Set (Measured)

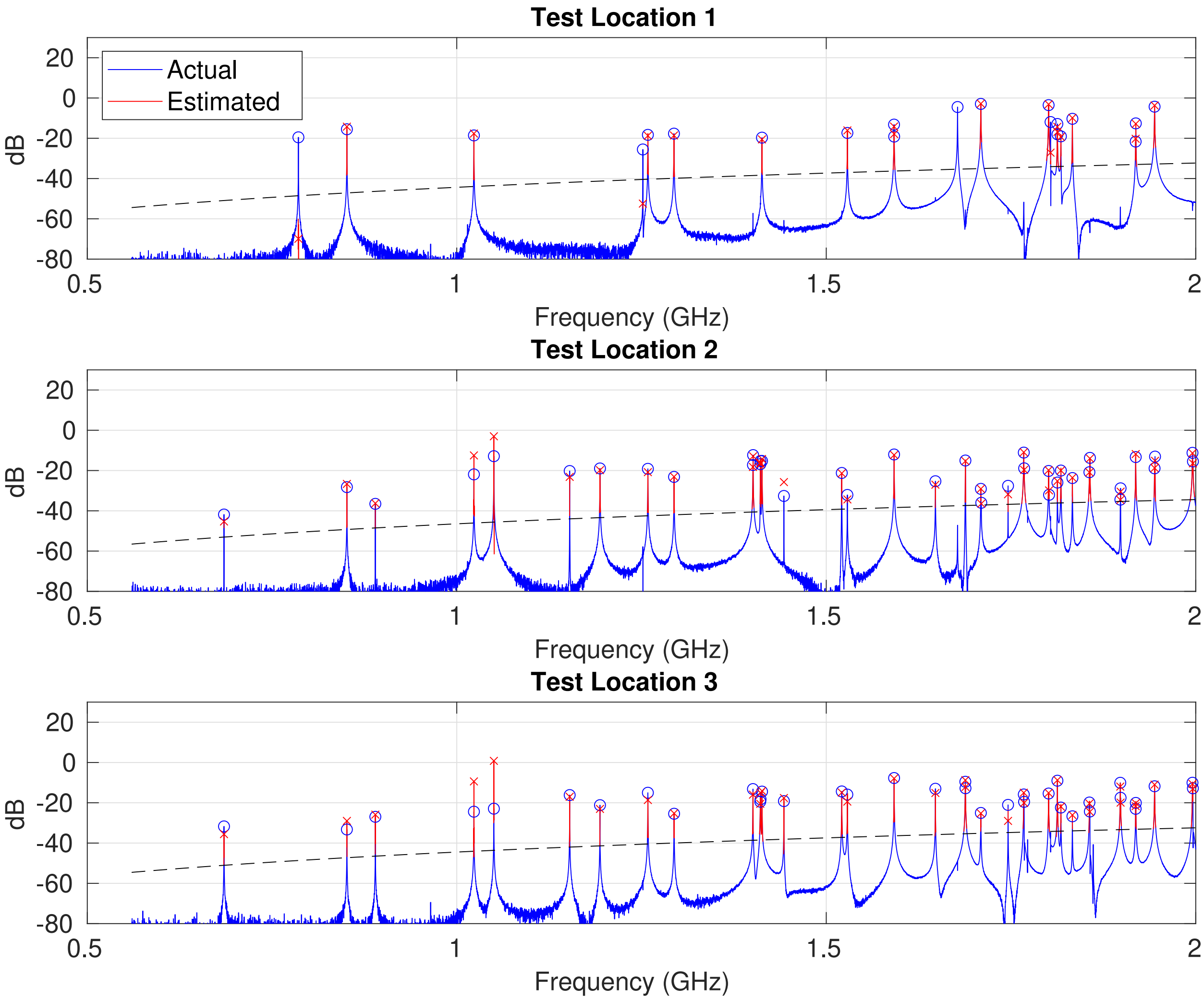

Test Port	P_{missed}	$\text{Error}_{90\%}$	$\text{Error}_{\text{Avg}}$
1	19.05 %	1.4 dB	0.8 dB
2	0.00 %	4.2 dB	1.6 dB
3	5.41 %	3.6 dB	1.5 dB

Figure E-7. Measured good random probe set in empty PV2 with four probes.

E.1.2.2. Good Random Probe Set (Simulated)

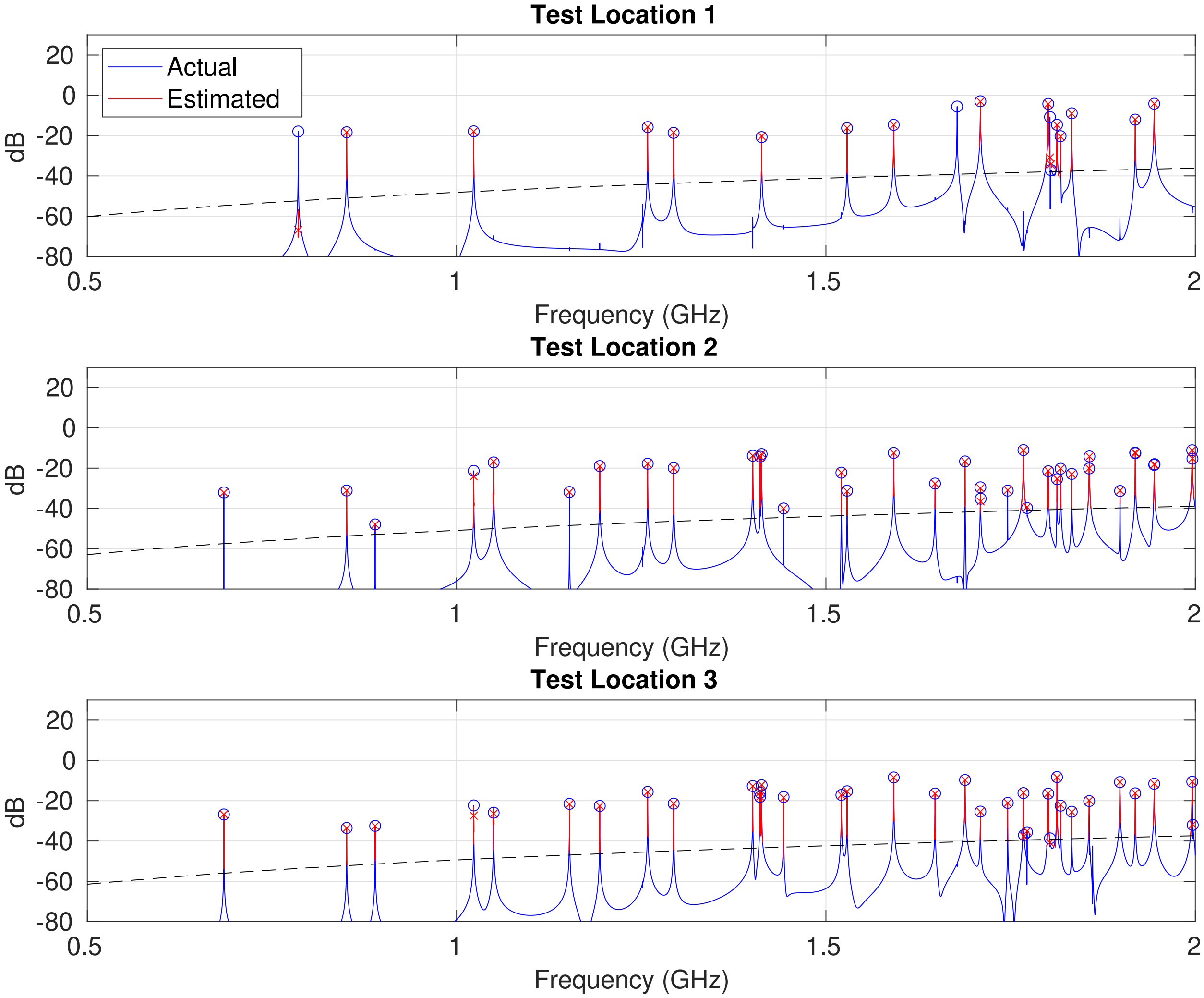

Test Port	P_{missed}	$\text{Error}_{90\%}$	$\text{Error}_{\text{Avg}}$
1	16.67 %	0.5 dB	0.3 dB
2	0.00 %	0.5 dB	0.2 dB
3	0.00 %	0.6 dB	0.4 dB

Figure E-8. Simulated good random probe set in empty PV2 with four probes.

E.1.2.3. Bad Random Probe Set (Measured)

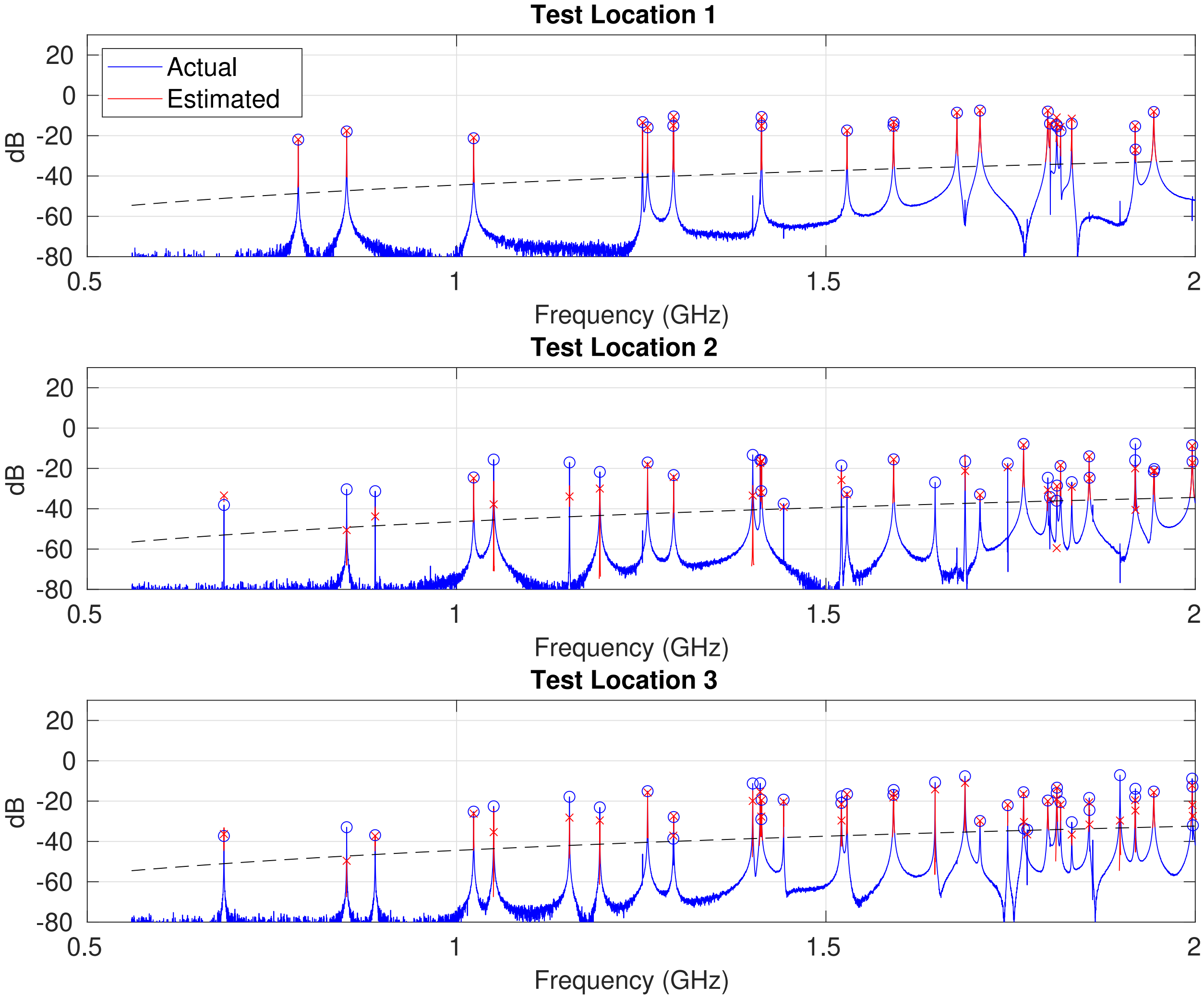

Test Port	P_{missed}	Error$_{90\%}$	Error$_{\text{Avg}}$
1	0.00 %	2.0 dB	0.6 dB
2	22.22 %	6.0 dB	1.8 dB
3	14.63 %	6.5 dB	2.4 dB

Figure E-9. Measured bad random probe set in empty PV2 with four probes.

E.1.2.4. Bad Random Probe Set (Simulated)

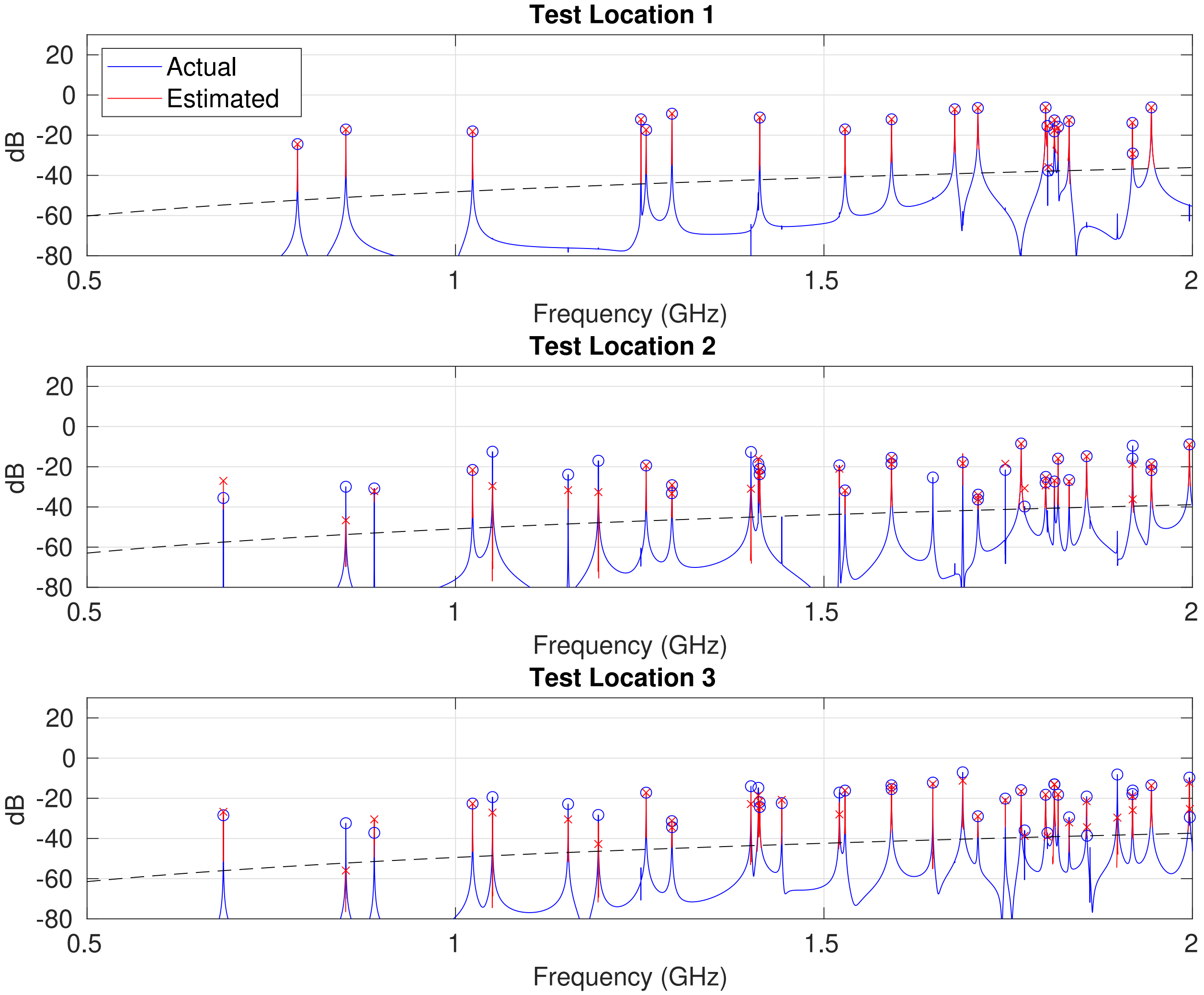

Test Port	P_{missed}	$\text{Error}_{90\%}$	$\text{Error}_{\text{Avg}}$
1	0.00 %	0.6 dB	0.2 dB
2	16.67 %	7.8 dB	1.4 dB
3	10.26 %	7.7 dB	2.2 dB

Figure E-10. Simulated bad random probe set in empty PV2 with four probes.

E.1.2.5. Heuristic Probe Set (Measured)

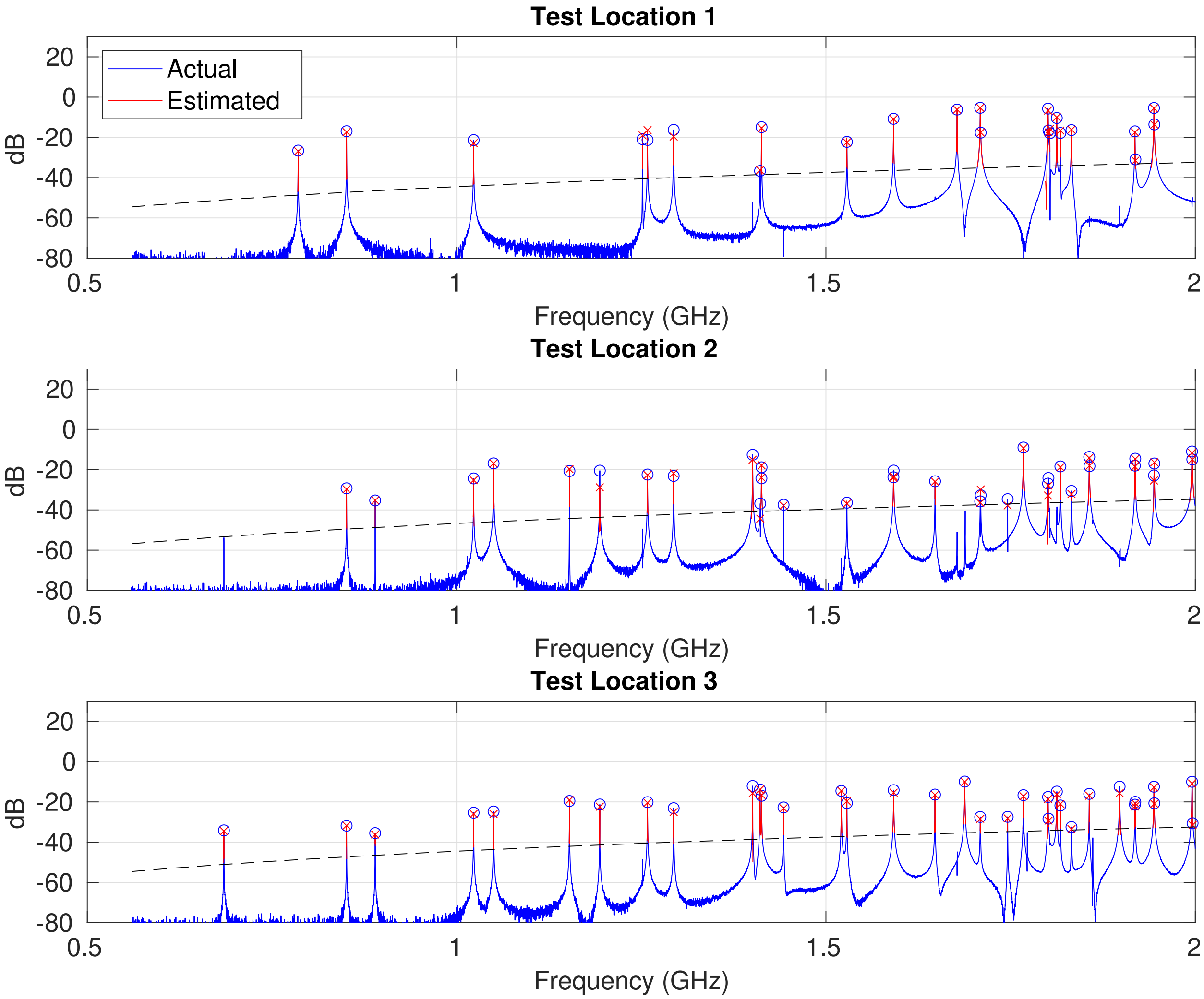

Test Port	P_{missed}	$\text{Error}_{90\%}$	$\text{Error}_{\text{Avg}}$
1	0.00 %	2.1 dB	0.9 dB
2	0.00 %	3.8 dB	1.6 dB
3	0.00 %	1.4 dB	0.9 dB

Figure E-11. Measured heuristic probe set in empty PV2 with four probes.

E.1.2.6. Heuristic Probe Set (Simulated)

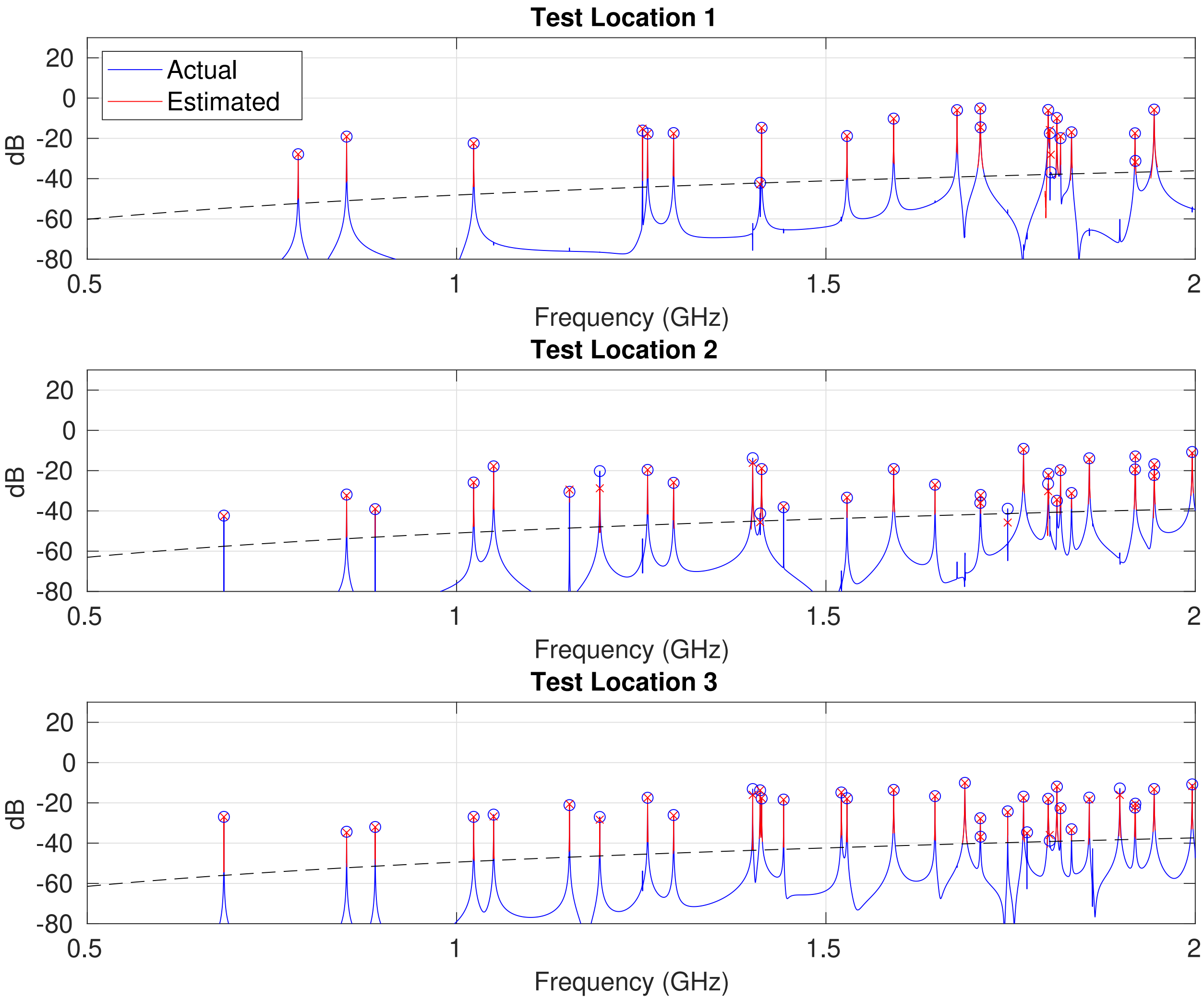

Test Port	P_{missed}	$\text{Error}_{90\%}$	$\text{Error}_{\text{Avg}}$
1	0.00 %	1.0 dB	0.7 dB
2	0.00 %	3.7 dB	1.1 dB
3	0.00 %	1.3 dB	0.5 dB

Figure E-12. Simulated heuristic probe set in empty PV2 with four probes.

E.2. Box in PV2 with Probe Injection

E.2.1. Six Probes

E.2.1.1. Good Random Probe Set (Measured)

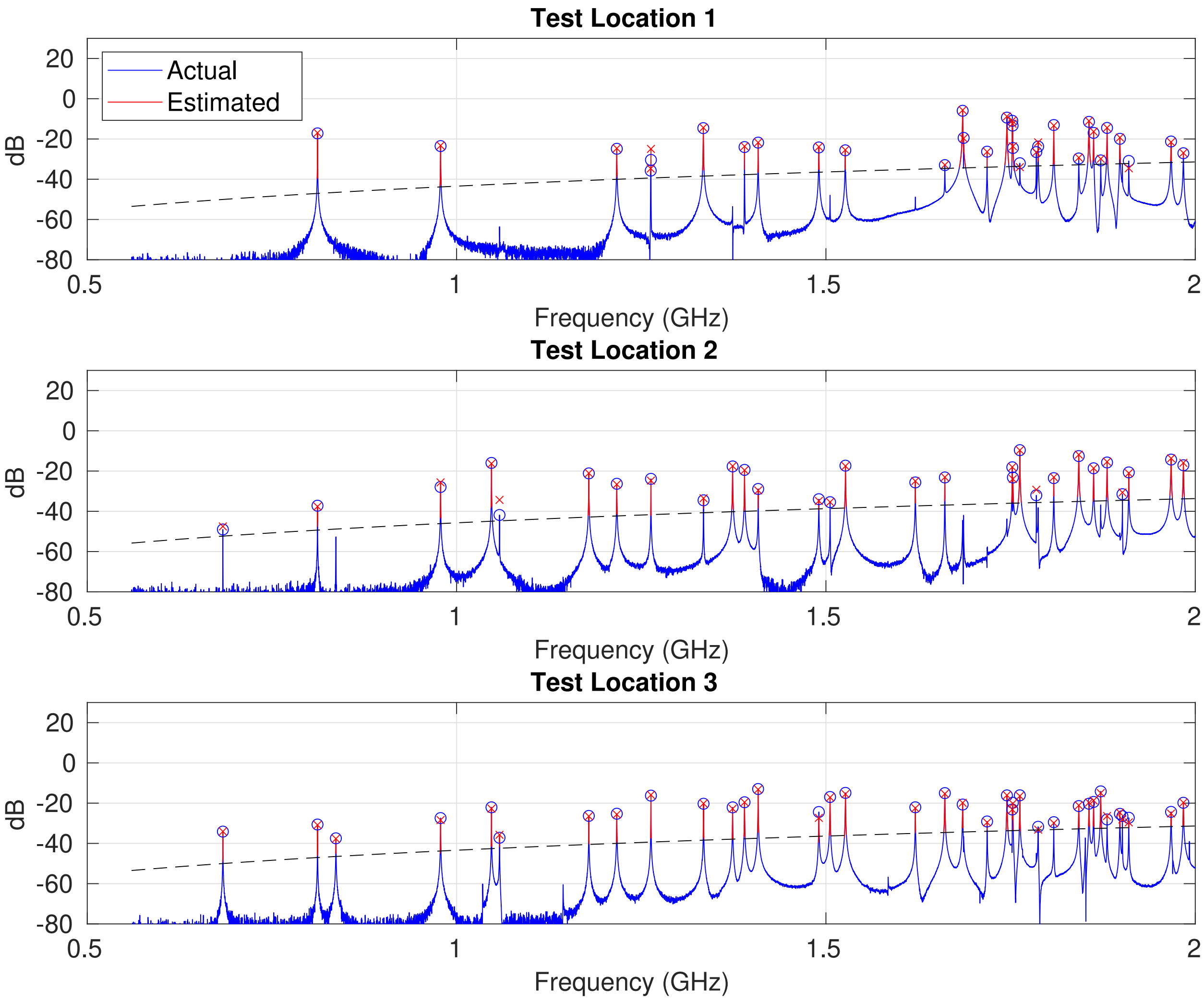

Test Port	P_{missed}	$\text{Error}_{90\%}$	$\text{Error}_{\text{Avg}}$
1	0.00 %	2.0 dB	0.7 dB
2	0.00 %	2.3 dB	0.9 dB
3	0.00 %	1.6 dB	0.7 dB

Figure E-13. Measured good random probe set in box-in-PV2 with six probes.

E.2.1.2. Good Random Probe Set (Simulated)

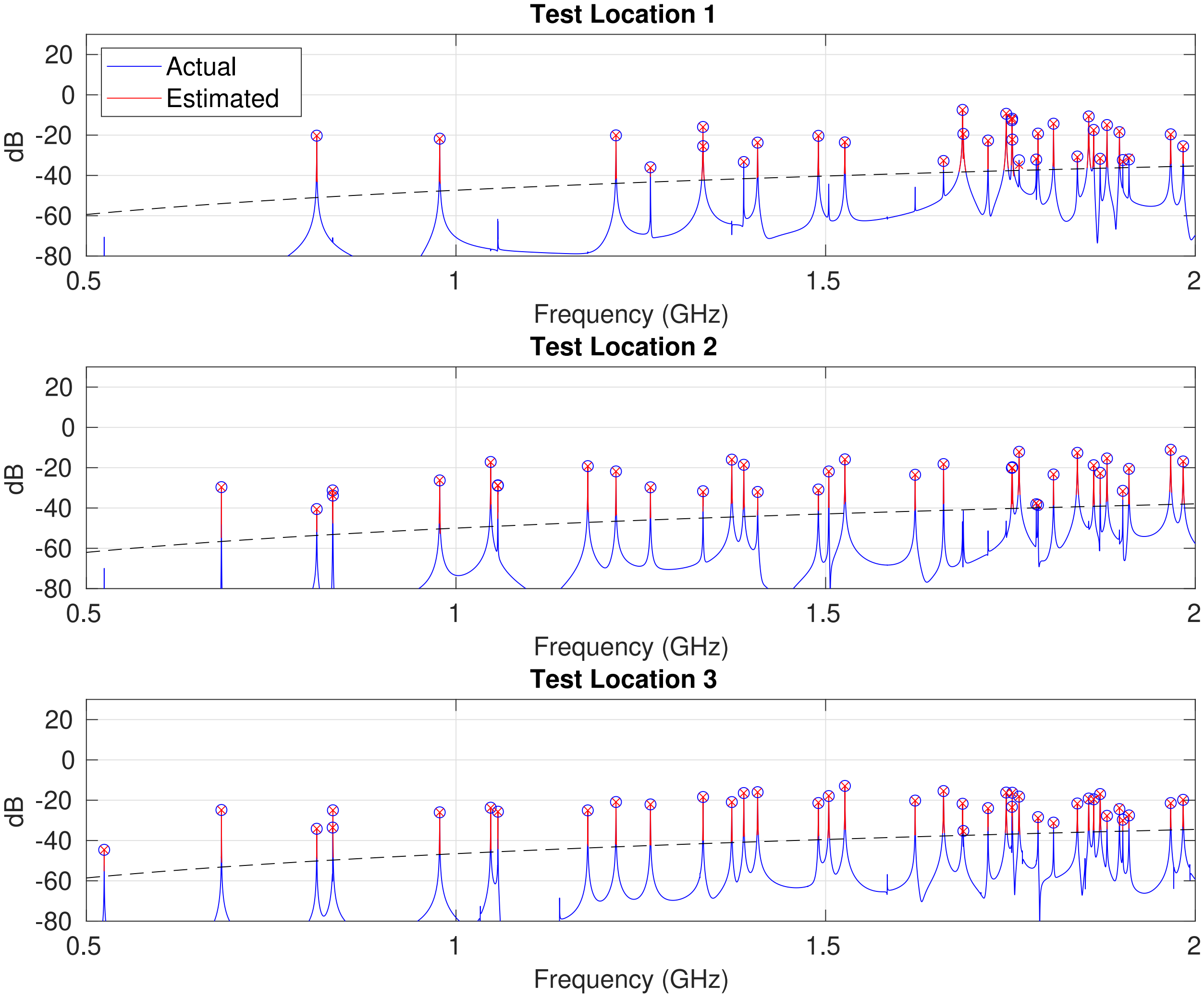

Test Port	P_{missed}	$\text{Error}_{90\%}$	$\text{Error}_{\text{Avg}}$
1	0.00 %	0.5 dB	0.2 dB
2	0.00 %	0.2 dB	0.1 dB
3	0.00 %	0.3 dB	0.1 dB

Figure E-14. Simulated good random probe set in box-in-PV2 with six probes.

E.2.1.3. Bad Random Probe Set (Measured)

This experiment was not performed.

E.2.1.4. Bad Random Probe Set (Simulated)

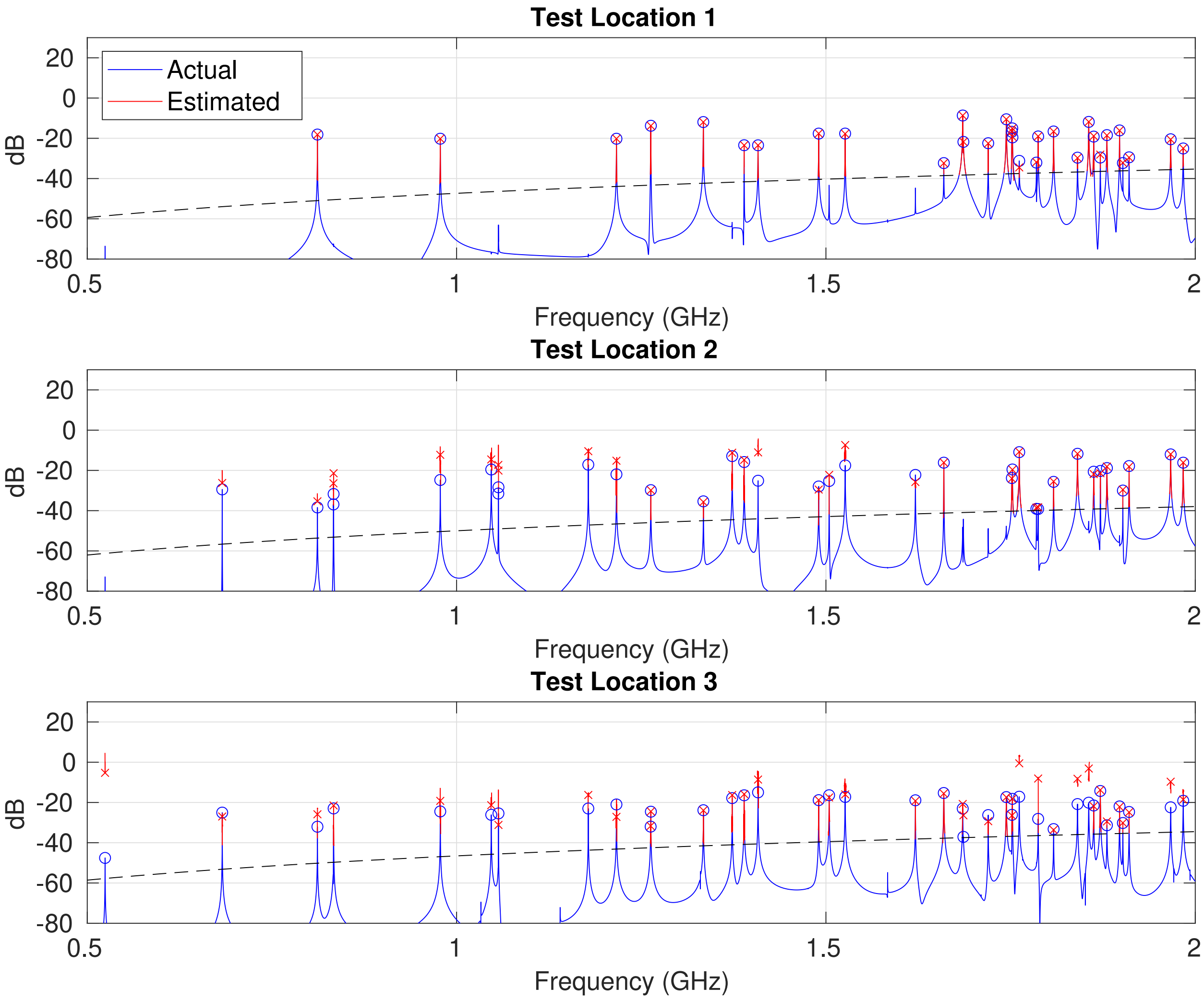

Test Port	P_{missed}	$\text{Error}_{90\%}$	$\text{Error}_{\text{Avg}}$
1	0.00 %	0.3 dB	0.2 dB
2	17.65 %	6.7 dB	1.8 dB
3	17.95 %	6.2 dB	1.9 dB

Figure E-15. Simulated bad random probe set in box-in-PV2 with six probes.

E.2.1.5. Heuristic Probe Set (Measured)

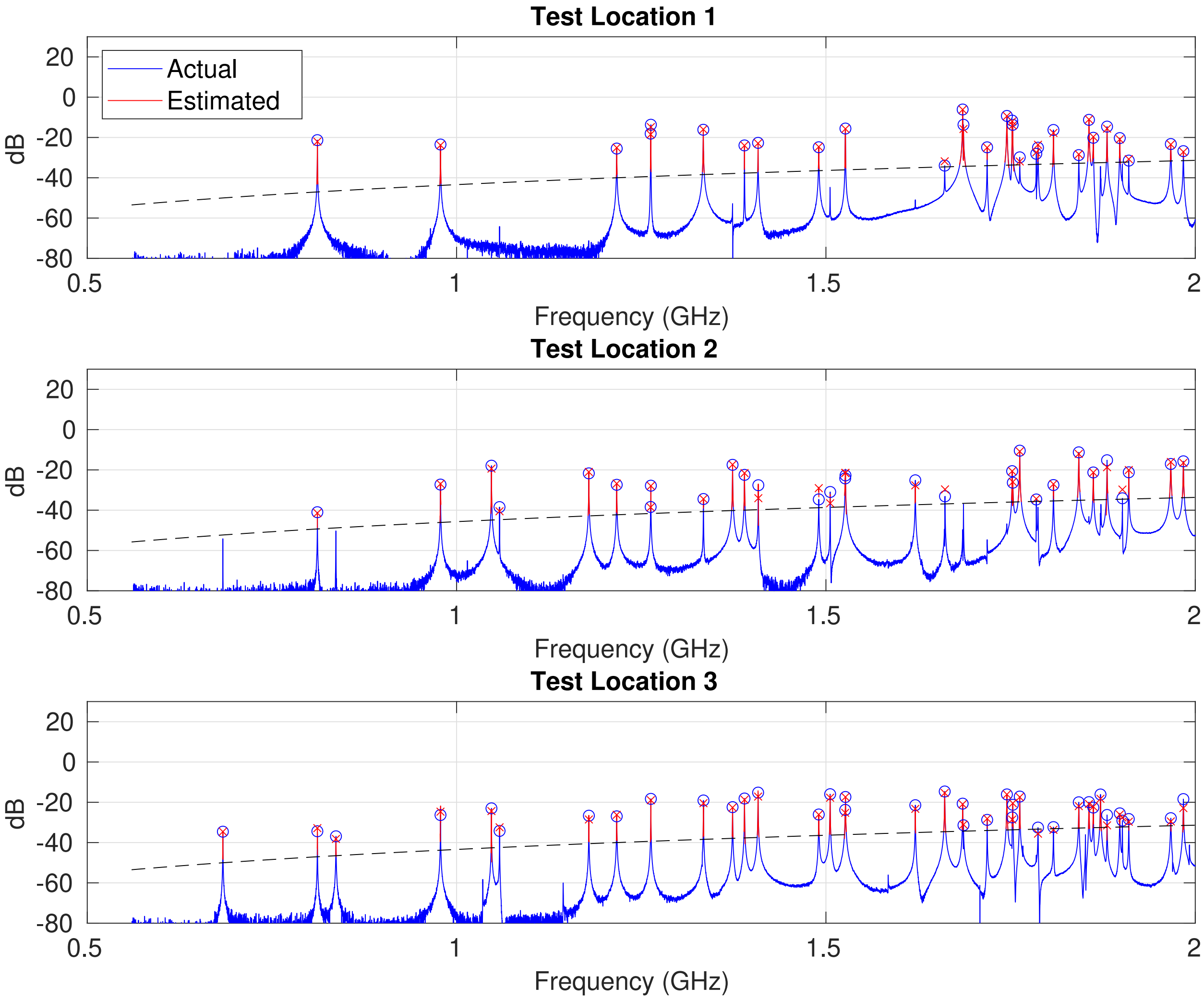

Test Port	P_{missed}	$\text{Error}_{90\%}$	$\text{Error}_{\text{Avg}}$
1	0.00 %	2.1 dB	0.6 dB
2	0.00 %	5.6 dB	1.6 dB
3	0.00 %	2.1 dB	1.3 dB

Figure E-16. Measured heuristic probe set in box-in-PV2 with six probes.

E.2.1.6. Heuristic Probe Set (Simulated)

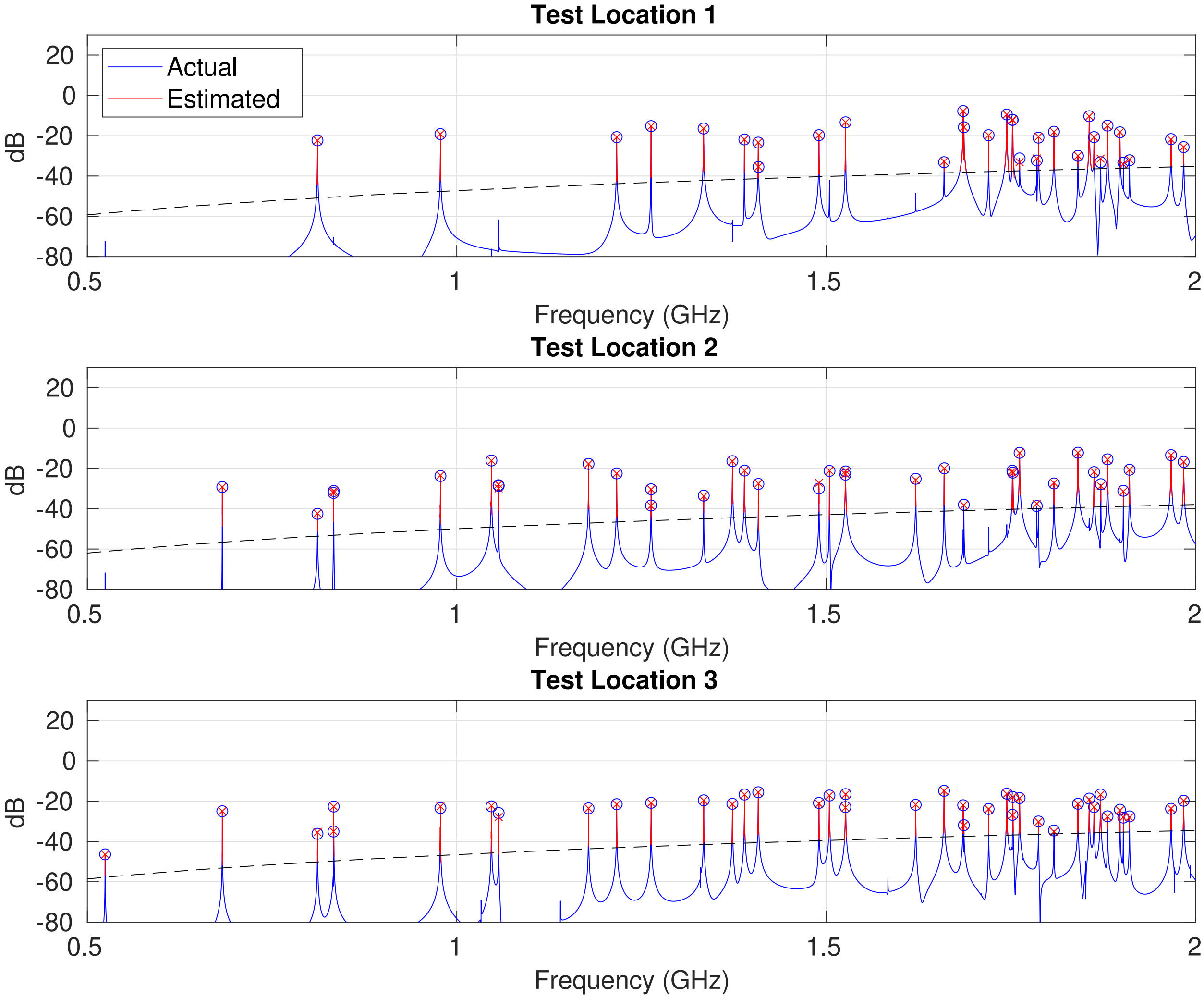

Test Port	P_{missed}	$\text{Error}_{90\%}$	$\text{Error}_{\text{Avg}}$
1	0.00 %	0.8 dB	0.2 dB
2	0.00 %	0.9 dB	0.3 dB
3	0.00 %	0.5 dB	0.2 dB

Figure E-17. Simulated heuristic probe set in box-in-PV2 with six probes.

E.2.2. Four Probes

E.2.2.1. Good Random Probe Set (Measured)

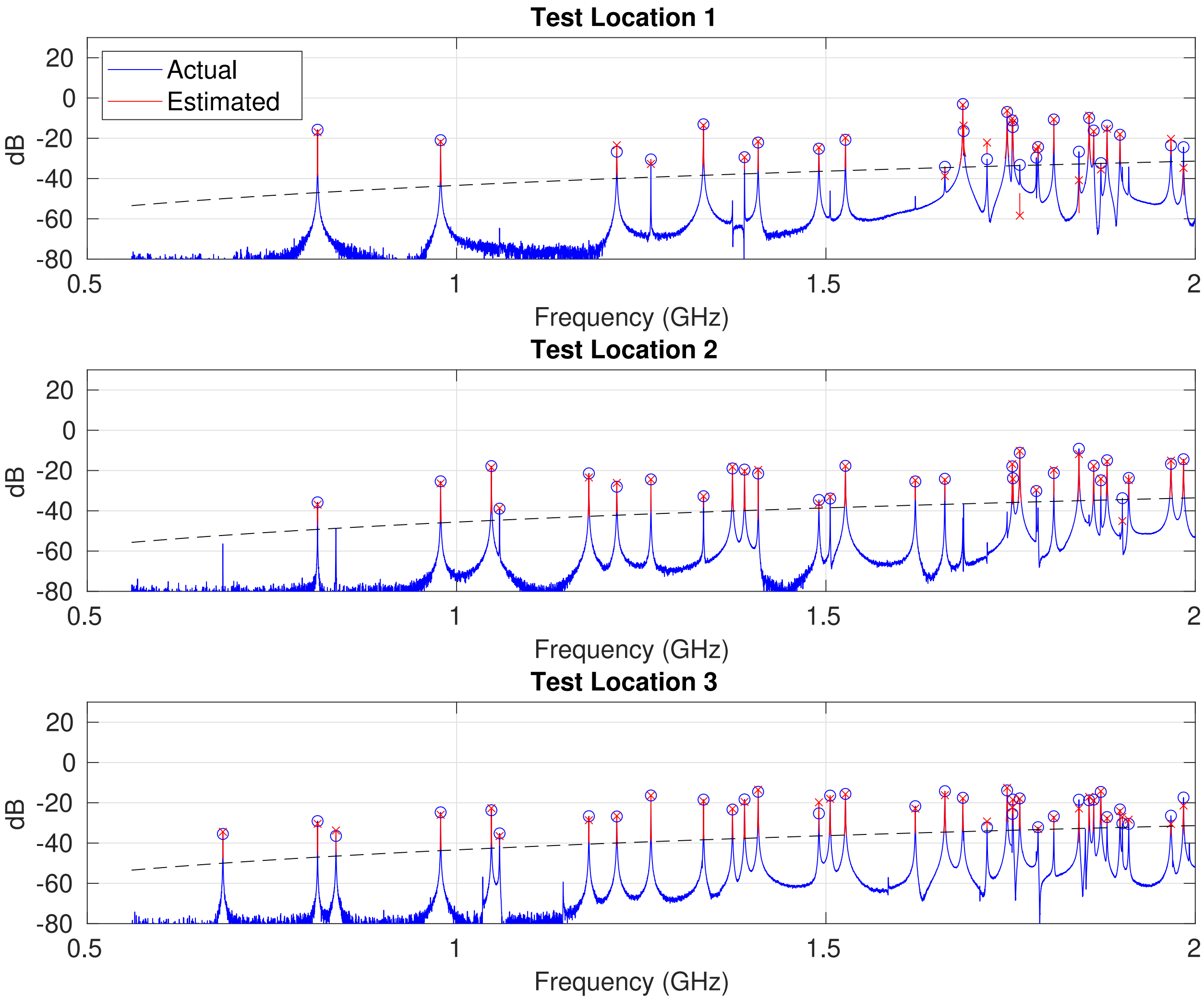
Test Location 1

Test Location 2

Test Location 3

Test Port	P_{missed}	$\text{Error}_{90\%}$	$\text{Error}_{\text{Avg}}$
1	10.71 %	4.0 dB	1.8 dB
2	3.45 %	1.9 dB	0.9 dB
3	0.00 %	4.0 dB	1.6 dB

Figure E-18. Measured good random probe set in box-in-PV2 with four probes.

E.2.2.2. Good Random Probe Set (Simulated)

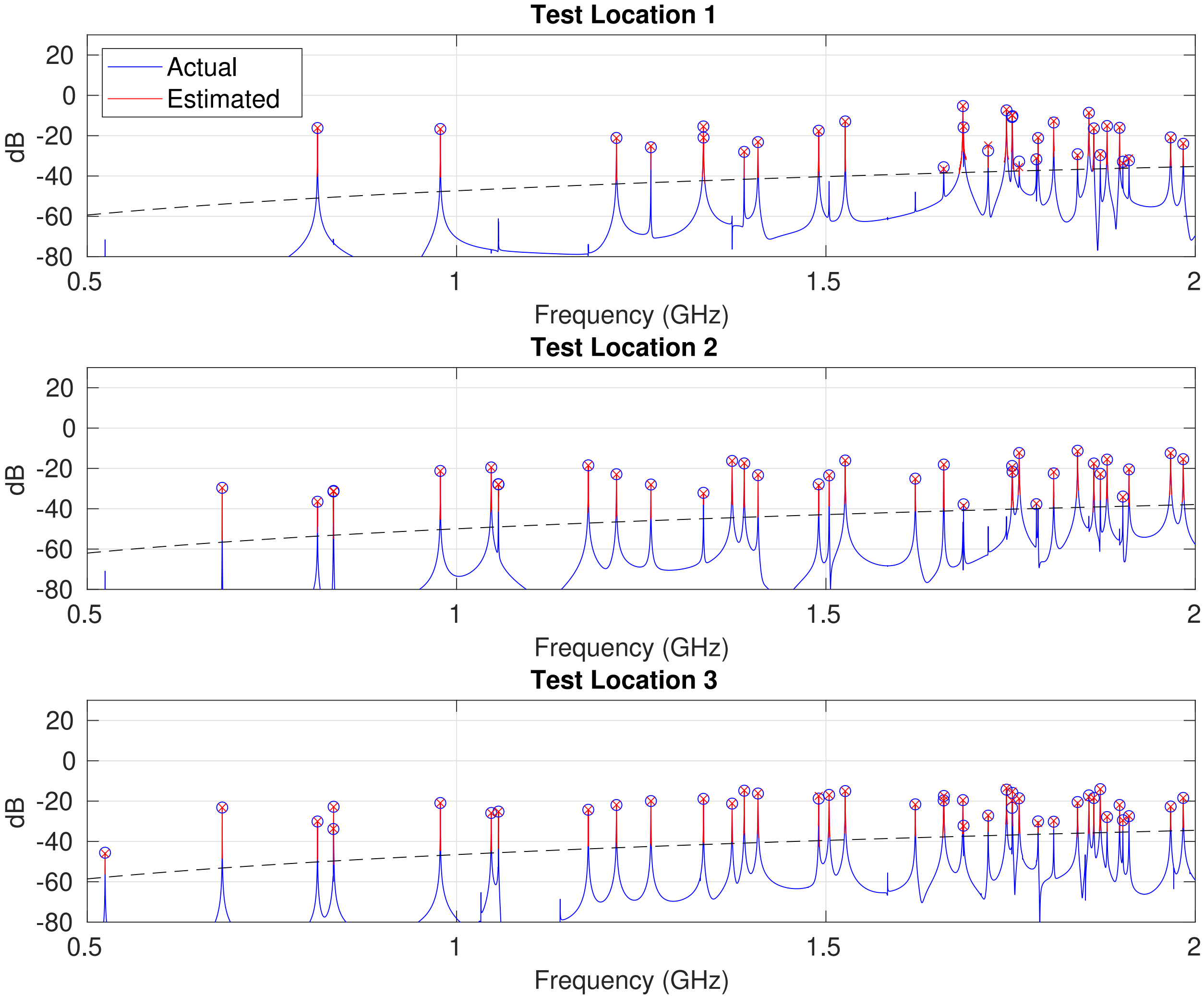

Test Port	P_{missed}	$\text{Error}_{90\%}$	$\text{Error}_{\text{Avg}}$
1	0.00 %	1.0 dB	0.5 dB
2	0.00 %	0.5 dB	0.2 dB
3	0.00 %	0.8 dB	0.3 dB

Figure E-19. Simulated good random probe set in box-in-PV2 with four probes.

E.2.2.3. Bad Random Probe Set (Measured)

This experiment was not performed.

E.2.2.4. Bad Random Probe Set (Simulated)

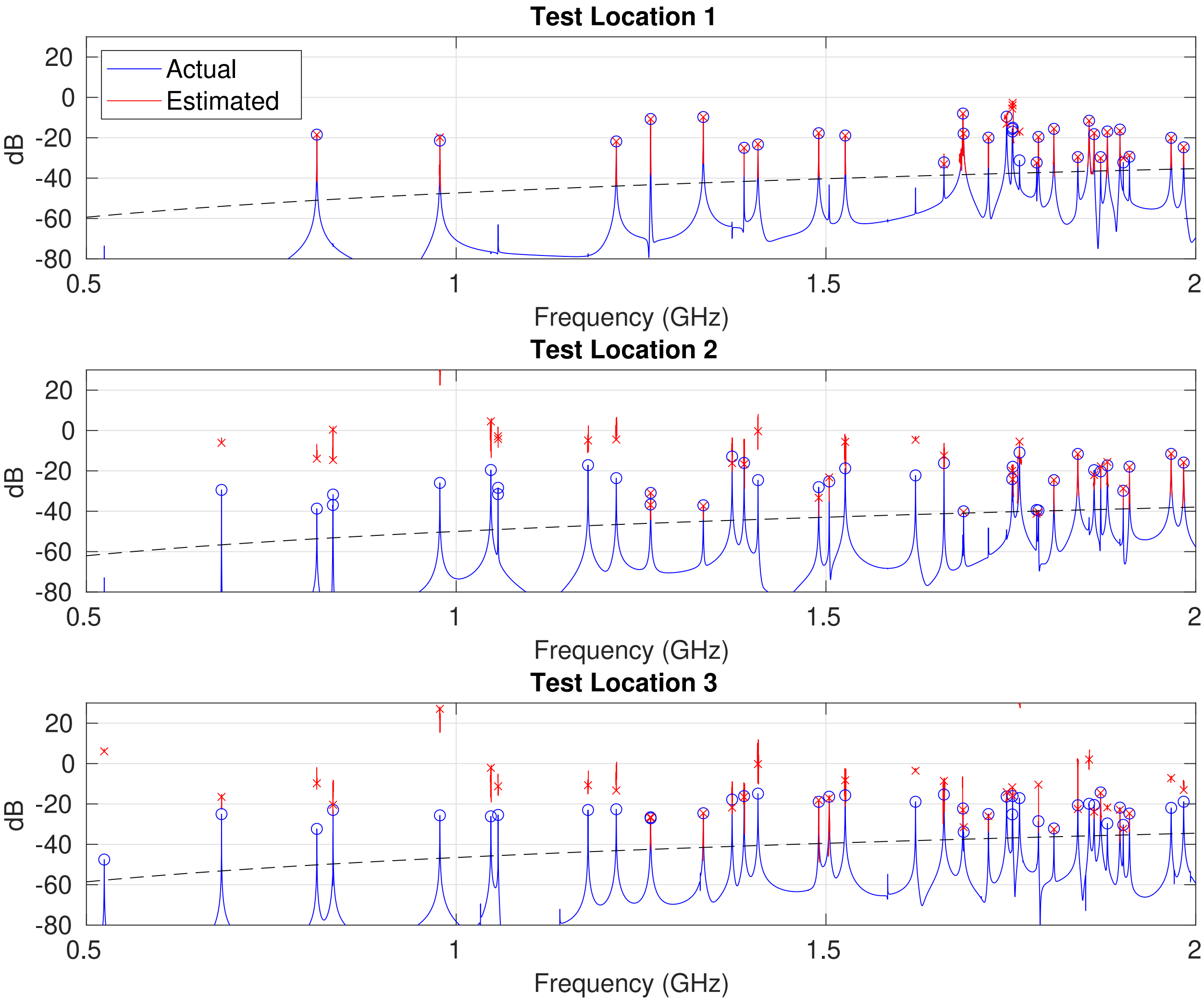

Test Port	P_{missed}	$\text{Error}_{90\%}$	$\text{Error}_{\text{Avg}}$
1	12.90 %	1.6 dB	0.4 dB
2	36.11 %	5.3 dB	1.9 dB
3	33.33 %	7.9 dB	2.7 dB

Figure E-20. Simulated bad random probe set in box-in-PV2 with four probes.

E.2.2.5. Heuristic Probe Set (Measured)

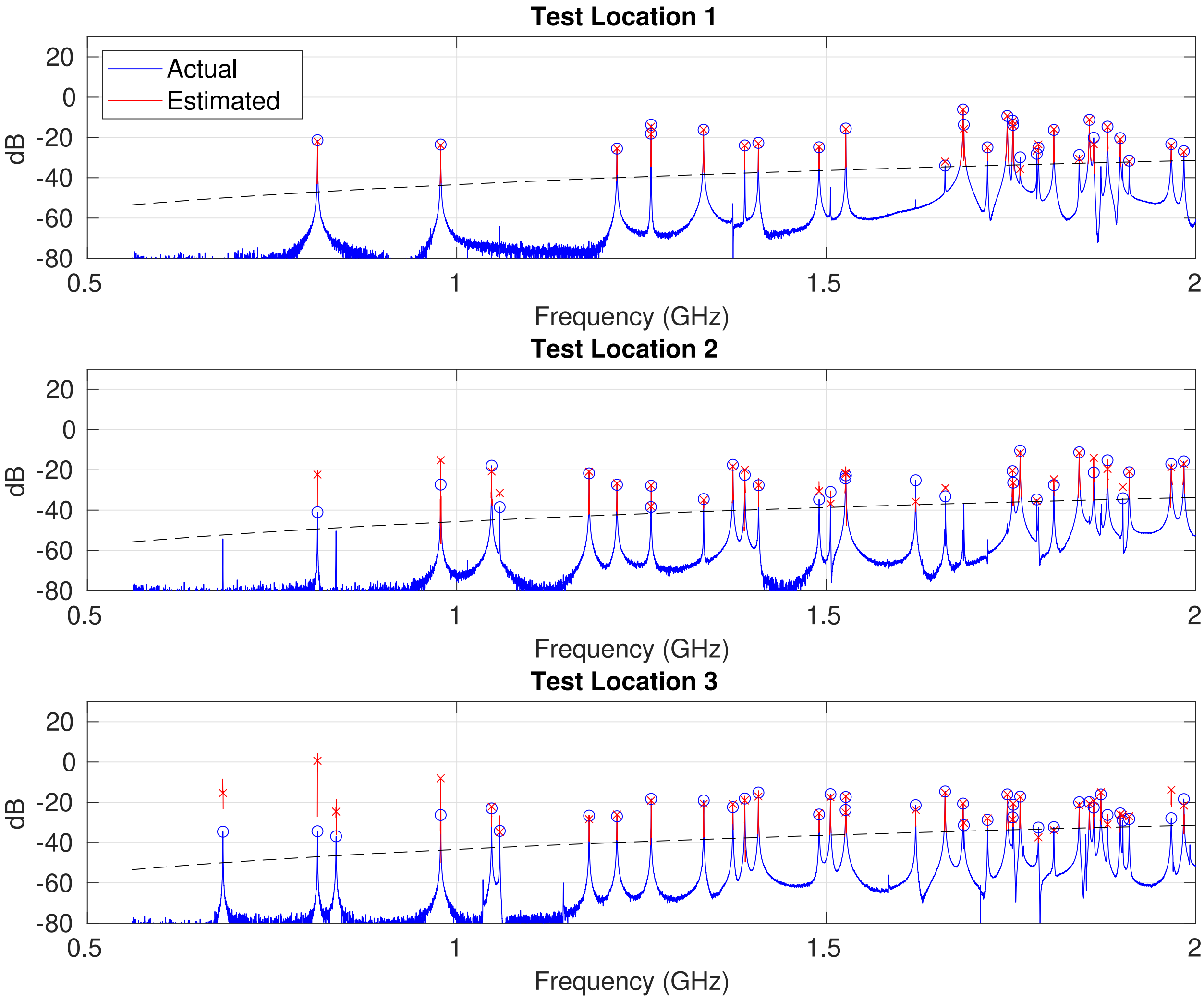

Test Port	P_{missed}	Error$_{90\%}$	Error$_{\text{Avg}}$
1	0.00 %	2.2 dB	0.9 dB
2	10.00 %	5.8 dB	2.2 dB
3	13.16 %	3.2 dB	1.4 dB

Figure E-21. Measured heuristic probe set in box-in-PV2 with four probes.

E.2.2.6. Heuristic Probe Set (Simulated)

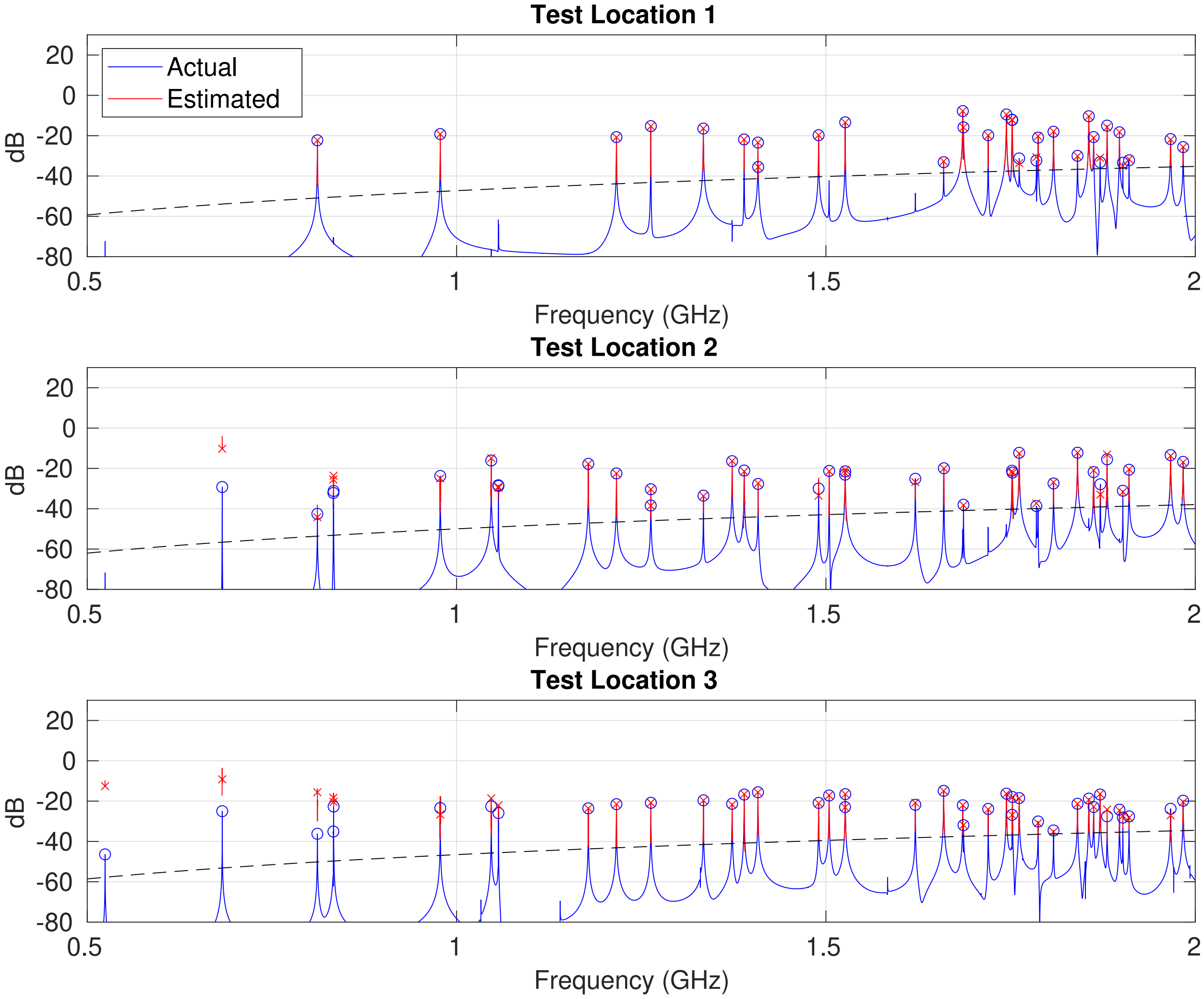

Test Port	P_{missed}	$\text{Error}_{90\%}$	$\text{Error}_{\text{Avg}}$
1	0.00 %	1.6 dB	0.4 dB
2	2.78 %	3.6 dB	1.2 dB
3	10.00 %	3.2 dB	0.8 dB

Figure E-22. Simulated heuristic probe set in box-in-PV2 with four probes.

E.3. Box in PV2 with Slot Excitation

E.3.1. Six Probes

E.3.1.1. Good Random Probe Set (Measured)

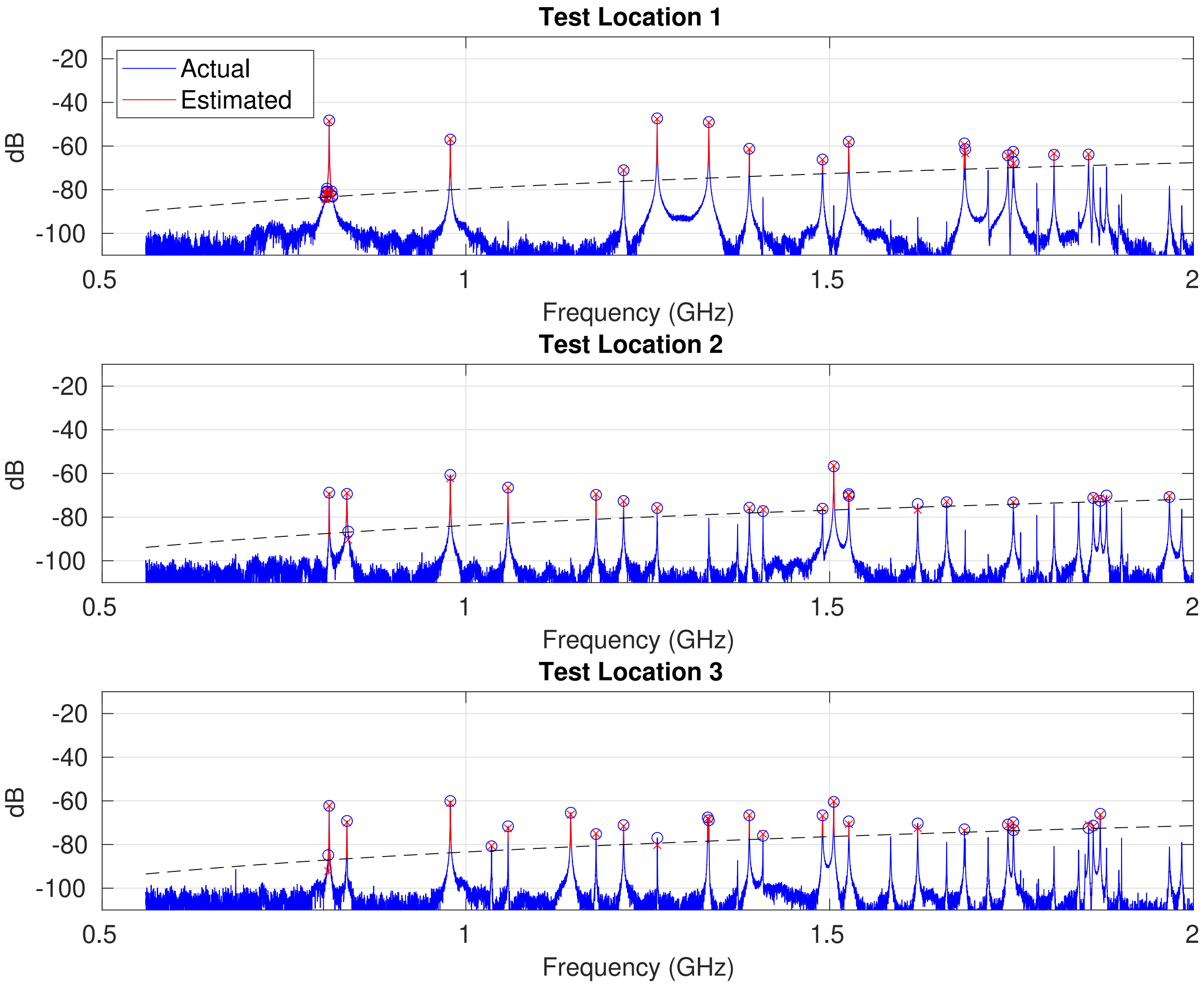

Location	P_{missed}	$\text{Error}_{90\%}$	$\text{Error}_{\text{avg}}$
1	0.00 %	1.1 dB	0.5 dB
2	0.00 %	1.8 dB	0.8 dB
3	0.00 %	2.1 dB	1.0 dB

Figure E-23. Measured good random probe set in box-in-PV2 with six probes.

E.3.1.2. Good Random Probe Set (Simulated)

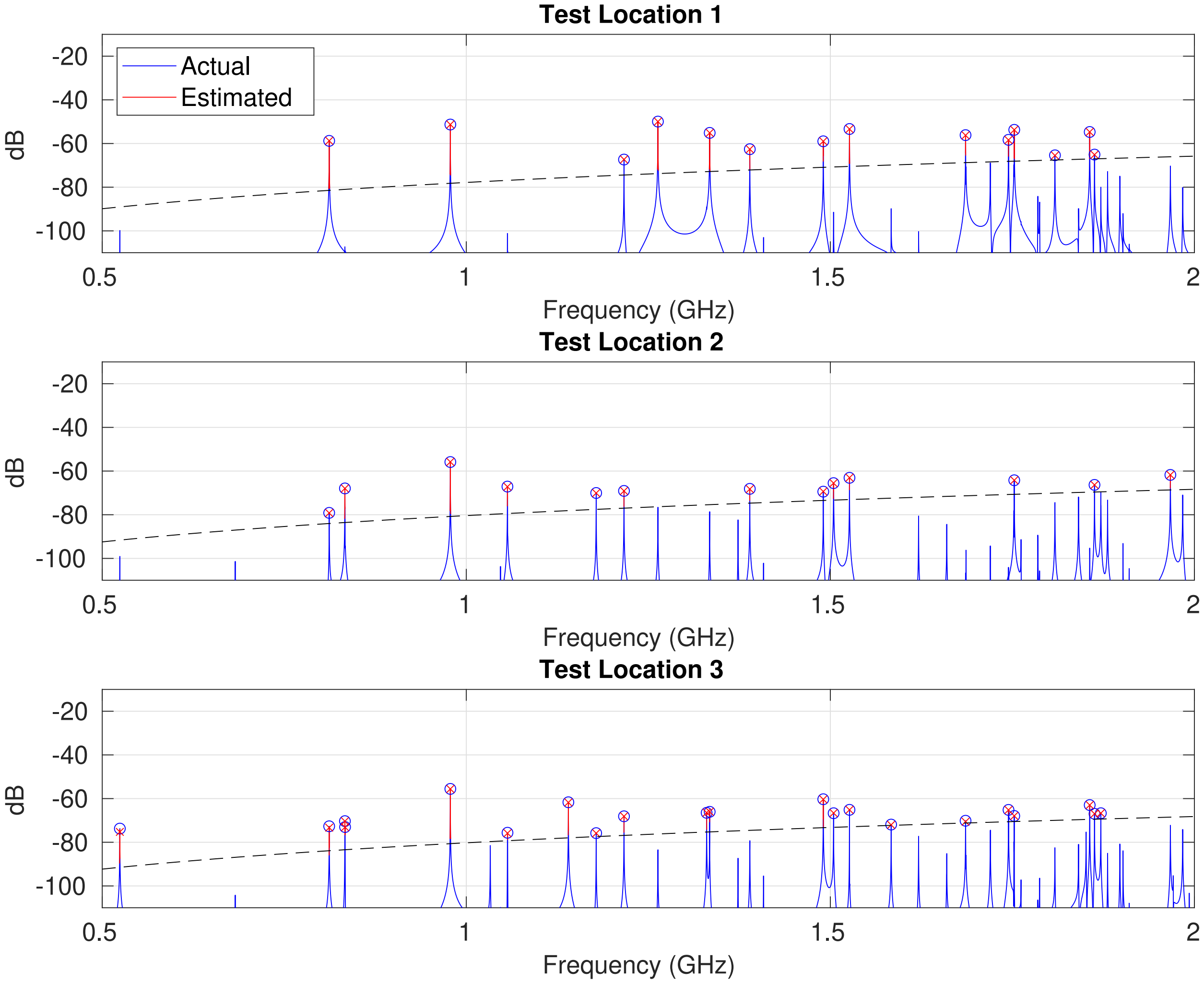

Location	P_{missed}	$\text{Error}_{90\%}$	$\text{Error}_{\text{avg}}$
1	0.00 %	0.1 dB	0.0 dB
2	0.00 %	0.1 dB	0.0 dB
3	0.00 %	0.4 dB	0.2 dB

Figure E-24. Simulated good random probe set in box-in-PV2 with six probes.

E.3.1.3. Bad Random Probe Set (Measured)

This experiment was not performed.

E.3.1.4. Bad Random Probe Set (Simulated)

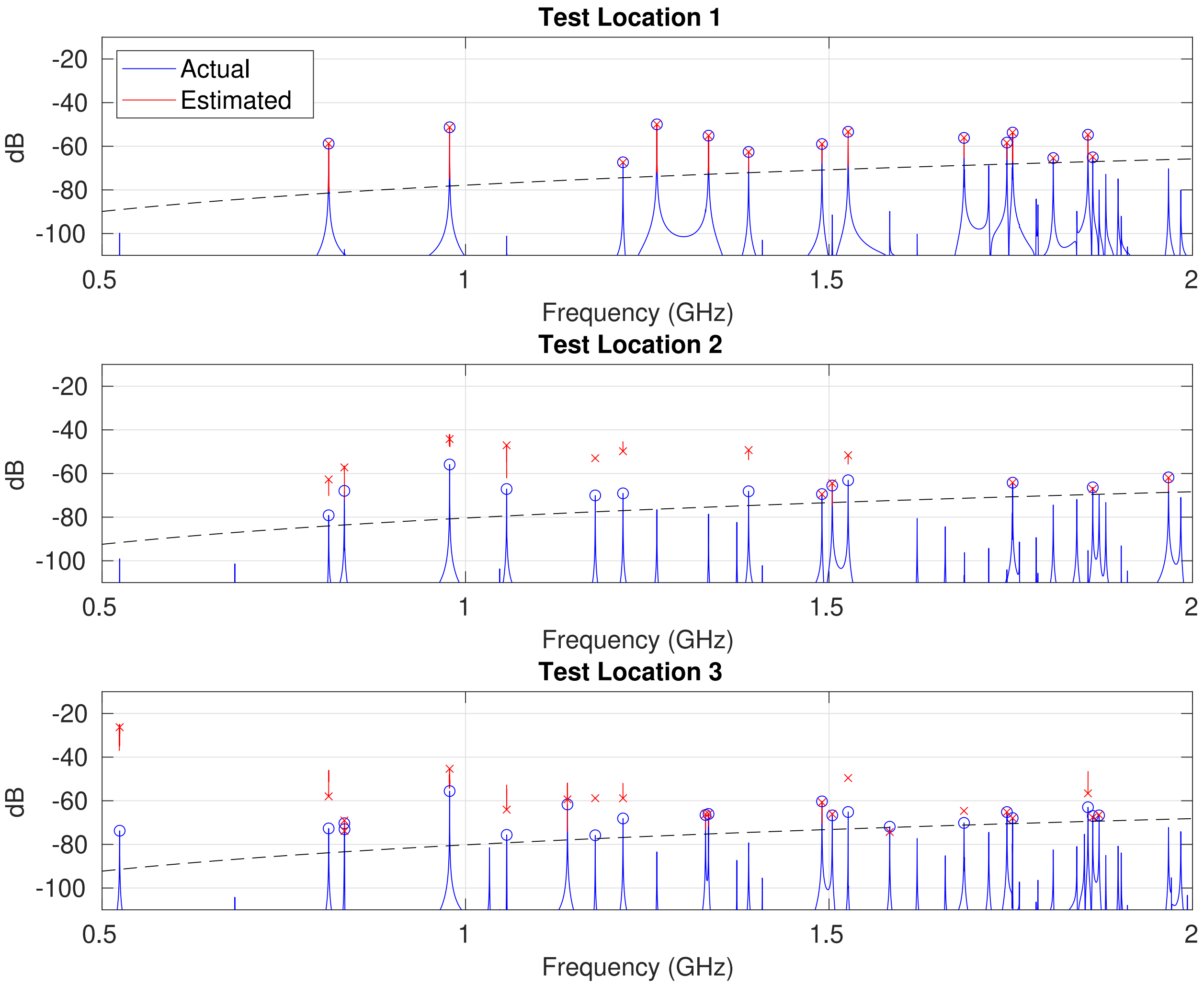

Location	P_{missed}	$\text{Error}_{90\%}$	$\text{Error}_{\text{avg}}$
1	0.00 %	0.1 dB	0.0 dB
2	61.54 %	1.1 dB	0.4 dB
3	28.57 %	6.3 dB	2.0 dB

Figure E-25. Simulated bad random probe set in box-in-PV2 with six probes.

E.3.1.5. Heuristic Probe Set (Measured)

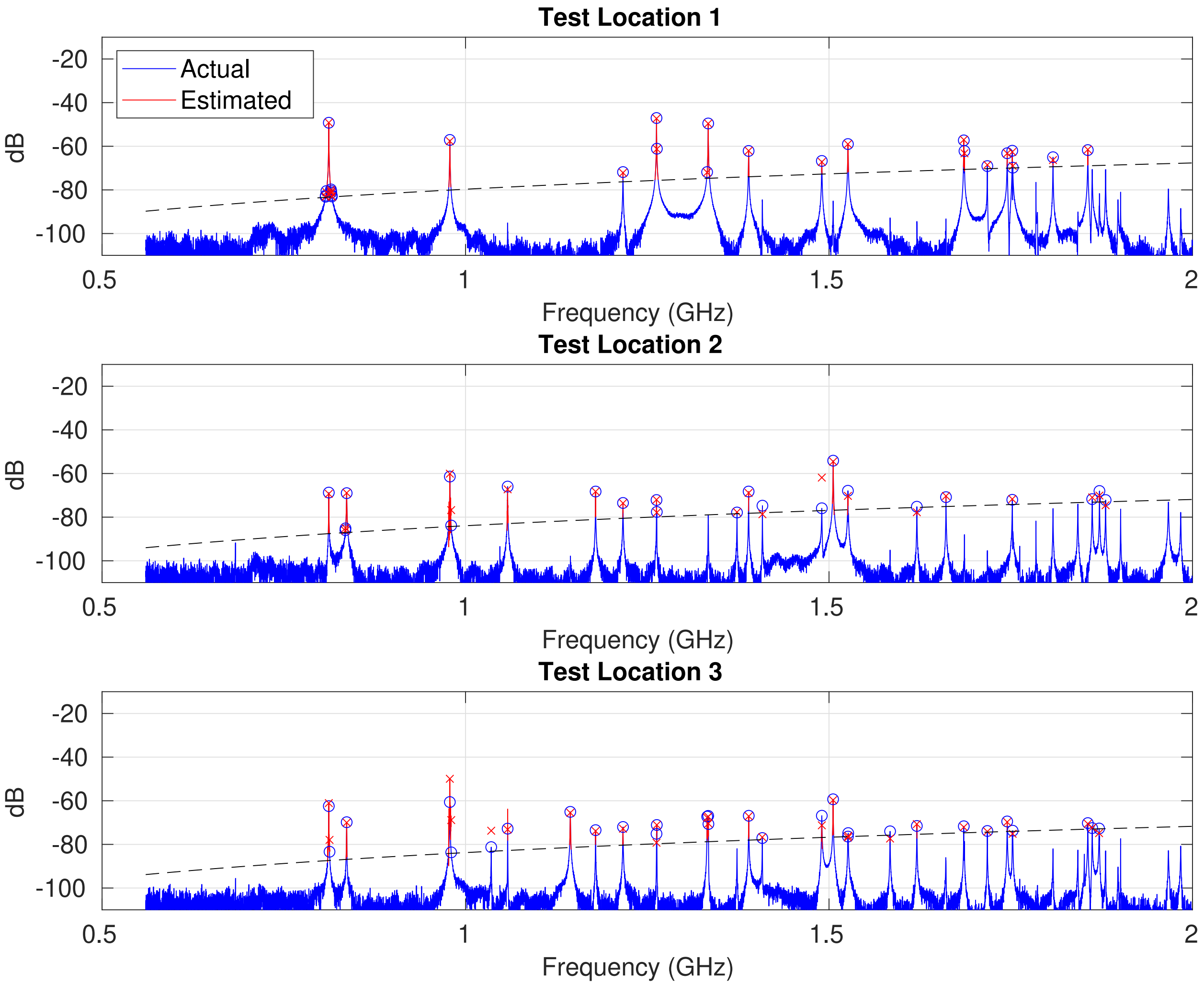

Location	P_{missed}	$\text{Error}_{90\%}$	$\text{Error}_{\text{avg}}$
1	0.00 %	0.8 dB	0.4 dB
2	4.35 %	2.5 dB	1.2 dB
3	6.67 %	4.4 dB	1.4 dB

Figure E-26. Measured heuristic probe set in box-in-PV2 with six probes.

E.3.1.6. Heuristic Probe Set (Simulated)

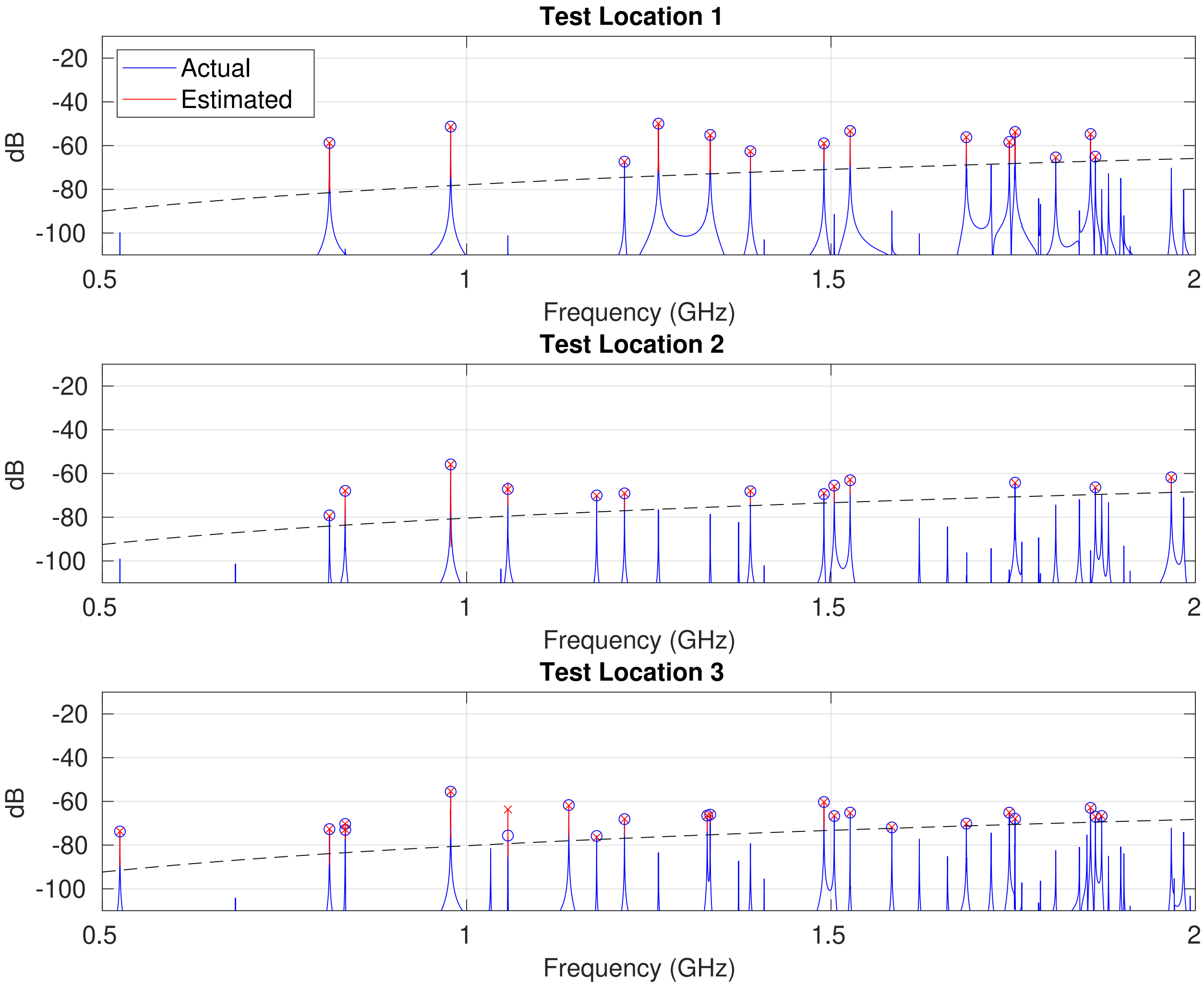

Location	P_{missed}	$\text{Error}_{90\%}$	$\text{Error}_{\text{avg}}$
1	0.00 %	0.1 dB	0.0 dB
2	0.00 %	0.4 dB	0.2 dB
3	4.76 %	0.2 dB	0.1 dB

Figure E-27. Simulated heuristic probe set in box-in-PV2 with six probes.

E.3.1.7. OED Probe Set (Measured)

This experiment was not performed.

E.3.1.8. OED Probe Set (Simulated)

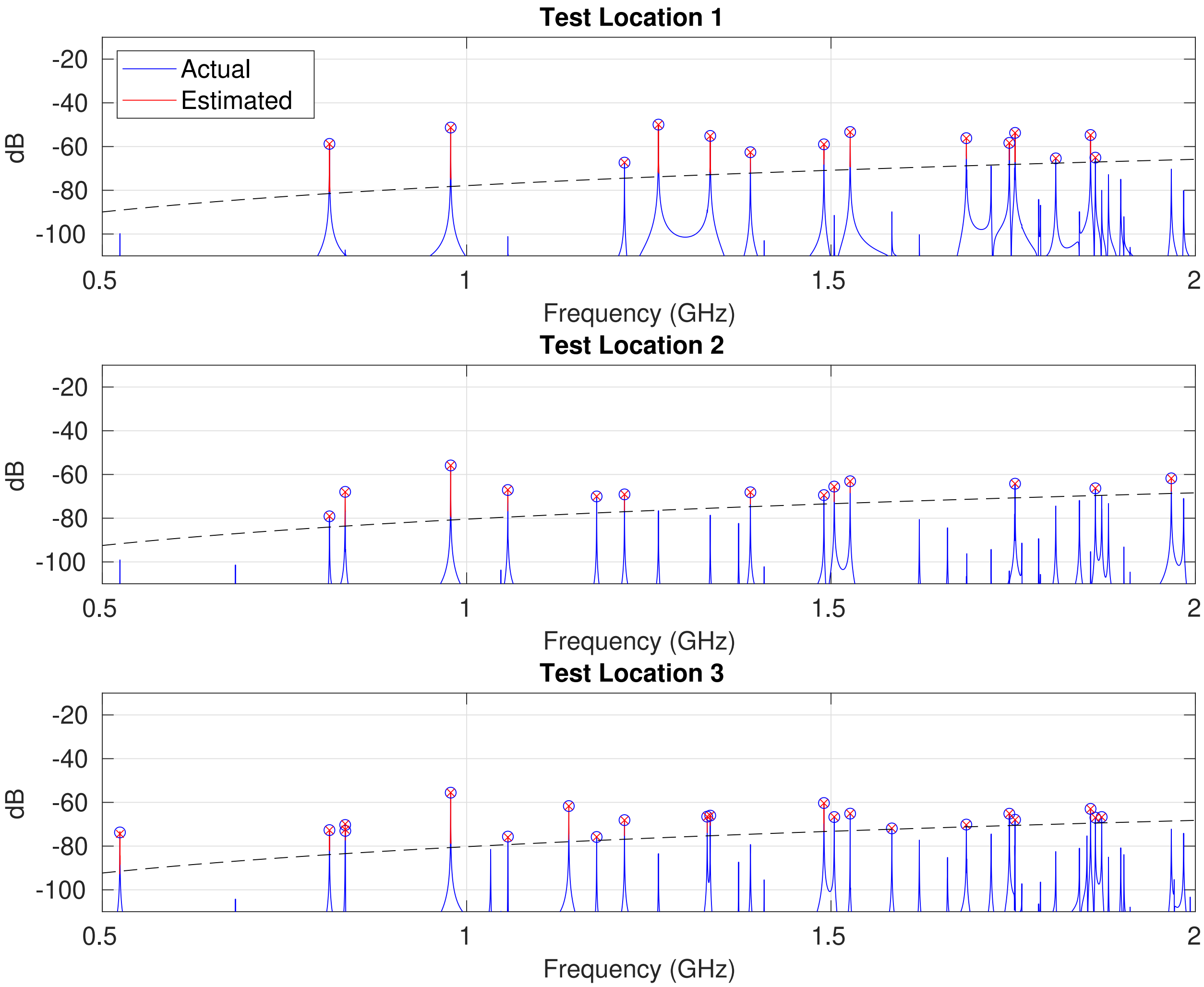

Location	P_{missed}	$\text{Error}_{90\%}$	$\text{Error}_{\text{avg}}$
1	0.00 %	0.1 dB	0.0 dB
2	0.00 %	0.1 dB	0.0 dB
3	0.00 %	0.5 dB	0.1 dB

Figure E-28. Simulated OED probe set in box-in-PV2 with six probes.

E.3.2. Four Probes

E.3.2.1. Good Random Probe Set (Measured)

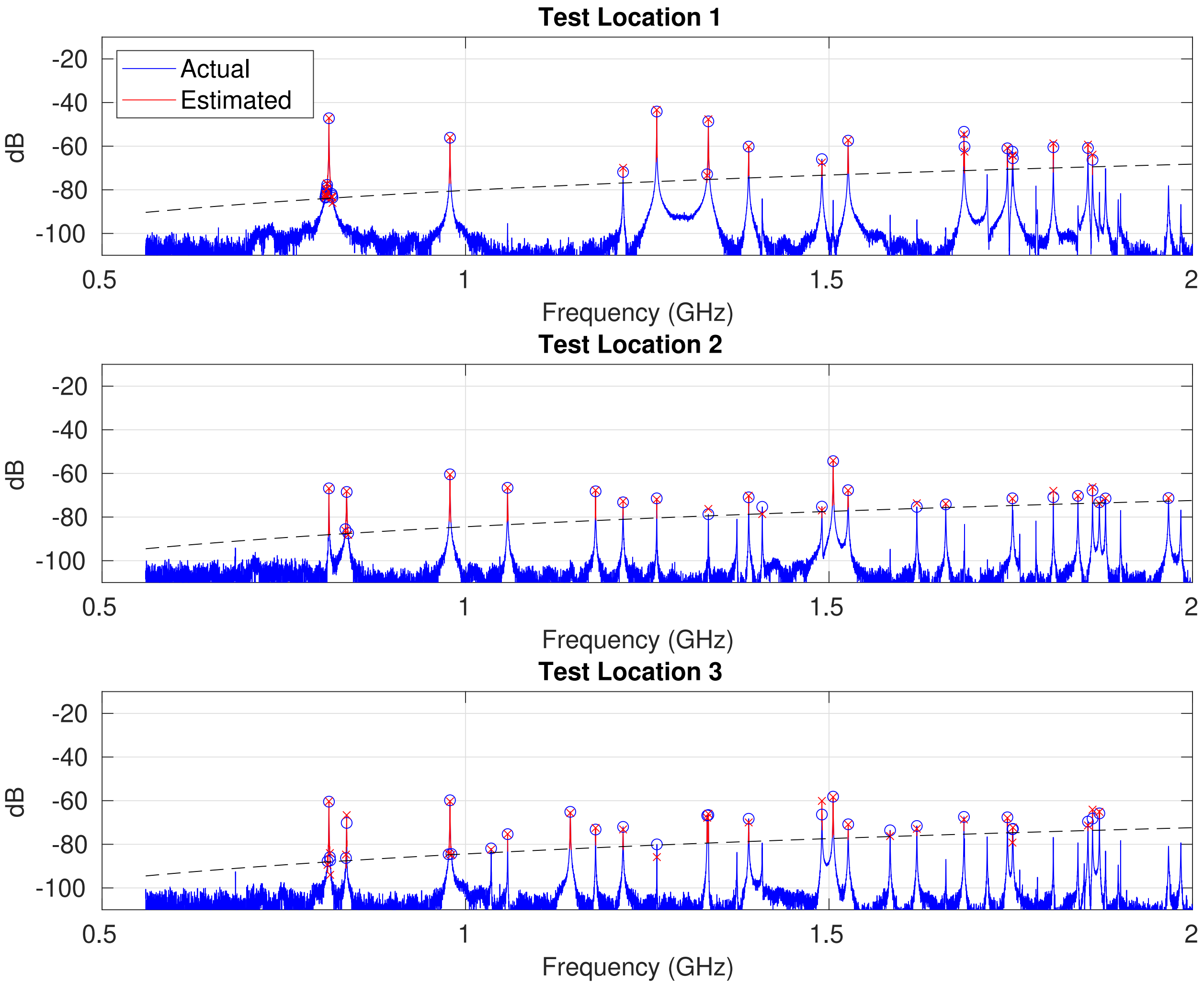

Location	P_{missed}	$\text{Error}_{90\%}$	$\text{Error}_{\text{avg}}$
1	0.00 %	2.2 dB	1.1 dB
2	0.00 %	2.4 dB	0.8 dB
3	0.00 %	6.2 dB	1.8 dB

Figure E-29. Measured good random probe set in box-in-PV2 with four probes.

E.3.2.2. Good Random Probe Set (Simulated)

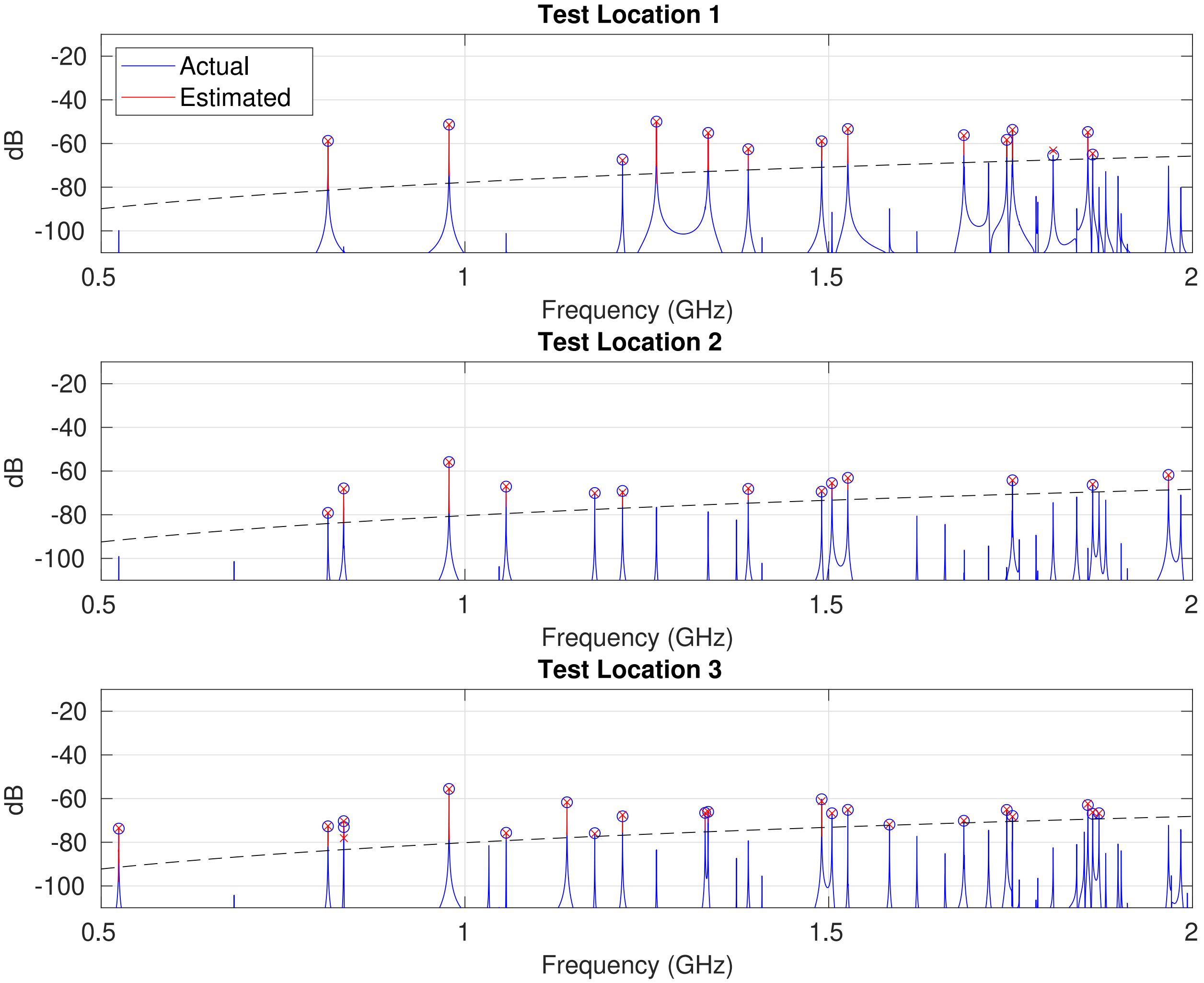

Location	P_{missed}	$\text{Error}_{90\%}$	$\text{Error}_{\text{avg}}$
1	0.00 %	0.5 dB	0.3 dB
2	0.00 %	0.4 dB	0.2 dB
3	0.00 %	0.8 dB	0.5 dB

Figure E-30. Simulated good random probe set in box-in-PV2 with four probes.

E.3.2.3. Bad Random Probe Set (Measured)

This experiment was not performed.

E.3.2.4. Bad Random Probe Set (Simulated)

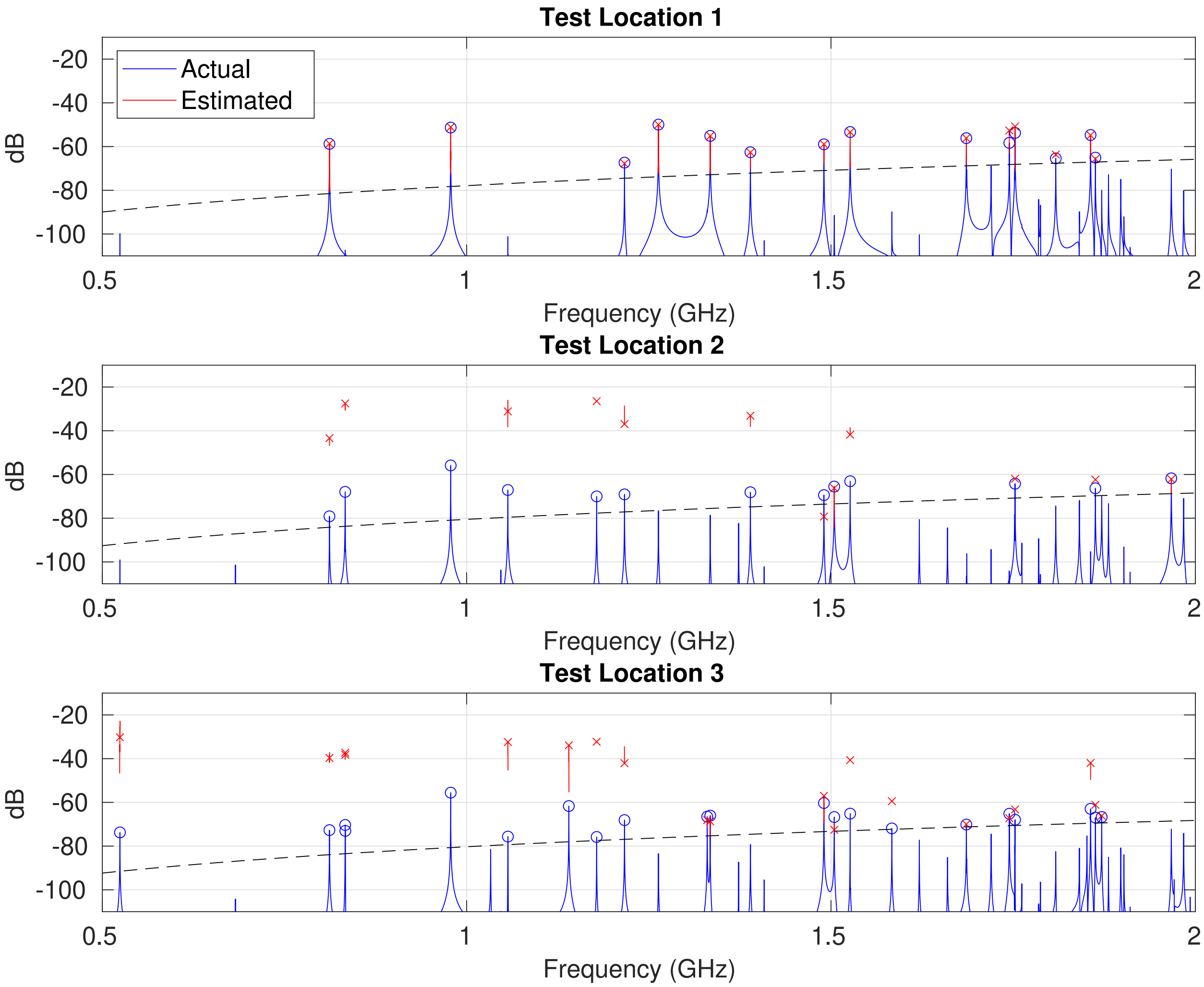

Location	P_{missed}	$\text{Error}_{90\%}$	$\text{Error}_{\text{avg}}$
1	0.00 %	2.9 dB	0.9 dB
2	61.54 %	9.8 dB	3.4 dB
3	57.14 %	5.8 dB	3.0 dB

Figure E-31. Simulated bad random probe set in box-in-PV2 with four probes.

E.3.2.5. Heuristic Probe Set (Measured)

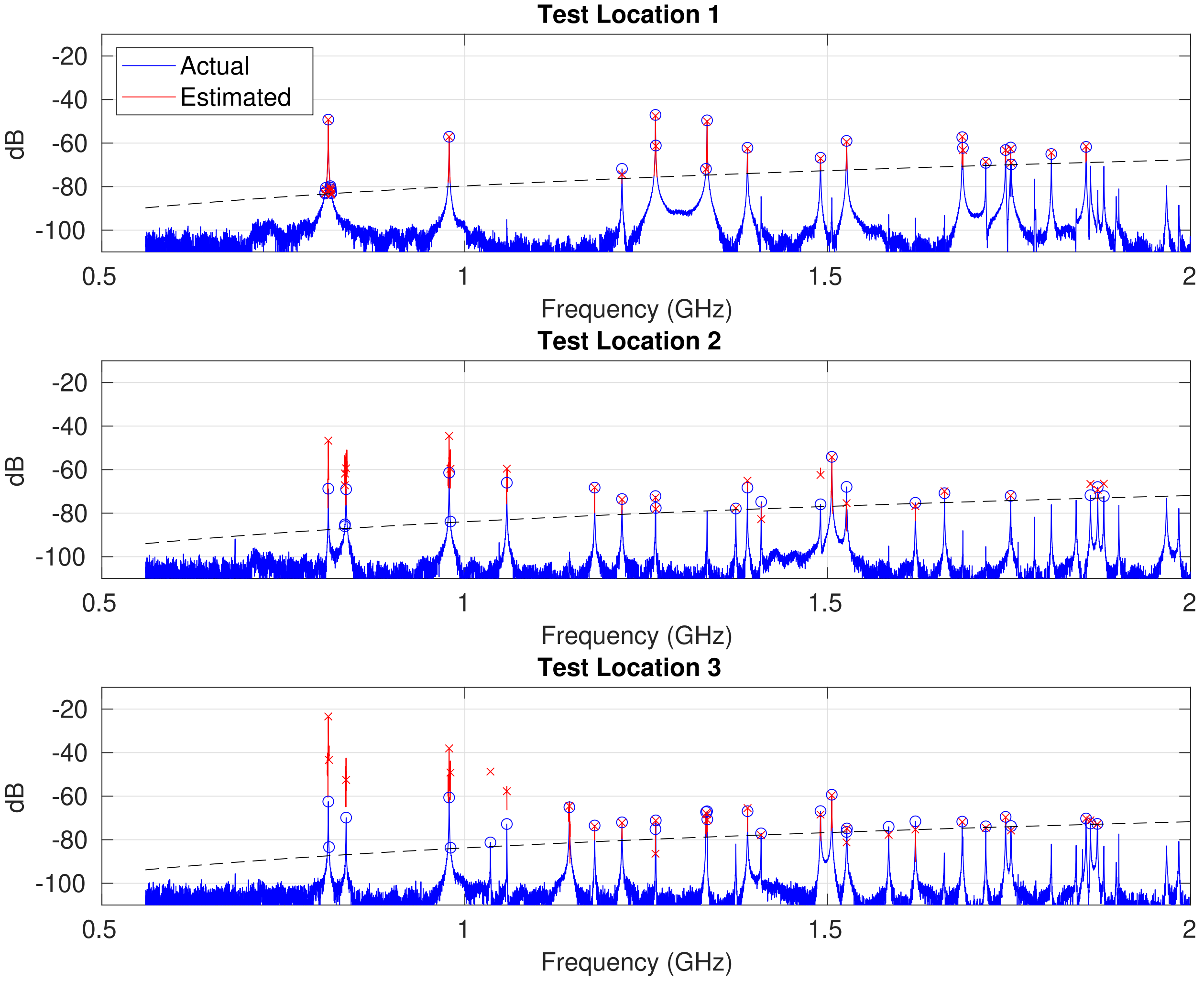

Location	P_{missed}	$\text{Error}_{90\%}$	$\text{Error}_{\text{avg}}$
1	0.00 %	0.8 dB	0.5 dB
2	26.09 %	8.0 dB	3.0 dB
3	26.67 %	3.7 dB	1.1 dB

Figure E-32. Measured heuristic probe set in box-in-PV2 with four probes.

E.3.2.6. Heuristic Probe Set (Simulated)

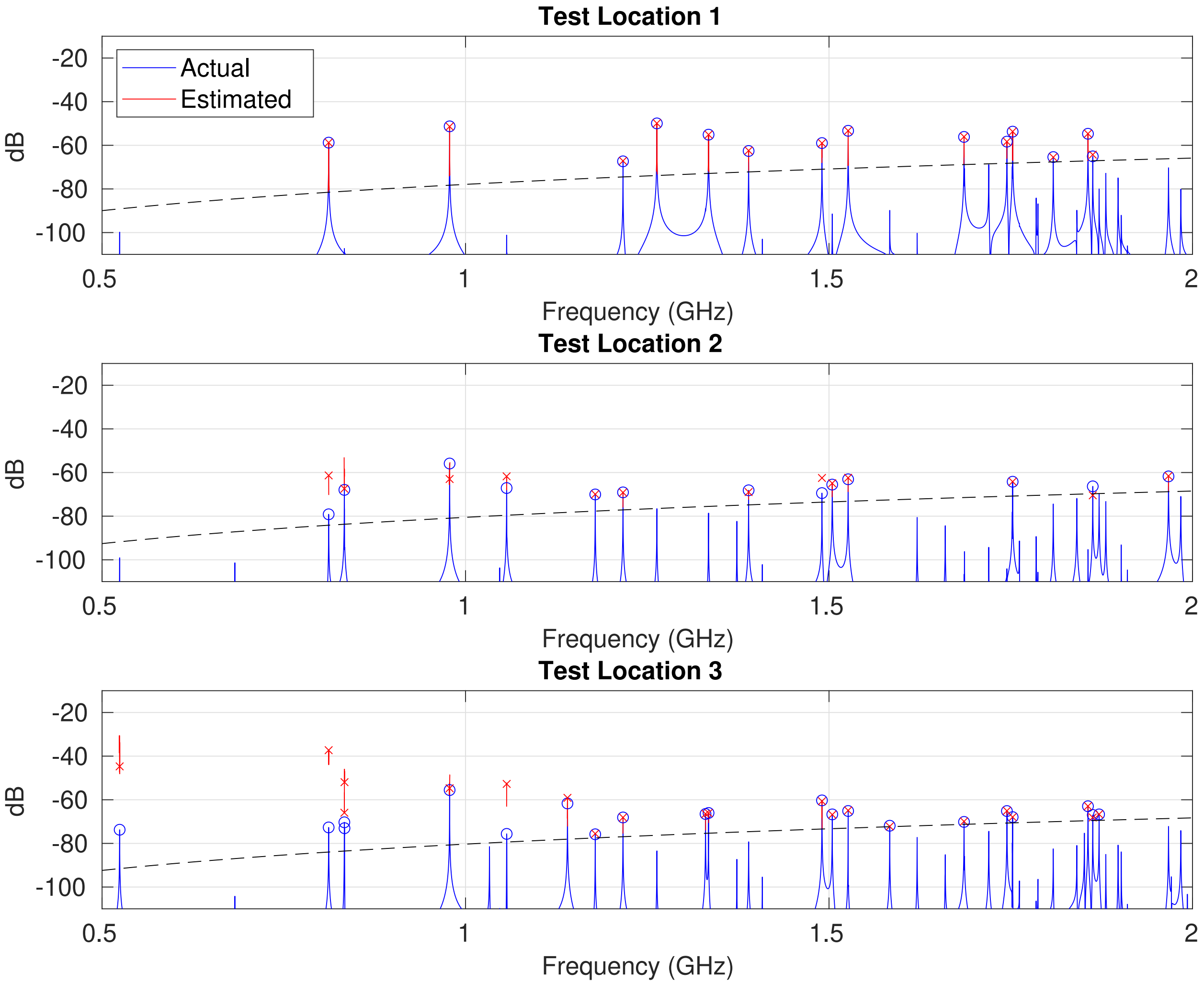

Location	P_{missed}	$\text{Error}_{90\%}$	$\text{Error}_{\text{avg}}$
1	0.00 %	0.2 dB	0.1 dB
2	7.69 %	6.9 dB	2.2 dB
3	19.05 %	2.6 dB	0.6 dB

Figure E-33. Simulated heuristic probe set in box-in-PV2 with four probes.

E.3.2.7. OED Probe Set (Measured)

This experiment was not performed.

E.3.2.8. OED Probe Set (Simulated)

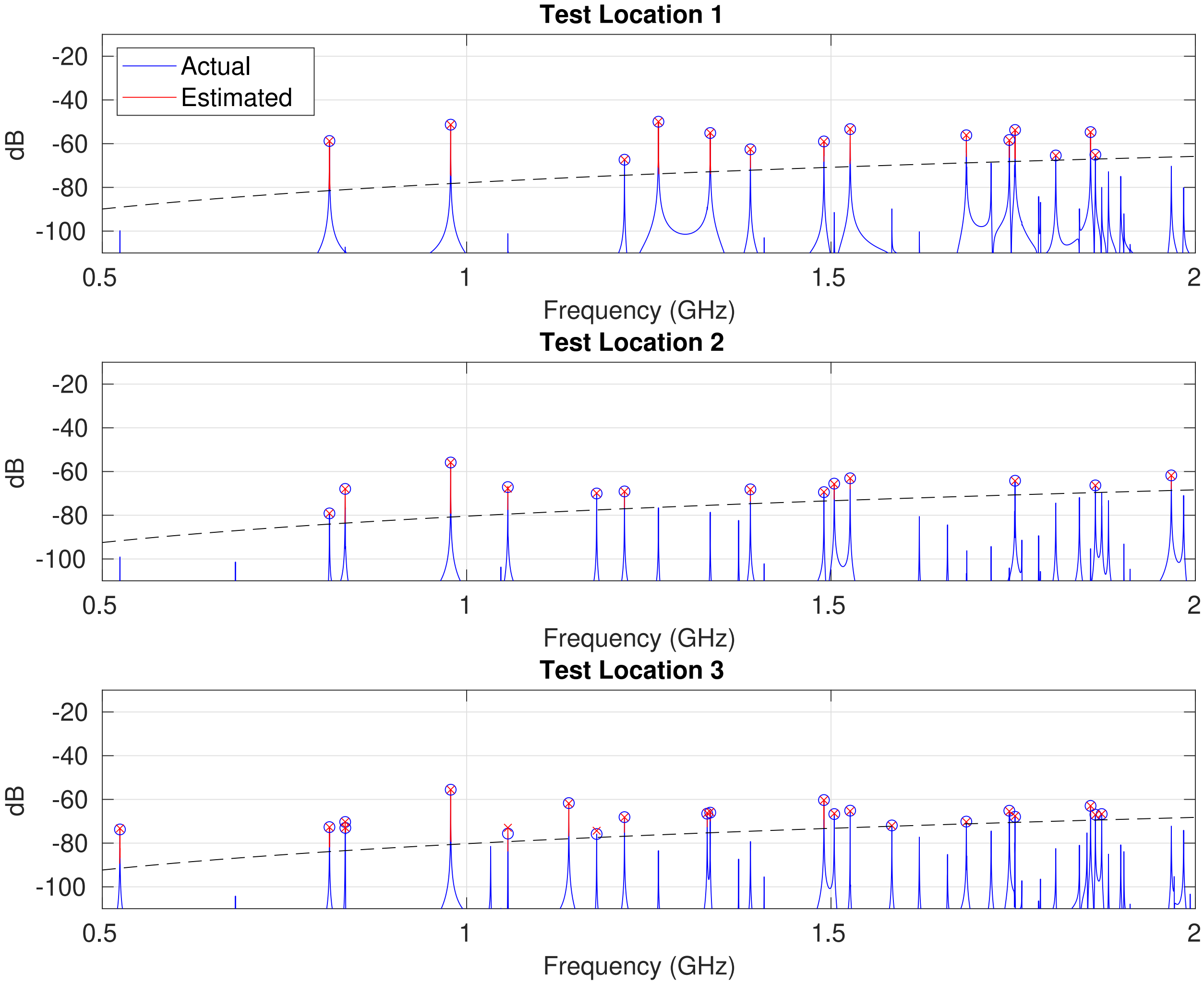

Location	P_{missed}	$\mathrm{Error}_{90\%}$	$\mathrm{Error}_{\mathrm{avg}}$
1	0.00 %	0.2 dB	0.1 dB
2	0.00 %	0.2 dB	0.1 dB
3	0.00 %	0.5 dB	0.3 dB

Figure E-34. Simulated OED probe set in box-in-PV2 with four probes.

This page intentionally left blank.

References

[1] R. E. Collin. *Foundations for Microwave Engineering*. IEEE Press, second edition, 2001.

[2] S. M. Kay. *Fundamentals of Statistical Signal Processing: Estimation Theory*. Prentice Hall, 1993.

[3] R. B. Lehoucq, D. C. Sorensen, and C. Yang. *ARPACK Users' Guide*. SIAM, 1998.

[4] D. M. Pozar. *Microwave Engineering*. Wiley, fourth edition, 2012.

[5] J. W. Wallace, I. J. Timmins, J. J. Himbele, I. C. Reines, R. K. Gutierrez, and J. T. Williams. Development of a novel electrical characterization technique for measuring hiddent joint contacts in weapons cavities, LDRD final report 218470. Technical Report SAND2022-12249, Sandia National Laboratories, Albuquerque, NM, Oct. 2022.

DISTRIBUTION

Email—Internal

Name	Org.	Sandia Email Address
Technical Library	1911	sanddocs@sandia.gov

Hardcopy—Internal

Number of Copies	Name	Org.	Mailstop
1	Technical Library	9536	0899

This page intentionally left blank.

Sandia National Laboratories